



universität
wien

DISSERTATION

Titel der Dissertation

“Synthesis and characterization of nanostructured dendritic
layers made by electrodeposition”

angestrebter akademischer Grad

Doktor der Naturwissenschaften (Dr. rer. nat.)

Verfasser:	Mag. Lidija Rafailovic
Matrikel-Nummer:	a0748903
Dissertationsgebiet (lt. Studienblatt):	Physik
Betreuer:	Univ.-Prof.i.R. Dr. Hans-Peter Karnthaler

Wien, am 15.Juni

Abstract

The electrodeposition technique has significant advantages for synthesizing nanocrystalline metals and alloys such as the potential of synthesizing a large variety of nanograined materials: pure metals and alloys with grain sizes as small as 20 nm. The goal of this work is to obtain different ferromagnetic alloy nanopowders and metal disperse deposits with a highly developed surface area that could be used as electrodes in electrochemical devices such as fuel cells, batteries and sensors. The basic characteristics of these electrodes are: the open porous structure which enables rapid transport of gas and liquid and the extremely high surface area which is desirable for electrochemical reactions. An approach that involves the application of extremely negative overpotential during metal electrodeposition, i.e. H_2 co-evolution method was used for deposition of dendritic deposits. Aqueous solutions undergo a rapid reduction of protons or water to H_2 that lead to the evolution of hydrogen gas bubbles at the cathode at such large negative overpotentials.

This strategy was applied to make dendritic CoNi foam on different substrates. The structure of deposited layers is governed by the nature of depositing ions and quantity of evolved hydrogen. The dendritic growth is a special case of structure formed in the CoNi alloy deposition at selected high current densities on polycrystalline Cu substrate. The selection of a substrate material, that shows a low wettability and contains a minimum density of structural defects, allows tailoring the morphology of the foam at lower current density when single-crystalline Cu (111) is used as a substrate. The very limited number of nucleation sites induces a localized flow of metal ions around large hydrogen bubbles and a dendritic nanocrystalline structure with grains as small as 9 nm can be achieved. The morphology of the open porous CoNi layer has a decisive influence on the kinetics of the surface redox reaction suitable for batteries. In addition, the open morphology of the dendritic foam facilitates catalytic activity for oxygen evolution for electrolyzers.

A further route to make hierarchical nanodendritic layers and powders of NiCoFe ternary alloy was used in this study. The powder particles were roughly 100 μm in diameter but contained dendrites down to 50 nm width, comprising nanodendritic branches with grains of about 8 nm. The hierarchical nature of the NiCoFe dendrites is reflected in the high Hausdorff fractal

dimensions of 1.77, which is close to that of fern plants. Self-assembly of metallic nanoparticles leads to a dendritic structure that could be suitable for practical applications. Layer deposits possess circular depressions of ca. 20 μm diameter due to the intensive H_2 gas evolution that accompanied the alloy deposition. The measurement demonstrated that the alloy is an effective catalyst for nitrate reduction.

Zusammenfassung

Elektrolytische Abscheidung hat immense Vorteile bei der Synthese von nanostrukturierten Materialien, da es die Möglichkeit bietet eine große Vielzahl an Materialien zu erzeugen, welche üblicherweise sehr kleine Korngrößen im Bereich von 20 nm aufweisen können.

Ziel der vorliegenden Arbeit ist es verschiedene ferromagnetische Nanopulver und Metallabscheidungen mit immenser Oberfläche zu erzeugen und zu charakterisieren, sodass diese als Elektroden in verschiedenen elektrochemischen Geräten wie beispielsweise Brennstoffzellen oder Batterien eingesetzt werden können. Wichtige Eigenschaften solcher Elektroden sind deren poröse Struktur zum schnellen Transport von Gasen und Flüssigkeiten sowie deren große Oberfläche für den Ablauf des elektrochemischen Prozesses. Zur Herstellung wurde ein Verfahren gewählt/entwickelt, welches mittels eines extremen Negativpotentials während der Abscheidung eine dendritische Struktur erzeugt. Dabei tritt in wässrigen Lösungen eine sehr schnelle Reduktion von Protonen oder Wassermolekülen zu H_2 auf, welche wiederum bei sehr großem negativen Potential zur Bildung von Gasblasen an der Kathode führt. Mit Hilfe dieses Verfahrens konnte ein dendritischer CoNi Schwamm hergestellt werden. Diese Struktur ist ein Spezialfall der Struktur von abgeschiedenem CoNi bei ausgewählten sehr hohen Stromdichten auf einem polykristallinem Cu Substrat. Die Auswahl eines geeigneten Materials für das Substrat, welches geringe Benetzung und gleichzeitig eine sehr geringe Dichte an strukturellen Defekten aufweist, erlaubt das gezielte Maßschneiden der Struktur des abgeschiedenen Materials bei geringerer Stromdichte. Für diesen Fall wurden Kupfer Einkristalle in (111) Orientierung als Substrat verwendet. Die äußerst geringe Zahl an Nukleationskeimen an der Oberfläche erzeugt einen lokalisierten Fluss an Metallionen in der Nähe der Wasserstoffblasen. Dadurch ist es möglich dendritische Strukturen mit Korngrößen von nur 9 nm zu erzielen. Weiters hat die Beschaffenheit der porösen CoNi Schicht einen sehr starken Einfluss auf die Kinetik der Redoxreaktion, wie sie in Batterien stattfindet. Auch während der Elektrolyse zeigen poröse Materialien eine erhöhte katalytische Wirksamkeit für die Bildung von Sauerstoff. Weiters wurden in dieser Arbeit nanodendritische Schichten und Pulver aus NiCoFe hergestellt. Am Beginn des Prozesses wiesen die Pulver eine Partikelgröße von etwa 100 μm mit darin enthaltenen Dendritstrukturen in der

Größenordnung von etwa 50 nm, bestehend aus einzelnen Dendritzweigen mit etwa 8 nm großen Körnern, auf. Diese hierarchische Ordnung in dendritischem NiCoFe spiegelt sich auch in der hohen Hausdorff Fraktaldimension von 1.77 wider, welche nahe an jener von Farnpflanzen liegt. Der Prozess der Selbstassemblierung in nanostrukturierten Materialien führt zu einer Nano-Dendritstruktur, welche ausgezeichnete Eigenschaften für diverse praktische Anwendungen bieten könnte. So wird durch Messungen gezeigt, dass diese Legierung durch das intensive Auftreten von H_2 Gasblasen kreisförmige Vertiefungen von etwa 20 μm Durchmesser aufweist und dadurch ein äußerst effektiver Katalysator für die Reduktion von Stickstoff ist.

Contents

List of terms	xvii
----------------------	-------------

1 Introduction	1
1.1 Synthesis of nanocrystalline and nanostructured materials . . .	1
1.2 Electrodeposition	3
1.3 Current density - overpotential	4
1.3.1 Mass transport	8
1.3.2 Concentration polarization	10
1.4 Electron transfer and mass transport	12
1.5 Hydrogen in metal electrodeposition	14
1.6 Electrocrystallization	17
1.6.1 Nucleation and Growth	19
1.6.2 Three-dimensional nucleation	23
1.6.3 Two-dimensional nucleation	23
1.7 Two sides of the interface	24
1.8 Interfacial region	25
1.9 Microstructure	26
1.10 Surface morphology	27
1.10.1 Compact nanocrystalline deposits	28
1.10.2 Disperse nanocrystalline deposits	29
1.10.3 Fractals	31
1.11 Catalytic properties of electrodeposits	33
1.12 Stress in electrodeposition	35
1.13 Wettability in electrodeposition	39
1.13.1 An influence of the surface roughness of a substrate on wetting	41

2	Experimental Procedures	45
2.1	Electrolytic fabrication techniques	45
2.2	Production of nanostructured deposits	46
2.3	Experimental setup	49
2.3.1	Synthesis	49
2.3.2	Electrochemical characterization-Cyclic Voltammetry .	50
2.4	Current efficiency	50
2.5	Characterization techniques	51
2.5.1	Microscopy methods	51
2.5.2	X-Ray Diffraction	52
2.5.3	Crystallite size	52
2.5.4	Lattice strain	53
2.5.5	Stress and texture	53
3	Structure/Properties of Ni-Co layers	57
3.1	Introduction	57
3.2	Experimental Procedure	58
3.3	Results and discussion	60
3.3.1	Current efficiency	60
3.3.2	Composition of the Ni-Co alloys	62
3.3.3	Microstructure of deposits	64
3.3.4	Phase analysis of deposits- Influence of current density on microstructure	67
3.3.5	Grain size of Ni-Co alloy deposits	69
3.3.6	Surface roughness of Ni-Co alloy deposits	71
3.3.7	Mechanical properties of Ni-Co deposits	72
3.4	Conclusions	75
4	Dendritic growth of Ni-Co layers	77
4.1	Introduction	77
4.2	Experimental Procedure	78
4.3	Results and discussion	79
4.3.1	Cathode polarization and efficiency	79
4.3.2	Growth of Ni, Co and dendritic Ni-Co deposits on Cu substrates.	82
4.3.3	EDX composition analysis of Ni-Co deposits.	83
4.3.4	Structural analysis of Ni-Co deposits.	85

4.3.5	Surface morphology of Ni-Co deposits	88
4.4	Conclusions	92
5	3D Dendritic Ni-Co Foams	95
5.1	Introduction	95
5.2	Experimental Procedure	96
5.3	Results and discussions	99
5.3.1	Wettability of single-crystalline Cu (111) and polycrystalline Cu substrates	99
5.3.2	Surface characteristic of microscopically rough CoNi dendritic deposits on single-crystalline Cu (111)	99
5.3.3	Morphology of CoNi layers on polycrystalline Cu and single-crystalline Cu (111) substrates	101
5.3.4	Microstructure of CoNi layers	102
5.3.5	Effect of the hydrogen bubble desorption on the formation of an open dendritic structure	104
5.3.6	Internal stresses of the CoNi layers	106
5.3.7	Enhanced catalytic ability of open, dendritic structure deposited on single-crystalline Cu (111) substrate . . .	108
5.3.8	Conclusions	109
6	Nanodendritic Ni-Co-Fe structures	113
6.1	Introduction	113
6.2	Experimental Procedure	114
6.2.1	Electrochemical characterization of NiCoFe alloy deposits	116
6.3	Results and discussions	117
6.3.1	Polarization diagrams for the deposition of dendritic Ni, Co and Fe metals and NiCoFe alloys	117
6.3.2	Nanofabrication of high surface area NiCoFe deposits .	117
6.3.3	Nanodendritic NiCoFe alloy as catalysts	122
6.3.4	Deposition of micro and nanoscaled metal alloy NiCoFe powders	123
6.3.5	Structural characterization of the electrodeposited ternary NiCoFe alloy powders	124
6.3.6	Morphology and size of the powder particles	125

6.3.7 Grain size of electrodeposited ternary NiCoFe alloy powders	127
6.4 Conclusions	130
Summary	131
Bibliography	137
Acknowledgements	151
Curriculum Vitae	153

List of Figures

1.1	Typical Tafel plots for the analysis of polarization	7
1.2	Diffusion of reacting particles and reaction products between bulk electrolyte and electrode surface	11
1.3	Complete polarization curves over a wide range of overpotentials	14
1.4	Two stages of electrodeposition process	18
1.5	The stages in the formation of a stable, growing nucleus of a metal on a inert carbon substrate	18
1.6	The various stages in the deposition of a thick layer of a metal on an inert substrate	19
1.7	Gibbs energy of nucleation as a function of nucleus radius . .	21
1.8	Different nucleus models for different number of cluster atoms	23
1.9	A two-dimensional nucleation with the nucleus in the approx- imate form of a circle	23
1.10	The cubic coordination sites in the lattice of perfect single crystal	24
1.11	Model of the interfacial region at the electrode surface for potentials negative to the potential of zero charge	26
1.12	Schematic representation of the dependance of deposition pa- rameters on grain size of electrodeposits	27
1.13	Polarization curve for the potentiostatic deposition of copper	30
1.14	Examples of fractals	32
1.15	(Top) Edge dislocation forming in an electrodeposited metal near a surface vacancy in the basis metal.(Bottom) How an ar- ray of dislocations produces a tensile stress in electrodeposits.	39
1.16	Wettability of liquid on solid surface	40

1.17	Schematic diagrams showing (a) Cassie-Baxter and (b) Wenzel wetting regimes.	41
2.1	Schematic representation of the electrochemical cell	47
2.2	Schematic diagram for electrodeposition process	47
2.3	Three experimental methods for deposition of metal nano and micro particles dispersions exhibiting excellent size monodispersity	48
2.4	A typical cyclic voltammogram showing reduction and oxidation current peaks	51
2.5	Schematic drawing of the difference between strain induced by external forces and internal lattice strain due to the defects in the crystal structure	53
2.6	Schematic drawing of the orientation of crystallites in a polycrystalline sample	54
2.7	Diffraction set up for texture and macroscopic stress measurements	55
3.1	Polarization curves for the cathodic process of NiCo deposition on copper cathode for different composition of the electrolyte	60
3.2	Current efficiency of the Ni-Co deposition process for the different current densities and compositions of the electrolyte . .	61
3.3	Dependence of the alloy composition on the $\text{Ni}^{2+}/\text{Co}^{2+}$ ratio in the electrolyte at a current density of 65mA cm^{-2}	63
3.4	Dependence of the alloy composition on current density from an electrolyte with concentration ratio $\text{Ni}^{2+}/\text{Co}^{2+}=1$	63
3.5	X-ray diffraction patterns of alloys deposited from the electrolyte with different $\text{Ni}^{2+}/\text{Co}^{2+}$ concentration ratios	64
3.6	SEM micrographs of Ni-Co deposits obtained at a current density of 65 mA cm^{-2} from an electrolyte with different $\text{Ni}^{2+}/\text{Co}^{2+}$ concentration ratios	68
3.7	X-ray diffraction patterns of alloys deposited from an electrolyte with concentration ratio $\text{Ni}^{2+}/\text{Co}^{2+}=1$ at different current densities	69

3.8	Evolution of the FCC phase content in deposits as a function of current density from an electrolyte with a concentration ratio $\text{Ni}^{2+}/\text{Co}^{2+}=1$	70
3.9	3D SEM reconstruction of the surfaces of Ni-Co deposits obtained at a current density of 65 mA cm^{-2} from the electrolyte with different $\text{Ni}^{2+}/\text{Co}^{2+}$ concentration ratios	71
3.10	Hardness of Ni-Co deposits as a function of current density and electrolyte composition	73
3.11	Cross-section of Ni-Co deposits obtained on a copper substrate from an electrolyte with concentration ratio $\text{Ni}^{2+}/\text{Co}^{2+}=1$	74
3.12	Effect of the grain size on the hardness of Ni-Co deposits produced from an electrolyte with different $\text{Ni}^{2+}/\text{Co}^{2+}=1$ concentration ratios	74
4.1	Polarization curves for galvanostatic Ni, Ni-Co and Co deposition from different solutions	81
4.2	The dependence of the current efficiency on current density for Ni, Ni-Co and Co electrodeposition	82
4.3	Cross-sections of Ni-Co deposits galvanostatically obtained from the solution containing equal concentration ratio $\text{Ni}^{2+}/\text{Co}^{2+}=1$ at different current densities	84
4.4	Cross-sections of Ni and Co deposit galvanostatically obtained at a current density of 65 mA cm^{-2}	84
4.5	XRD of Ni, Co and Ni-Co deposits galvanostatically obtained on Cu substrates at different current densities	86
4.6	3D SEM reconstruction of the surfaces of Ni-Co deposits galvanostatically obtained at different current densities	89
4.7	3D SEM reconstruction of the surface of Ni deposit galvanostatically obtained at current density of 400 mA cm^{-2}	89
4.8	3D SEM reconstruction of the surface of Co deposit galvanostatically obtained at current density of 220 mA cm^{-2}	90
4.9	SEM micrograph of Ni deposit formed by galvanostatic deposition at different current densities	91
4.10	Schematic representation of the dendrite formation	92
5.1	SEM image of the surface of the polycrystalline Cu substrate (PC) and the single crystalline Cu (111) substrate (SC)	100

5.2	3D SEM reconstruction of the foam surface of CoNi deposited on single crystalline Cu (111) substrate	100
5.3	SEM micrographs of Co ₉₀ Ni ₁₀ layers on the PC and SC substrates made after the same deposition time	103
5.4	XRD of electrodeposited CoNi layers on Pc and SC substrates	105
5.5	Schematic representation of the CoNi electrodeposition process during concurrent hydrogen evolution reaction	107
5.6	Cyclic voltammograms obtained on different morphology of electrodeposited CoNi layers	110
6.1	Linear sweep voltammograms for the electrodeposition of non-dendritic and dendritic Ni, Co, Fe and NiCoFe nanostructures	118
6.2	SEM images of NiCoFe alloys obtained at different current densities	120
6.3	X-ray profile of the NiCoFe non-dendritic and dendritic deposit	121
6.4	3D SEM reconstruction of the dendritic NiCoFe surface . . .	122
6.5	Linear sweep voltammograms on non-dendritic and dendritic NiCoFe deposits	123
6.6	X-ray profile of the electrodeposited NiCoFe powder	124
6.7	SEM images of NiCoFe powder electrodeposited at the same current density after different deposition times	126
6.8	Particle size distribution of NiCoFe alloy powder	126
6.9	Transmission Electron Microscopy (TEM) study of the NiCoFe powder	128
6.10	Grain size distribution of the NiCoFe powder	129

List of Tables

1.1	Standard potentials of metal deposition and dissolution reactions	5
1.2	Typical cathode current efficiencies during electrodeposition .	16
1.3	The hydrogen discharge mechanism	16
3.1	Phase composition, grain size and cell parameters of the Ni-Co alloys electrodeposited from the electrolyte with a different $\text{Ni}^{2+}/\text{Co}^{2+}$ concentration ratios	66
3.2	Roughness parameters of alloys deposited from electrolytes of different $\text{Ni}^{2+}/\text{Co}^{2+}$ concentration ratio and at different current densities	72
4.1	Cross-section composition analysis of Ni-Co alloys deposited at different current densities	83
4.2	Phase composition, grain size and cell parameters of the Ni-Co alloys deposited from solution containing 0.12 mol dm^{-3} ($\text{NiSO}_4 + \text{CoSO}_4$), ratio $\text{Ni}^{2+}/\text{Co}^{2+}=1$ at different current densities	87
5.1	Results of the XRD measurements of the $\text{Co}_{90}\text{Ni}_{10}$ electrodeposits on different substrates	109

List of terms

- a_i - activity of species i (mol dm^{-3})
 c_i - concentration of species i in the bulk solution (mol dm^{-3})
 A - geometric area of electrode (m^2) or (cm^2) or rate constant for nucleation (s^{-1})
 D - diffusion coefficient (m^2s^{-1})
 F - Faraday constant (Fmol^{-1})
 R - gas constant ($\text{J K}^{-1}\text{mol}^{-1}$)
 k - Boltzmann constant (J K^{-1})
 T - Temperature (K)
 ΔG - Gibbs's free energy change (kJmol^{-1})
 I - current (A or mA)
 j - current density (Am^{-2} , mA cm^{-2} , etc)
 j_L - limiting current density (mA cm^{-2} , etc)
 j_o - exchange current density (mA cm^{-2} , etc)
 J_i - flux of species i ($\text{mol m}^{-2}\text{s}^{-1}$)
 E - potential vs a reference electrode (V or mV)
 E_e - equilibrium potential for the couple O/R vs a reference electrode (V or mV)
 E_o - standard electrode potential for the couple O/R vs a reference electrode (V or mV)
 n - number of electrons involved in electrode reaction (dimensionless)
 α - transfer coefficient (dimensionless)
 δ - thickness of diffusion layer (m)
 σ - surface roughness
 μ - chemical potential (V or mV)
 η - overpotential (V or mV)
 E_{pzc} - potential of zero charge of electrical double layer

θ - contact angle or diffraction angle

ν - current efficiency (%) or Poisson's ratio of the material

γ - interfacial tension

σ - stress (Pa)

ψ - the tilt angle of the sample

ϕ - the rotation of the sample

Ra- mean roughness (μm)

Rz- the difference between the highest and the lowest point in the picture of defined scan (μm)

RS - active surface, the ratio of the real surface including topography to a projected surface (μm^2)

Sign conventions

Anodic currents are positive and cathodic currents are negative. Making the potential more positive will increase the driving force for oxidation and making the potential more negative will increase the driving force for reduction.

Chapter 1

Introduction

1.1 Synthesis of nanocrystalline and nanostructured materials

Nanocrystalline materials [1] as a new class of materials structurally characterized by a large volume fraction of grain boundaries, which may significantly alter their physical, mechanical, and chemical properties in comparison with conventional coarse-grained polycrystalline materials [2], have been the subject of widespread research over the past couple of decades with significant advancement in their understanding especially in the last few years. Nanocrystalline materials are single- or multiphase polycrystals with typical grain diameter less than 100 nm. At the upper limit of this regime, the term “ultrafine grain size” is often used (grain sizes of 250-1000 nm). Nanometric features of nanocrystalline metallic systems relevant to the functional properties are: grain dimensions, regions of the material exhibiting a given orientation of the crystal lattice, atomic density gradients and zones with a different chemical composition.

A number of techniques have surfaced over the years for producing nanostructured materials, but most of them are limited to synthesis of small quantities [2]. There has been a constant quest to scale up to bulk processing, and lately, a few advances seem to hold technological promise.

Nanocrystalline materials can be synthesized either by consolidating small clusters or breaking down the polycrystalline bulk material into crystalline units with dimensions of nanometers. These approaches have been classified into bottom-up and top-down. In the bottom-up approach the nanostructure

is built atom-by-atom, layer-by layer. In the top-down approach the bulk material microstructure is converted into a nanostructure. The principal synthesis methods are:

- Inert gas condensation
- Mechanical alloying
- Electrodeposition
- Crystallization from amorphous material
- Severe plastic deformation
- Cryomilling
- Plasma synthesis
- Chemical vapor deposition
- Sputtering
- Physical vapor deposition
- Spark erosion

The different types of nanostructured materials share two main characteristics: (i) the atomic domains (grains or phases) are confined in space to submicrometric domains, (ii) a high fraction of atoms is found in interfacial regions. According to their dimensionality, nanostructured materials can be categorized into four categories: 0D-nanoclusters; 1D-multilayers; 2D-nanograined layers; 3D-equiaxed bulk solids. In addition, nanowires, that are one-dimensional nanostructures, have important electronic properties. Metallic systems with all these kinds of dimensionality can be obtained by electrodeposition, even though the broadest scope for applications is related to the three dimensional ones [3]. The importance of the nanometer scale stems from the fact that in this range of dimensions several properties achieve special values, essentially owing to confinement effects.

1.2 Electrodeposition

Electrodeposition is starting to be regarded as a viable process for nanofabrication and - even though electrocrystallisation has received considerable attention from both the theoretical and experimental viewpoints - it is now worth focusing systematically on the role of processing and electrochemical engineering factors, in the tailoring of nanosized structural features [3]. Electrodeposition has significant advantages over other methods for synthesizing nanocrystalline materials such as the potential of synthesizing a large variety of nanograined materials: pure metals, alloys and composite systems with grain sizes as small as 20 nm [4].

Recent investigations have highlighted electrodeposition as an attractive approach for the preparation of nanostructured materials. Electrodeposition provides a cost-effective method using readily available equipment for the preparation of nanocrystalline and nanophase metallic materials (metals, alloys, compositionally modulated alloys and composites) either as coatings or as freestanding objects even in complex shapes (foils, wires, electroforms) [5]. The low processing temperature (around room temperature) minimizes interdiffusion or chemical reaction. The film thickness can be accurately controlled by monitoring the charge passed. Composition and defect chemistry can be controlled by electrical and fluid-dynamic means. Deposition rates of the order of several tens of microns per hour can be routinely achieved. Potentially there are a very large number of pure metals, alloys, composites, and ceramics which can be electrodeposited with grain sizes less than 100 nm. For example, the literature contains numerous examples giving electrochemical processing windows for the synthesis of nanocrystalline pure metals e.g., Ni [6, 7], Pd [8], Co and Cu films [9] and binary alloys e.g., Ni-P [10, 11], Ni-Fe [12, 13], Zn-Ni [14], Co-Zn [15], Pd-Fe [16] as well as various hard thin films, i.e. platinum and tungsten alloys [17] and ternary NiCoFe alloys [18]. Even multilayered structures or compositionally modulated alloys e.g., Cu-Pb [19], Cu-Ni [20], Ag-Pd [21], Ni-P [22], metal matrix composites (e.g., Ni-SiC) [6], ceramics (e.g., ZrO₂) [23], and ceramic nanocomposites [24] have been successfully produced by electrodeposition methods.

1.3 The current density - overpotential - Basic equations

Fundamental aspects of electrochemical deposition include the heterogeneous electron transfer step between the electrode and the electroactive species present in solution as well as the transition of the discharged metal atoms into the crystalline state. Electrochemical deposition of metals typically proceeds by reduction of species in a solution, Eq. (1.1).



The standard electrode potential for an electrochemical reaction is the potential where there is zero net current due to the rate of the reduction and the oxidation reactions being equal, at standard activity, pressure (1 atm) and temperature (298 K). The Nernst equation relates the electrode potential E to the standard electrode potential E° :

$$E_e = E_e^\circ + \frac{RT}{nF} \ln \frac{a_o}{a_R} \quad (1.2)$$

Where R denotes the standard gas constant ($8.314510 \text{ J K}^{-1} \text{ mol}^{-1}$), T the absolute temperature in K, n the number of electrons transferred and F the Faraday's constant ($96485.309 \text{ C mol}^{-1}$) [25]. The potential also depends on the ratio of natural logarithm of the activities of the oxidized and reduced species.

The electrolysis of species can be performed using constant current through the electrochemical cell, while the electric potential is monitored (galvanostatic deposition). Alternatively, in potentiostatic deposition a desired potential can be chosen, which is then maintained by the instrument while the necessary current used to maintain that potential is monitored. If the electrolyte contains more than one species of metal ion, it is possible to deposit alloys under certain conditions. The respective values of E° serves as an approximate guide for determining whether two metals may be co-deposited from salt solution. In general, metals, which have similar values of equilibrium standard electrode potential are more readily co-deposited. Table 1.1 gives the standard electrode potentials for some electrode reactions. The values of standard electrode potentials given in the Table 1.1 are relative to the standard hydrogen electrode arbitrary chosen to be zero.

Electrode reaction	Standard potentials, (V)	Electrode reaction	Standard potentials, (V)
$Li^+ + e^- = Li$	-3.045	$Fe^{2+} + 2e^- = Fe$	-0.4
$K^+ + e^- = K$	-2.925	$Co^{2+} + 2e^- = Co$	-0.277
$Na^+ + e^- = Na$	-2.714	$Ni^{2+} + 2e^- = Ni$	-0.250
$Mg^{2+} + 2e^- = Mg$	-2.363	$Sn^{2+} + 2e^- = Sn$	-0.163
$Al^{3+} + 3e^- = Al$	-1.662	$Cu^{2+} + 2e^- = Cu$	0.337
$Zn^{2+} + 2e^- = Zn$	-0.763	$Cu^+ + e^- = Cu$	0.521

Table 1.1: Standard potentials of metal deposition and dissolution reactions.

The electrode potential is directly connected to the Gibb's free energy change of the electrode process at standard conditions through the relationship:

$$\Delta G^o = -nFE^o \quad (1.3)$$

An inert electrode will take up the equilibrium potential E_e for the redox couple O/R in the solution represented by Eq. (1.1) when no net current flows. Both reduction of O to R and oxidation of R to O will occur at the electrode surface but the forward and reverse reaction take place at the same rate. In terms of current density (current per unit area of electrode or $j = I/A$) the total current density is a sum of partial anodic and cathodic current densities with opposite signs. The magnitude of these anodic or cathodic partial current densities at the equilibrium potential turns out to be an important kinetic characteristics for the couple and it is called exchange current density, j_o . It is a measure of electron transfer activity at the equilibrium potential [25].

A thorough discussion of the current density - overpotential relationship was given by Bockris [26]. The approach suitable for use in metal electrodeposition will be given here for the electrochemical reaction represented by Eq. (1.1). The difference in the electrode potential versus reference electrode between operating potential and equilibrium potential when a current is flowing is defined as an overpotential in Eq. (1.4). The overpotential is a measure (via Eq. 1.3) of the extra energy needed (an energy loss that appears as heat) to force the electrode reaction to proceed at a required rate

(or its equivalent current density).

$$\eta = E - E_e \quad (1.4)$$

or as:

$$\eta = \frac{RT}{nF} \ln \frac{a}{a_e} \quad (1.5)$$

Where E_e is the equilibrium potential of a bulk metal crystal dipped in a solution of its ion with activity a_e (assuming no IR loss).

The general form of current density - overpotential relationship in electrodeposition of metals for the reaction is given by:

$$j = -j_o \left[\frac{a_j^0}{a_e^0} f_c - \frac{a_j^R}{a_e^R} f_a \right] \quad (1.6)$$

where j_o is the exchange current density and a is the activity of the oxidized (O) or reduced (R) state at a current density j and a_e is the activity in the equilibrium state [27].

And f_c and f_a are given by:

$$f_c = \exp\left(\frac{-\alpha_c n F \eta}{RT}\right) = \exp\left(\frac{2.3}{b_c} \eta\right) \quad (1.7)$$

and

$$f_a = \exp\left(\frac{\alpha_a n F \eta}{RT}\right) = \exp\left(\frac{2.3}{b_a} \eta\right) \quad (1.8)$$

where α_c and α_a are the cathodic and anodic transfer coefficients, b_c and b_a corresponding Tafel slopes and η is the overpotential. The Tafel slopes are defined as:

$$b_c = \frac{-2.3RT}{\alpha_c n F} \quad (1.9)$$

and

$$b_a = \frac{2.3RT}{\alpha_a n F} \quad (1.10)$$

The transfer coefficients are best considered as the fraction of the change in the overpotential which leads to a change in the rate constant for electron transfer.

The Tafel slopes are generally obtained from the Butler Volmer equation for both anodic and cathodic reaction assuming $\frac{a_j^0}{a_e^0} = \frac{a_j^R}{a_e^R}$ is equal, i.e. only

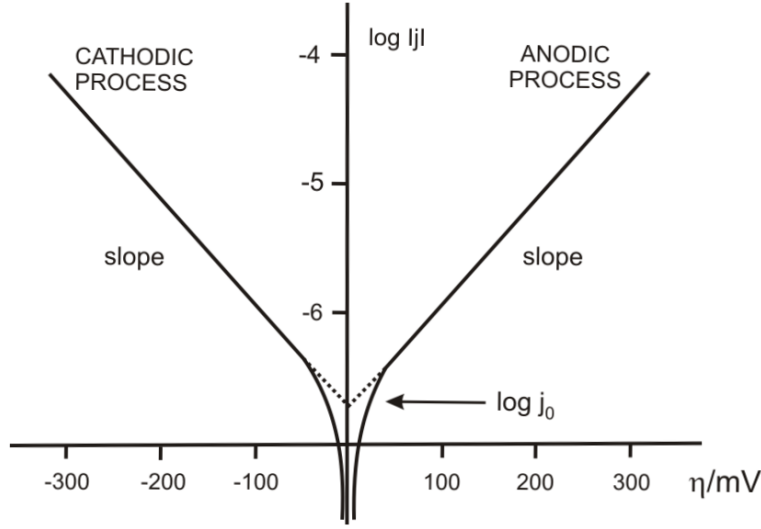


Figure 1.1: Typical Tafel plots for the analysis of polarization [25].

charge transfer limitation in the small overpotential region:

$$j = j_o \left[\exp\left(\frac{\alpha_a n F \eta}{RT}\right) - \exp\left(\frac{-\alpha_c n F \eta}{RT}\right) \right] \quad (1.11)$$

It can be seen from this equation that only close to the equilibrium potential (i.e. for low values of overpotential) both exponential terms are significant. When the current density can be measured at both positive and negative overpotentials, it is convenient to analyze the data using a modification of Butler Volmer equation, obtained by noting that $\alpha_c = 1 - \alpha_a$, dividing through by $\exp(\frac{\alpha_a n F \eta}{RT})$ rearranging and taking logs to give a form known as the Tafel equations for positive values of overpotential ($\eta > \frac{RT}{\alpha_a n F}$):

$$\log j = \log j_o + \frac{\alpha_a n F \eta}{RT} \quad (1.12)$$

or for negative values of overpotential ($\eta < -\frac{RT}{\alpha_c n F}$)

$$\log -j = \log j_o - \frac{\alpha_c n F \eta}{RT} \quad (1.13)$$

At both positive or negative overpotentials, there will be ideally a linear relationship between $\log|j|$ and η known as Tafel linearity (Fig. 1.1). Both lines should extrapolate to $\log j_o$ at $\eta = 0$ (Fig. 1.1) and the transfer coefficient can be obtained from the slopes since the $\alpha_c + \alpha_a = 1$.

1.3.1 Mass transport

The supply of reactant and the removal of product from the electrode surface are essential to a continuing chemical change. We have to consider that the activity of a charged species depends on the local electrostatic potential, and the work of transport will include the electrical work associated with movement of charge between phases of different potential. To describe this, the electrochemical potential of charged species is defined as the sum of the chemical ($\mu = \mu_o + RT \ln a_i$) and electrical potentials ($z_i F \varphi$) for the component i . In general it is possible to have contributions from three forms of mass transport:

(i) diffusion

Represents the movement of the species due to a concentration gradient. Hence, diffusion is a physical process which causes the transport of species from a region of concentrated solution to region which is more dilute, until the concentrations become equal.

(ii) convection

Convection is a movement of species due to external mechanical forces. It can be caused by thermal convection, by rotating the electrode in the cell or by introducing gas into the solution.

(iii) migration

Migration is the movement of charged species due to a potential gradient. In all electrochemical cells, a current is passed between two electrodes and this requires the application of a voltage and, therefore, the creation of a potential field. Migration arises from the purely electrostatic forces and, hence, is not necessarily important for the transport of all species in the system. The common way to neglect the influence of migration is to add a high concentration of non-reactive electrolyte (also called the inert or supporting electrolyte) to the solution of the electroactive species; one of its roles is to ensure that migration does not contribute significantly to the transport of the electroactive species. The reactant and/or the product of the electrode reaction will be charged species but if they are surrounded by a large excess of the ions of the supporting electrolyte. Contribution of the supporting electrolyte to the j - E response is neglected since it does not have any electron transfer chemistry in the potential range of redox couple defined from Eq. (1.1).

The flux of charged species is caused by difference in the electrochemical

potential. For linear mass transport, the flux can be governed by the Nernst-Planck equation:

$$J_i(x) = -D_i \frac{\partial c_i(x)}{\partial x} - \frac{z_i F}{RT} D_i c_i \frac{\partial \varphi_i(x)}{\partial x} + c_i \nu x \quad (1.14)$$

where J_i is the flux of charged species i , D_i is a diffusion coefficient, z_i is the number of electrons, F the Faraday constant, R the gas constant, T the temperature, φ the voltage drop and ν the stirring velocity. Mass transfer is concerned with three different items, which are diffusion (i.e. first term in Eq. (1.14), migration (i.e. second term in Eq. (1.14) and convection (i.e. third term in Eq. (1.14)). Two kinds of convection are involved in electrochemical cell, one is nature convection due to the density gradient and the other is artificial stirring. Migration makes protons migrate towards the cathode and electrons migrate to the anode due to the potential gradient. In bulk solution, i.e. away from the electrode, current is mainly controlled by migration because concentration gradients are generally small. On the contrary, current near the electrode surface is dominated mainly by diffusion due to high concentration gradients. In potentiostatic mode, diffusion limited current can be obtained by applying a specific potential which is higher than the reduction potential. On the contrary, in galvanostatic mode diffusion-limited current can not be defined due to the significant hydrogen evolution.

An important step of the reaction mechanism in a heterogeneous process is the transport of the reacting substances and reaction products between the place of reaction (i.e. electrode) and the bulk phases. If the driving force for the transport is a concentration gradient, the transport process is diffusion (Fig. 1.2). In the general redox system depicted in Fig. 1.2a, the oxidized or reduced components diffuse between the bulk electrolyte and electrode surface. In electrochemistry, in addition to the concentration gradient, a gradient of the electric field can be the driving force. This process is called electro-migration and is often important in solid or polymer electrolytes, particularly in mass transport. In electrodeposition (Fig. 1.2b) solvated metal ions diffuse to the surface and lose the solvation shell in the process of depositing. The solvents diffuses back into the electrolyte. Mass transport in polymer or solid phases is much slower than in aqueous electrolytes. The process is nevertheless important for many applications like charging and discharging of batteries. Control and enhancement of the charge transfer by

diffusion or migration is a big problem in electrochemical kinetics.

The diffusion process operates under a concentration gradient and is typically the most important of all three processes, because it is typically dominant in mass transport in batteries. The analysis of diffusion is carried out by a basic equation which defines the flux of material crossing a plane at distance x and time t . The flux is proportional to the concentration gradient and it is represented by the first Fick's law:

$$J = -D \frac{\partial c}{\partial x} \quad (1.15)$$

The rate of change of concentration with time is defined by the second Fick's law.

$$\frac{\partial c}{\partial t} = D \frac{\partial^2 c}{\partial x^2} \quad (1.16)$$

In this work laboratory experiments were carried out with totally unstirred solutions containing a large excess of supporting electrolyte. Diffusion is then the predominant mode of mass transport.

1.3.2 Concentration polarization

In this approach only the diffusion of metal ions is taken into account. The transport of metal ions can be substituted by the cathodic current density:

$$j = -nFD \frac{c_o - c_s}{\delta_d} \quad (1.17)$$

where δ_d is a diffusion layer thickness.

A limiting current is reached as the concentration on the surface, c_s , approaches zero

$$j_L = -nFD \frac{c_o}{\delta_d} \quad (1.18)$$

The change in the surface concentration leads to a shift in the Nernst potential:

$$E - E^o \cong \frac{RT}{nF} \ln \frac{c_s}{c_o} \quad (1.19)$$

The difference $E - E^o$ is the diffusion overpotential $\eta_d = E - E^o$. The concentration ratio can be substituted by the current densities:

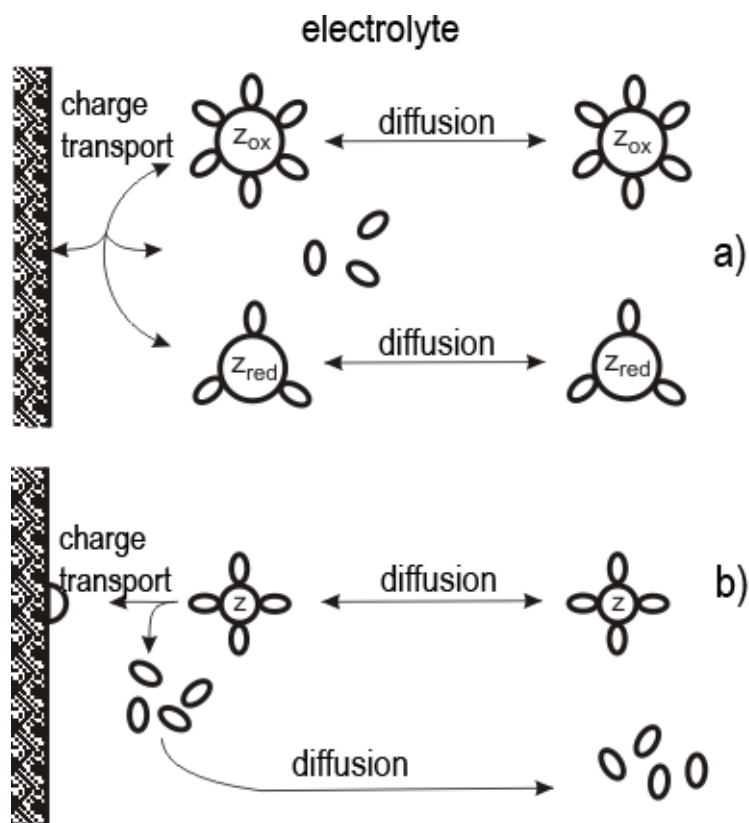


Figure 1.2: Diffusion of reacting particles and reaction products between bulk electrolyte and electrode surface. (a) Redox process in the electrolyte and (b) deposition reaction of a solvated metal ion [28].

$$\frac{c_s}{c_o} = \frac{j_L - j}{j_L} \quad (1.20)$$

As a result, the diffusion overpotential is given by the equation:

$$\eta_d = \frac{RT}{nF} \ln\left[1 - \frac{j}{j_L}\right] \quad (1.21)$$

1.4 The interaction of electron transfer and mass transport

It has been pointed out in previous section that, even in the simplest cases, an electrode reaction is a complex sequence of three events. For the reduction of O to R it can be represented by mass transport of oxidized species from the bulk O_{bulk} to the electrode $O_{electrode}$ and then by reduction at the electrode to $R_{electrode}$ and finally by mass transport from the electrode to the bulk, O_{bulk} . If the experiment is commenced at the equilibrium potential which according to Eq. (1.2) is $E_e^o = -60$ mV for the ratio $c_o/c_R = 10 \text{ mol } m^{-3}$, no net current will be observed. Although no net chemical change occur at this potential, the magnitude of the partial currents for oxidation and reduction depend on kinetics of electron transfer for the couple O/R. As the potential is taken positive of the equilibrium potential, it is possible to identified three distinct potential regions. Each of these regions characterize a different slowest step in the electrochemical process.

(i) activation control

In activation control, the electrochemical overpotential that determines the whole process is caused by slow charge transport of the electroactive species. Therefore, charge transfer is the rate determining step and according to Butler Volmer and Tafel equations, j-E has an exponential dependance of current density on overpotential. The activation-controlled region is usually determined by values of exchange current density and limiting current density ($5 j_o < j < 0.01 j_L$) [25]. In practice, current from another electrode reaction, e.g. the reduction of impurities, frequently can contribute the lowest current density which may be recorded for reduction of O to R. As long as electrode reaction is solely electron transfer controlled, the current density is totally independent of the mass transport regime.

When the electrode potential is made more negative in relation to the

standard reduction potential for an electrochemical reaction, the reduction current increases because the rate of electron transfer of the reduction increases. In the electron transfer controlled potential region, there is a linear relationship between the potential and the logarithm of the deposition current known as the Tafel linearity. However, in practice the current can also be limited by other factors such as mass transfer, preceding chemical steps and crystallization processes.

(i) mixed control

As the overpotential is increased further, the rate of electron transfer continues to increase exponentially and eventually the rate of reduction of O at the electrode will approach the rate of its transport at to the surface. In another words, the electron transfer process becomes fast enough that the surface concentration begins to decrease significantly from the bulk value so that the mass transport becomes an important part of the reaction with further consequence on non-linearity in j-E plot.

(i) mass transport control

The mass transport region is determined by slow diffusion step of electroactive species to the electrode surface. If the electron transport is rapid, the surface concentration of O then drops to zero and the current density will become fully mass transport controlled. As a result, the current density is independent of overpotential but strongly dependant on the mass transport regime. An electrode reaction is considered to be under “diffusion control” when the overall rate of the reaction is is controlled by the rate of the diffusion of the reactants to the electrode surface rather than the rate of the reaction itself or the IR drop in the solution.

An electrode reaction where electron transfer determines the surface concentration at lower overpotentials is irreversible. If the exchange current density is large and, i.e. the electron transfer reaction is inherently fast, then it is possible at all potentials, the electron transfer reaction remains in equilibrium under the prevailing mass transport conditions. The surface concentration then can be calculated from the Nernst equation and the electrode reaction is reversible (terms reversible and irreversible are used in thermodynamic sense to denote whether the electron transfer reaction at the electrode is in equilibrium or not). The shapes of j-E polarization curves (Fig. 1.3) are distinct in respect of determination of polarization regions associated with an rate determining step in overall process.

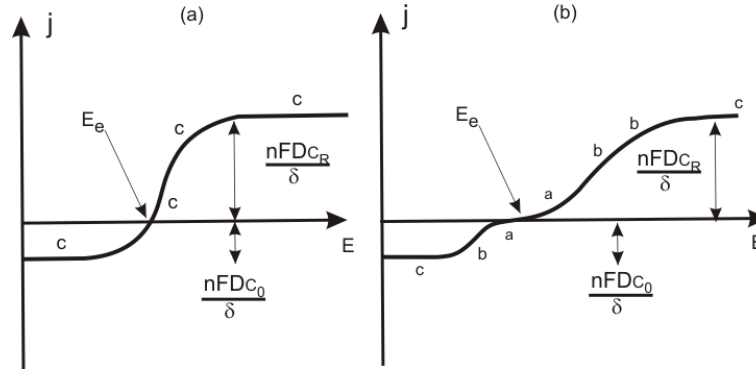


Figure 1.3: Complete polarization curves over a wide range of overpotentials for (a) reversible electron transfer and (b) irreversible electron transfer. $c_R = c_o$. a: electron transfer control, b: mixed control, c: mass transport control [25].

1.5 Role of hydrogen in metal electrodeposition process

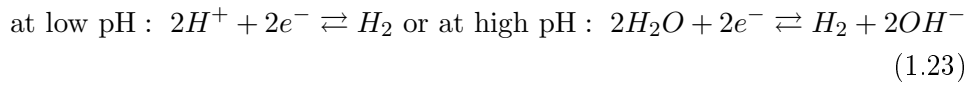
In electrodeposition processes hydrogen is often evolved as aside product at the cathode: in some cases it cannot be ignored.

During the cathodic electrodeposition of metals from aqueous solutions, three main types of reaction can occur [29].

Metal deposition:



Hydrogen evolution:



Metal ion reduction:



Oxygen reduction is, in principle, possible but can be neglected as, even with air agitation replenishment, its contribution is usually very small. Other cathode reactions are in practice also neglectable because either the kinetics or thermodynamics are unfavorable (e.g., hydride formation) or are dependent upon a special combination of chemical and physical conditions (e.g.,

cathode film formation). The principal cathode reaction is, in theory, a thermodynamic one; that is, the reaction which occurs at the least negative potential; e.g. silver deposition ($E^\circ = + 0.799$ V), is preferred to hydrogen discharge ($E^\circ = 0$) and e.g. hydrogen discharge to aluminium deposition ($E^\circ = - 1.66$ V); intermediate potentials give rise to mixed situations as for chromium ($E^\circ = - 0.74$ V). Reaction represented by Eq. (1.24) only occurs in practice for multivalent transition metals, e.g. copper, cobalt, tin, and represents 2-3% of the total current in most cases; it is generally neglected because the reverse can take place at the anode and if the net effect is small the two reactions are often not noticed.

The fact that electronegative metals can be electrodeposited at all derives from the fact that hydrogen has a large overpotential (up to 1.0 V), that is, it actually is evolved at much more negative potentials than the thermodynamic value because of other rate controlling steps in the discharge process. Such metals include nickel ($E^\circ = - 0.25$ V), and zinc ($E^\circ = - 0.76$ V) which may be efficiently deposited from aqueous solutions. The value of the hydrogen overpotential (η) depends upon several factors: (i) solution pH, (ii) current density (j) and Tafel parameters a and b , and (iii) the metal concerned, through its exchange current density j_0 .

In practical terms, the hydrogen overpotential can influence the cathodic current efficiency, CCE. Solutions in which reaction represented by Eq. (1.22) dominates have a CCE which tends towards 100% and the CCE falls as the j rises. Solutions where reaction represented by Eq. (1.23) dominates have low CCE or even 0% for very reactive metals such as Al, Ti ($E^\circ = - 1.63$ V), but for chromium it is $10 \pm 25\%$ and for manganese ($E^\circ = - 1.18$ V) $20 \pm 40\%$. The presence of complexants radically changes the situation because the discharge potential may be markedly lowered while the hydrogen overpotential may be only slightly affected by, for example, the pH. Thus, typical values of efficiency might be as shown in Table 1.2. In contrast to the case above, when the reaction given by Eq. (1.24) is favored over the reaction given by Eq. (1.23), e.g. for chromium, the CCE tends to increase with j (i.e., as j tends to 0%, the CCE tends to 0% as hydrogen is the sole reaction) and chromium is, therefore, the minor reaction electrochemically.

Bockris identified 5 steps in hydrogen evolution from acidic aqueous solutions [29] (cf. Table 1.3). By comparison, electrodeposition takes place in three, namely, the analogues of steps 1-3 (Table 1.3). The unique effects of

Solution type	CCE (%)
Acid copper	98
Alkaline cyanide copper	70-85
Acid zinc	>90
Alkaline zinc	70-90
Chromic acid	10-25
Alkaline tin	65-80
Acid tin	90-98

Table 1.2: Typical cathode current efficiencies during electrodeposition [29].

Reaction step	Rate-controlling process	Characteristic
1	Transport of H_3O^+ ions from the bulk of solution to the diffusion layer	
2	H_3O^+ ions are desolvated and partially discharged at the electrode surface $H_3O^+ + 2e^- \rightarrow H_{ad} + H_2O$ or $M + H_3O^+ + 2e^- \rightarrow M-H + H_2O$	Volmer rcs where $b = 0.118V$ if $\alpha = 0.5$ and $n = 1$
3	H atoms combine in the adsorbed state to form adsorbed H_2 molecules. Two alternative mechanisms are possible: (a) "Catalytic desorption" $M-H + M-H \rightarrow 2M + H_2(ad)$ (b) "Electrochemical desorption" $H_3O^+ + M-H + e^- \rightarrow M + H_2(ad) + H_2O$	Tafel rcs giving $b = 0.033V$ for catalytic behaviour theory. Heyrovsky rcs giving $b = 0.118V$: electrochemical theory.
4	Desorption of adsorbed hydrogen molecules as bubbles $nH_2 \rightarrow (H_2)_n$	Not electrochemical but affected by surface tension.
5	Diffusion of hydrogen bubbles and evolution of gas from the electrode surface.	

Table 1.3: The hydrogen discharge mechanism. The Tafel equation is of the form: $\eta = a + b \log j$ where η is the overpotential and j is the current density. The Tafel parameters are given as: $b = 2.303RT/\alpha nF$ and $a = b \log j_o$ where j_o is the exchange current density and α is the symmetry coefficient [29].

hydrogen can be seen as a consequence of steps 3-5 and can be stated as follows:

- Hydrogen absorption occurs in the substrate metal as H atoms not H_2 molecules but may gather as molecule bubbles in voids or vacancies thus leading to hydrogen embrittlement.
- Hydrogen bubbles cling to the surface in an adsorbed state; this leads to pore growth as the deposit forms around bubbles before they are released.
- Hydrogen bubble evolution can provide a stirring effect and lead to a substantial bubble raft at the solution free surface.

1.6 Electrocrystallization

Electrocrystallization (Fig. 1.4) occurs either by the build up of existing crystals or the formation of new ones [30]. These two processes are in competition with each other and are influenced by different factors. The two key mechanisms which have been identified as the major rate-determining steps for nanocrystal formation are charge transfer at the electrode surface and surface diffusion of adions on the crystal surface [26]. The second important factor in nanocrystal formation during electrocrystallization is overpotential. Grain growth is favored at low overpotential and high surface diffusion rates. On the other hand, high overpotential and low diffusion rates promote the formation of new nuclei.

Electrocrystallization (i.e., the nucleation and crystal growth in electrochemical systems under the influence of an electric field) can be treated in a similar manner to that of deposition from a vapor phase. The phase transformation, i.e. liquid to solid phase will occur when free energy change ΔG has a negative value.

Sketches of the the various stages in the formation and growth of a single nucleus of the metal on the inert substrate are given in Fig. 1.5. A rather idealized cathode surface, smooth and even defect free is assumed. The steps in overall process are:

- (i) transport of solvated metal ions through the solution to the electrode surface
- (ii) electron transfer

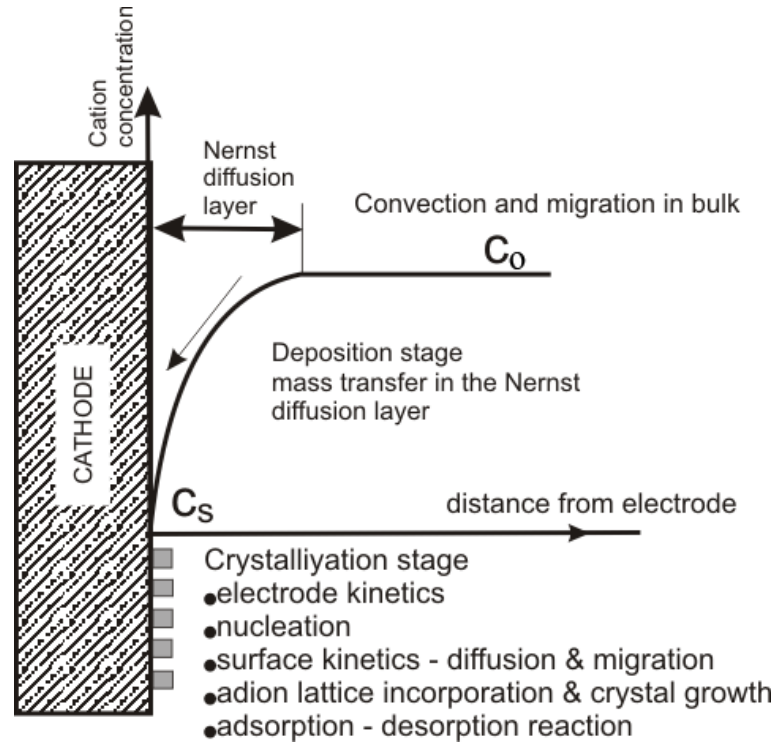


Figure 1.4: Two stages of electrodeposition process according to Bockris [26].

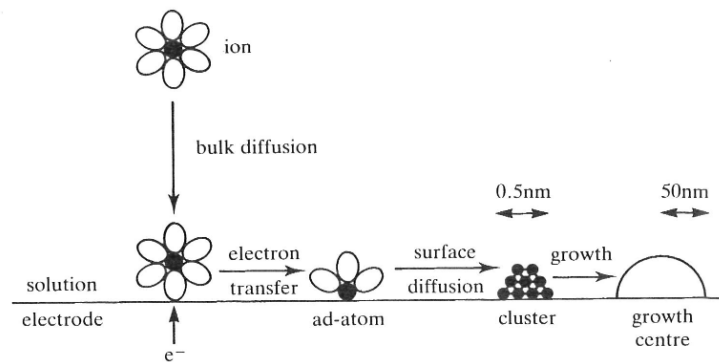


Figure 1.5: The stages in the formation of a stable, growing nucleus of a metal on a inert carbon substrate [25].

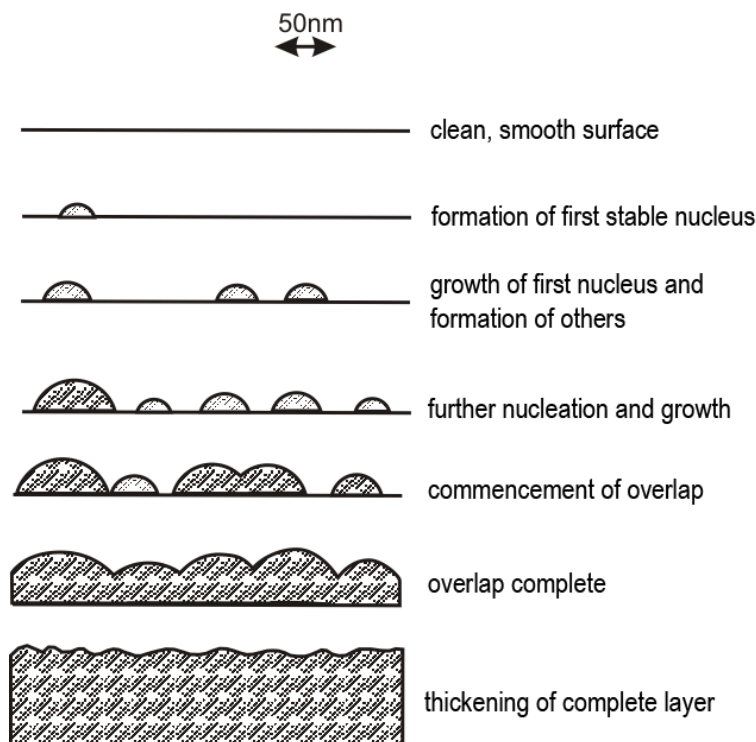


Figure 1.6: The various stages in the deposition of a thick layer of a metal on an inert substrate [25].

- (iii) partial or complete loss of the solvation sheath to form an adatom
- (iv) surface diffusion of adatoms
- (v) clustering of adatoms to form a nucleus of sufficient size for it to be stable
- (vi) growth of the nucleus by incorporation of adatoms to favourable sites in the lattice structure of the metal.

The growth of macrodeposit in case of progressive nucleation and three dimensional nucleation is schematically represented in Fig. 1.6. Formation of nuclei leading to the deposition of the thick layer of deposit is a multistep process and each of the processes can be the rate determining step.

1.6.1 Nucleation and Growth

Nucleation is ideally classified as either instantaneous or progressive, and the growth mode can be one-, two-, or three-dimensional, with the resulting shape of growing crystallites being, for example needles, discs and either

cones or hemispheres, respectively. The rate determining step may be charge transfer, diffusion or electrocrystallization. Different combinations of nucleation type, growth mode, and rate determining step yield different functions of current density as a function of time. The nucleation process on real crystalline substrates (i.e., those with crystal defects and/or inhomogeneities that result in preferred nucleation sites) with a number, N_0 , of randomly distributed active sites may be described by the following general first order kinetic law [31, 32]

$$N = N_0[1 - \exp(-Jt)] \quad (1.25)$$

Where N is number of sites converted into nuclei at time t and J is a nucleation rate constant (the inverse of the mean nucleation time) and N_0 is saturation nucleus density. When A is very high, $N \approx N_0$, all surface sites are converted immediately into nuclei, and nucleation is said to be “instantaneous”. On the other hand, when A and t are both small, $N \approx AN_0t$, the number of nuclei depends on time, and nucleation is termed “progressive”. In this case, nuclei appear arbitrarily in space and time, eventually forming a monolayer. Following instantaneous nucleation, the centers would be expected to be the same size while progressive nucleation would be expected to lead to broad range of sizes.

The phase transformation, i.e. liquid to solid phase will occur when free energy change ΔG has a negative value.

$$\Delta G = \left(\frac{4}{3}\pi r^3 \Delta G_v + 4\pi r^2 \gamma\right) \quad (1.26)$$

The first term in equation is the volume free energy change upon formation of a nucleus and is negative in sign and it is directly related to the substrate temperature and the deposition rate. The second term is positive and proportional to the surface area. Small centers are therefore unstable because they have a high ratio of surface area/volume; ΔG in Eq. (1.26) is positive. Nuclei having their radius less than the value at which ΔG is maximum will tend to spontaneously dissolve since this will lead to reduction of free energy. So for a stable nucleus to form, its radius should be greater than a critical radius at which $d\Delta G/dr$ changes its sign from positive to negative (Fig. 1.7).

Volmer and Weber [33] derived an equation for deposition rate:

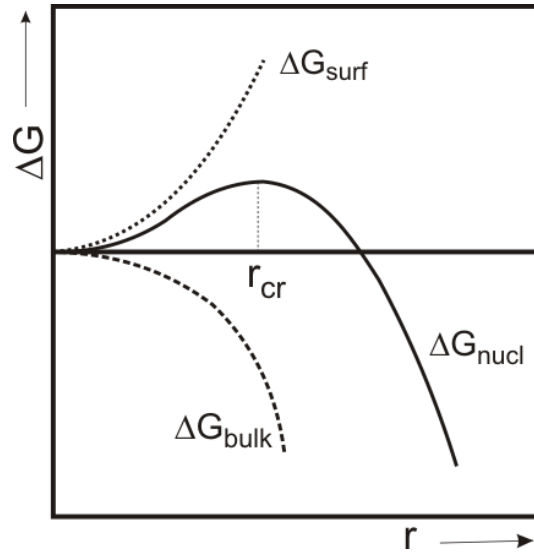


Figure 1.7: Gibbs energy of nucleation as a function of radius, r_{cr} is the size where the nucleus become stable [28].

$$J = A \exp\left(\frac{-\Delta G_{crit}}{kT}\right) \quad (1.27)$$

where k is the Boltzmann constant. The classical expression for steady state nucleation rate based on dependance between Gibbs free energy and overpotential Eq. (1.3) after calculation of ΔG_{crit} and forming the logarithm, it is possible to obtain following equation for the nucleation rate J :

$$\ln J = \ln A - \frac{B}{\eta^2} \quad (1.28)$$

This equation was confirmed by most experiments regardless of the continuing discussion of the validity of classical approach [28]. Clearly, for the nucleus to become stable, it must reach critical size and this can be achieved only if the adatoms collect together very rapidly. In electrocrystallization, of very high concentration of adatoms is favored by using a solution with a high concentration of metal ions and driving the electron transfer process hard by applying a sufficient overpotential.

The most important parameters determining the mode of growth of a substance on a foreign substrate are the deposit/substrate binding energy and the crystallographic misfit between them. Considering the deposition process at nearly equilibrium conditions, that is, small supersaturation and

negligible kinetic influences, a deposit may grow on a substrate by different modes [31].

First, if the interatomic interactions between substrate and deposits are stronger and more attractive than those between the different atomic species within the deposit, growth takes place layer-by-layer according to the Frank-van der Merwe model [34] up to the disappearance of the strong substrate-deposited substance attraction. Second, in the opposite case, where the interatomic interactions between substrate and deposits are weaker and less attractive, formation of three-dimensional islands occurs according to the Volmer-Weber model. Third, for intermediate interactions strength, formation of strained two-dimensional layers is followed by growth of unstrained three-dimensional islands according to the Stranski-Krastanov model [35].

The strain resulting from lattice mismatch contributes to the interface energy, a key parameter in determining the growth mode [34]. However, the surface free energies for the substrate and deposit materials also influence the mode of growth.

The formation of nuclei of radius greater than a critical radius r_{cr} occurs until further nucleation is not possible as the energy situation of growth becomes more favorable and growth of existing nuclei takes place by the addition of more atoms. In most common Frank-van der Merwe model, the simplest energetic interpretation is that the atom attaching to the growth layer edge makes two or more bonds while one connecting to the top surface makes only one, and hence reduces the interfacial energy by much more [36]. In a kinetic interpretation the atom attached to the top of the surface will diffuse quickly until it encounters a new layer edge, and, now having two bonds, thereafter will have a much lower probability of moving back to the surface.

In Volmer- Weber growth mode, nucleation of islands is favored over extended growth at layer edges as in Frank-van der Merwe model. Increasing the nuclei density, i.e. the deposition rate enhances nucleation to occur under this type. Temperature additionally controls the surface diffusion of the atoms.

In Stranski-Krastanov growth mode, the growth changes from monolayer to island after formation of one or two monolayers. Explanation is attributed to the stress increase and thus strain relief after the formation of few monolayers caused by mismatch in the lattice spacings.

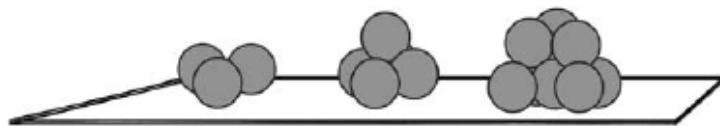


Figure 1.8: Different nucleus models on a surface (a) a cluster of three atoms, (b) a cluster of four atoms and (c) a cluster of ten atoms in more or less a semi-sphere [28].

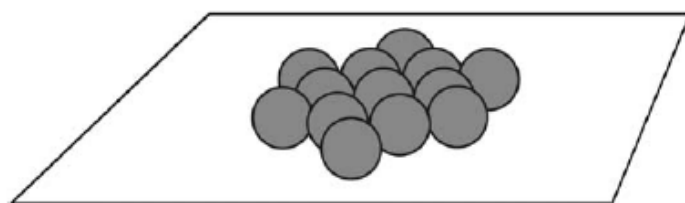


Figure 1.9: A two-dimensional nucleation with the nucleus in the approximate form of a circle [28].

1.6.2 Three-dimensional nucleation

In electrochemical phase formation nucleation must be on a surface of a foreign or native substrate. If the nucleus formed on a surface is a cluster that grows in all three dimensions, one speaks of a three-dimensional nucleation. The nucleus is a cluster of only a few atoms and can be depicted as a semi-sphere (Fig. 1.8). The nucleation of 3-D nuclei takes place either by surface diffusion or by direct impingement of atoms, often at active sites such as crystal defects, atomic step or impurities. These sites act as a means for reducing the activation energy for nucleation or bonding of the nuclei to the substrate. In principle, a thick layer can be formed simply by a continuation of the growth process.

1.6.3 Two-dimensional nucleation

Sometimes a two-dimensional nucleus forms on a surface (Fig. 1.9) which leads therefore to a mono layer growth because of the strong interaction between the substrate and deposited metal as in under potential deposition. This cluster of N atoms almost has a circular shape.

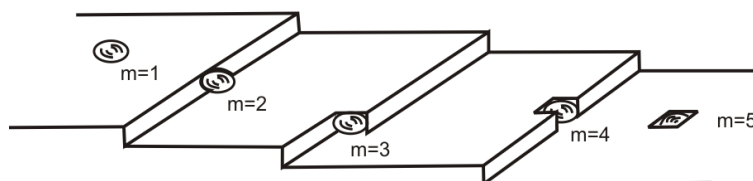


Figure 1.10: The cubic coordination sites in the lattice of perfect single crystal (i) surface sites $m=1$, (ii) edge sites $m=2$, (iii) kink sites $m=3$, (iv) edge vacancies $m=4$ and (v) surface vacancies $m=5$, taken from [25].

The many defects on the surface of a real crystal form nucleation centers. After switching to a potential in the deposition region, there will already be a fixed density of defects N_0 where local growth can start.

At the microscopic level, the phase growth process involves the incorporation of atoms in lattice sites at the surface of the solid. Even on a perfect single crystal, there are a number of different types of site (Fig. 1.10). Adatoms are formed over the whole surface of the metal center but they then diffuse across the surface to site where they can be coordinated by several other atoms, i.e. edge and kink sites. The free energy of the lattice formation becomes more negative as the coordination number of the site increases. In real, macroscopic solid, the situation is complicated by the presence of defects which propagate as atoms are incorporated while maintaining constant the number of sites where further lattice expansion is energetically favorable.

1.7 Two sides of the interface

An essential objective in electrochemistry is to understand the electron transfer event at the electrode surface. The electron must pass between a delocalized energy level in a metal and an orbital localized on an ion or molecule in solution. For simple electron transfer reactions, the detailed structure of the surface is assumed to be unimportant. On the other hand if any reaction involves the adsorption of species from the solution and possibly heterogeneous chemical reactions, the surface structure becomes critical since it determines the relative positions and separations of adsorption sites. Usually, polycrystalline metal electrodes are used in electrodeposition. The surface of such electrodes are not flat on atomic dimensions. Each will have a number of steps, probably randomly spaced, across its surface and there will also be

the other types of sites shown in Fig. 1.10. The overall effect is production of a surface which is a complex collection of single crystal faces.

From the view point of understanding surface chemistry, the key feature of single crystal faces, formed through cutting the perfect crystal at a defined angle, is that each has a characteristic geometric arrangement of atoms. Different local arrangement of atoms are quite different for different crystal planes of cubic structure (e.g. Cu or Pt) causing as consequence different catalytic abilities. Investigation of surface structure of single crystal Pt in ultra high vacuum before and after electrochemical investigation revealed that the free energy of adsorption of hydrogen atoms depends strongly on the single crystal face used [25].

Particular chemistry may be promoted by favorable local arrangements of metal atoms in the surface. In addition, to occurring in the single crystal faces, they can also arise at defects in the lattice and at grain boundaries. Therefore, the rate of reaction is commonly very dependant on on the preparation of the metal (particle size, grain size and surface chemistry) and its coverage by impurities. It must be emphasized that the surface of most metals is readily oxidized when contacted with air or when in solution if its potential is allowed to stay positive of a very restricted range. Universally, such oxide layers would be expected to have diametrical effect on the adsorption and chemical properties of the bare metal surface. Their effect depends on the thickness and properties of the oxide.

It should be stressed that the properties of the interface also result from the properties of both the metal and the solution as well as the interactions between the two phases.

1.8 Interfacial region-electrochemical double layer

When potential is applied to an electrode in a solution electrolyte, its surface will become charged, with a value that depends on the material of the electrode, the electrolyte and the potential. The charge on the electrode surface is always balanced by attracting ions of opposite charge from the bulk solutions to the vicinity of the surface causing formation of electrical double layer with potential of zero charge E_{pzc} .

When the potential in aqueous solution is made more negative than E_{pzc} , the surface of the electrode will be negatively charged and cations and

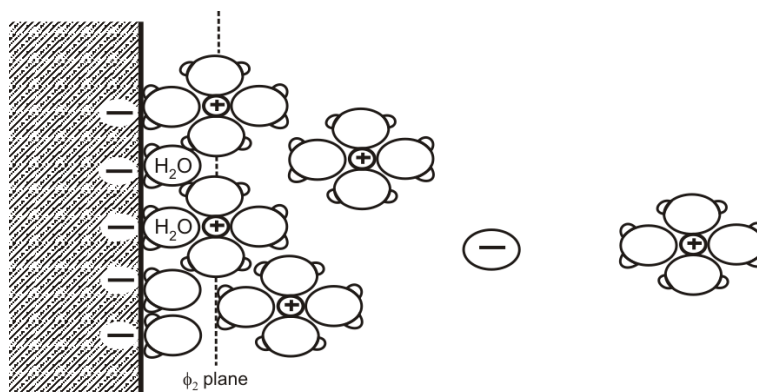


Figure 1.11: Model of the interfacial region at the electrode surface for potentials negative to the potential of zero charge [25].

dipoles, particularly water molecules will be attracted to the surface forming a compact double layer at the plane of closest approach, known as the ϕ_2 plane (Fig. 1.11). The neighboring region of solution is called the diffuse double layer and is a region of much less organization where the number of cations exceeds the number of anions to complete the balance of the negative charge on the electrode. The opposite case is when the potential is made more positive than E_{pzc} .

1.9 Microstructure

In order to predict properties, it is essential to understand how the structures vary with decreasing crystallite sizes, since for all superior properties of the nanostructured materials, the grain size is the dominant structural parameter governing a material's properties. Therefore, microstructural investigations are essential to elucidate the underlying mechanisms. An appropriate way to investigate the microstructures of nanocrystalline materials is to image them in a transmission electron microscope (TEM). The crystal structure of electrodeposits is strongly dependent to the relative rates of formation of crystal nuclei and their growth [37]. Finer-grained deposits are the result of conditions that favor crystal nuclei formation while larger crystals are obtained in those cases that favor growth over nucleation. Generally, a decreasing crystal size is the result of factors which increase cathodic polarization (Eq. 1.28). Electrodeposition processes have numerous variables that influence structure, e.g., metal ion concentration, additives, current density,

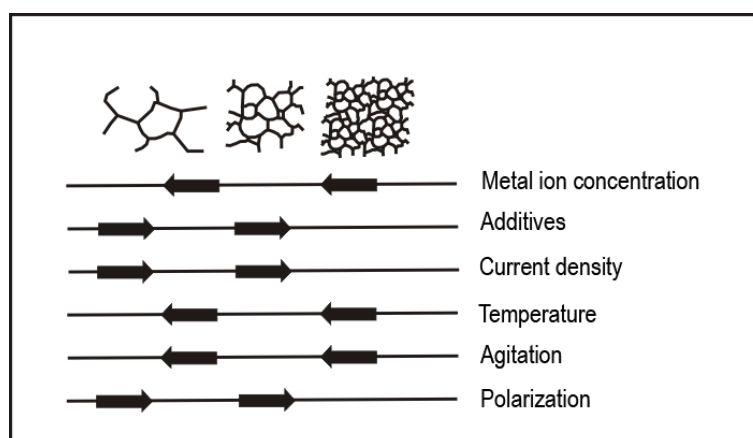


Figure 1.12: Schematic representation of the dependance of deposition parameters on grain size of electrodeposits, taken from [37].

temperature, agitation, and polarization. Schematic representation of the influence of individual plating variables on structure of electrodeposits is shown in (Fig. 1.12).

The structure of most electrodeposits is determined by epitaxial and pseudomorphic growth onto a substrate and by the conditions prevailing during deposition. Typically, a deposited metal will try to copy the structure of the substrate and this involves epitaxy, which occurs when definite crystal planes and directions are parallel in the deposit and substrate, respectively. Epitaxy is the orderly relation between the atomic lattices of substrate and deposit at the interface, and is possible if the atomic arrangement in a certain crystal direction of the deposit matches that in the substrate. The structure of a deposit, physical properties and adhesion of deposit to the substrate can be noticeably influenced by the substrate upon which it is plated.

1.10 Surface morphology of electrochemical deposits

Morphology is an important property of electrodeposited metals. It depends mainly on the kinetic parameters of the deposition process and on the deposition overpotential or current density. The morphology of an electrodeposited metal depends also on the deposition time until the deposit has attained its final form.

Electrodeposition can give rise to the following morphologies of deposited layers:

- compact
- dendritic
- spongy or granular.

On the other hand, it is known that the morphology of electrodeposits can be substantially changed if the electrodeposition is carried out in the presence of organic or inorganic additives. For example, a smooth deposit can be obtained in the presence of additives instead of a rough one in the absence of additives [38]. Crystalline metal electrodeposits exhibit several types of growth forms including layers, blocks, pyramids, ridges, spiral growth forms, dendrites, powders, and whiskers [38]. These morphologies have been studied extensively and various models have been advanced to correlate specific growth forms with electrodeposition parameters and substrate microstructure. Electrodeposition parameters like bath composition, pH, temperature, overpotential, bath additives, etc., and microstructural features of the substrate including grain size, crystallographic texture, dislocation density and internal stress influence not only the microstructure but also the final morphology of the deposited layers.

1.10.1 Compact nanocrystalline deposits

For a given quantity of deposited metal, in general - under mixed kinetic control - the surface coarseness is positively correlated with the current density. In particular, charge-transfer controlled electrodeposition gives rise to large grains with generally well-defined crystallite shapes. This second fact has been explained by the differences of j_o on the different developing crystal faces, while the Nernst potential is very similar: this can lead to the preferential growth of given crystal planes, because the growth rate chiefly depends on the orientation [39]. This behavior breaks down in the case of even limited mass-transport contributions to kinetic control. Therefore at the onset of mixed control conditions, morphological changes are observed from the growth of large crystallites to compact micro- and nanocrystalline deposits [40].

1.10.2 Disperse nanocrystalline deposits

If an ellipsoidal feature is considered, spherical diffusion takes place only around the tip of the protrusion assuming it to be $\leq 100\mu\text{m}$. Deposition on the protrusion tip can occur under pure charge-transfer control (at overvoltages lower than the critical one for the growth of dendrites), while on the rest of the cathode mixed control prevails [41]. Some of the new nuclei can be precursors of carrot- or needle-like protrusions, depending on their crystal orientation and position with respect to other protrusions [3].

In conditions close to full diffusion control, disperse - i.e. dendritic, powdered or spongy - deposits can be obtained by the different mechanisms presented in this section.

A dendrite can be defined as a protrusion growing under charge-transfer control, while electrodeposition on the rest of the cathode goes on under diffusion control [38]. Dendrites of Cu, Cd, Pb, Sn, Ag have been reported [3]. Dendrites develop if a critical overvoltage is exceeded and display a highly ordered structure, growing and branching in well-defined directions. The branches typically display nanometric dimensions. Dendritic growth is favored by decreasing the concentration of the depositing ions, increasing the concentration of the supporting electrolyte and the viscosity of the bath as well as by decreasing the temperature and stirring.

Powdered deposits basically represent dendritic electrodeposits which spontaneously fall apart during growth or which can be broken by mechanical action. All metals which can be electrodeposited exhibit a tendency to appear in the form of powders at current densities larger than a critical value [38]. It has also been observed that the product of the current density with the square root of the time for the onset of powder formation is a constant within limits as can be expected for a diffusion-controlled process. Increasing the overvoltage leads to the formation of less dispersed powder with lower average particle size. Cu and Ag powders consisting of micrometric aggregates of nanometric crystals have been produced by electrodeposition [3]. Electrolyte concentration, stirring rate and temperature have been shown to have the effects on powder quality (ability of the powder to be well pressed and sintered after production) which can be expected from the dendritic growth mode. The morphology of the powders is affected by galvanostatic or potentiostatic deposition modes: the former gives rise to less branched powders because the overvoltage decreases during the growth process [3].

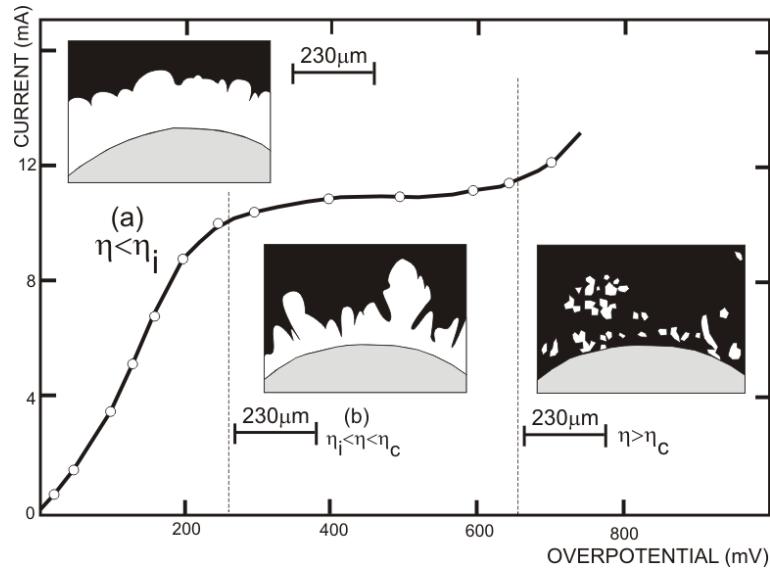


Figure 1.13: Polarization curve for the potentiostatic deposition of copper. (a) Overpotential: 200 mV, deposition time: 6 hours; (b) Overpotential: 300 mV, deposition time: 5 hours; (c) Overpotential: 700 mV, deposition time: 2 min [38].

The growth of protrusions in all directions under spherical diffusion control giving rise to branching and interweaving protrusions has been denominated spongy growth [42]. Typical spongy electrodeposits with nanometric grains and filaments are formed during the growth of e.g. Zn and Cd at low overvoltage under conditions of low nucleation rate. The mechanism for the development of a spongy morphology is not yet fully understood, nevertheless it seems that the initiation of spongy growth is due to the amplification of surface protrusions within the spherical diffusion layer forming around each independently growing grain. Initially hemi-spherical diffusion predominates around the growing protrusions. As deposition progresses the diffusion hemispheres expand and merge into a single planar layer.

In Fig. 1.13, the polarization curve for copper electrodeposition is shown, as well as cross sections of electrodeposits obtained in different overpotential ranges. Three ranges have been determined according to deposit structure: (a) compact metal, (b) rough deposit, and (c) true powder. These results show clearly that a distinction has to be made between rough and powdery deposits. Obviously, the powder deposit is formed only at the end of the polarization curve plateau, at overpotential/ current density values larger

than the critical values, as illustrated by Fig. 1.13. Hence, in potentiostatic electrodeposition of powders, the overpotential must be larger than the overpotential corresponding to the end of the limiting diffusion current density plateau (i.e. $\eta > \eta_c$). Correspondingly, in galvanostatic powder deposition, the current density must be larger than the limiting diffusion current density. This situation occurs when the diffusion rate is slow compared to charge transfer and the diffusional process cannot supply the reactants fast enough to the surface (mass-transport control). In other words, the criterion for obtaining powdery deposits is that the electrode process must be controlled by the diffusion of ions to the electrode surface, rather than the kinetics of the electrodeposition.

Powders are typically obtained from qualitatively the same, but less concentrated, solutions as used in electrowinning and are produced at higher current densities. All metals that can be electrodeposited exhibit a tendency to appear in the form of powders at current densities larger than a certain critical value. A powder formed by the electrolytic technique is often dendritic or spongy in shape although considerable control of particle size and shape is possible. The specific properties of the powder depend on the electrolytic bath conditions during deposition and on the subsequent processing steps. At low current densities the discharge of ions occurs slowly, and so the rate of the growth of the nuclei should exceed the rate at which new ones form; the deposits obtained under these conditions should be coarsely crystalline. As the current density is raised the rate of formation of nuclei will be greater and the deposit will become finer-grained. At very high currents the solution in the vicinity of the cathode will be depleted in the ions required for discharge, and, as a result, the crystals will tend to grow outwards towards regions of higher concentration; the deposit then consists of “trees”, nodules or protruding crystals. If the current density exceeds the limiting value for the given electrolyte, hydrogen will be evolved at the same time as the metal is deposited; bubble formation often interferes with crystal growth, and porous and spongy deposits or powders may be obtained.

1.10.3 Fractals

Basically, a fractal is any pattern that reveals greater complexity as it is enlarged and is made of parts that are in some way similar to the whole [36]. Fractals were first described mathematically by Mandelbrot and a classical

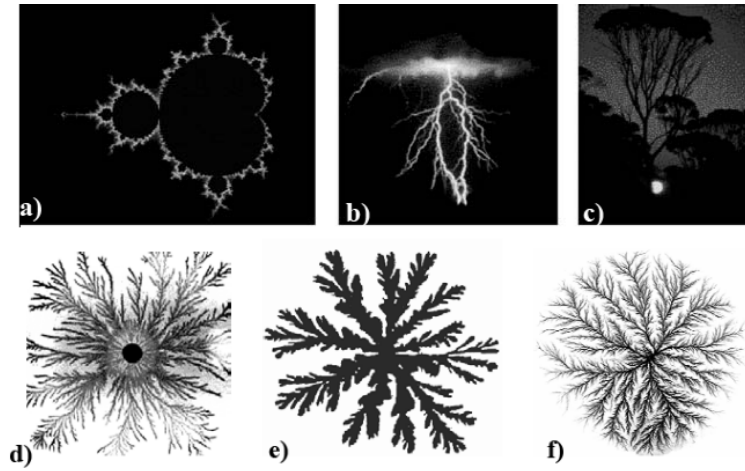


Figure 1.14: Examples of fractals; a) classical Mandelbrot fractal image, b) lightning fractal, c) fractal image of a tree canopy, d) image formed by the growth of bacteria on a planar support, e) Hale-Shaw image generated by the injection of gas into a layer of viscous liquid and f) Lichtenberg image formed by an electric discharge inside a dielectric ; images a), b) and c) are all from clipart files derived from the copyright-free public domain [36]; images d), e) and f) are from the reference [43].

example of a Mandelbrot fractal shape is shown in Fig. 1.14a [36, 43].

Additional examples of fractals in nature are shown in Fig. 1.14. Many technically relevant processes of electrochemical growth develop self-affine fractal surfaces rather than euclidean ones, owing to the presence of non-equilibrium conditions [3]. Growth models for phase growth far from equilibrium imply a flux of incoming particles which is much faster than the mass transport along the growing surface, such as surface diffusion or surface-tension relaxation. These models can be formulated according to a discrete, atomistic approach, such as Monte Carlo or Molecular Dynamics or by continuous motion equations [3]. Typical continuous models comprise a roughening term - linked to the stochastic arrival of depositing particles - and a smoothing one resulting from surface diffusion and surface-tension relaxation. Among other approaches, the dynamic scaling theory provides a framework for understanding fractal-like morphologies of electrodeposits, by allowing the estimation of parameters from images of the surfaces and to relate them to growth modes. From the analysis of surface profiles resulting from high lateral-resolution imaging procedures, such as STM and AFM images, the dynamic scaling parameters α (roughness exponent), β (growth

exponent) and z (coarsening exponent) can be estimated from equations Eq. (1.29) to Eq. (1.31):

$$\Delta(L) \sim L^\alpha \quad (1.29)$$

$$\Delta(L, t) \sim t^\beta \quad (1.30)$$

$$t_x \sim L^z \quad (1.31)$$

where: Δ is the standard deviation of the interface height, L is the dimension of the surface, and t_x is the transition time such that for $t > t_x$ the surface becomes a scale-invariant self-affine fractal. Fractal quantities can also be derived from digitised micrographs. The different numerical values of α , β and z correspond to different growth models. Fractal geometry is an efficient tool for characterizing irregular patterns like highly branched dendritic deposits. Electrodeposition of zinc has been demonstrated as one of the real physical systems which exhibits a structure similar to the theoretical diffusion-limited aggregation (DLA) model [44]. The observed patterns fall into three classes of deposits: (a) fractals resembling DLA aggregates, (b) dendrites with stable tips and (c) dense radial structures. The two-dimensional zinc deposits of a class (a) bear a striking resemblance to computer generated fractal patterns and their fractal dimension is 1.7, remarkably close to the computer simulated value of 1.71. The fractal (Hausdorff) dimension is usually determined by digitizing photographs and taking the best-fit slope of $\ln(N)$ vs. $\ln(r)$, where $N(r)$ is the number of pixels covering the fractal.

1.11 Catalytic properties of electrodeposits

The aim of electrocatalysis is to design the electrode surface in a way that provides a high current density (high rate of reaction) close to the equilibrium conditions (at low overpotentials) [25]. The main characteristics of electrocatalytic reactions can be categorized into three main groups:

- The electrode material determines strongly the kinetics and the mechanism of the reaction. Materials like metals, alloys, oxides or transition

metal complexes are usually good electrocatalysts.

- The current density depends on the real surface area. The rate of the reaction actually reflects the number of sites available, it therefore can be enhanced by preparation of porous, rough or other high area surfaces.
- The formation of the key intermediate can be blocked by substances that inhibit adsorption (some organic or inorganic species act as a poison).

Many electrocatalytic reactions are important in electrochemical technology [25]. Metal nano- and microparticles are technologically important electrocatalysts. For example, nanoparticles having a composition of $\text{Pt}_{0.5}\text{Ru}_{0.5}$ are one of the most efficient catalysts for the oxidation of methanol in the direct methanol fuel cell [45]. Silver nanoparticles are excellent catalysts for the reduction of oxygen in basic aqueous solutions, and nanoparticles of pure platinum are efficient catalysts for oxidizing a variety of molecules, including oxygen (in acidic solutions) and many organic molecules and alkenes [45]. On semiconducting TiO_2 surfaces, platinum nanoparticles have also been employed as photocatalysts to effect the light-driven splitting of water into H_2 and O_2 . Although metal nanoparticles are important electrocatalysts, electrodeposition has rarely been employed by electrochemists to prepare metal particles. Instead, nanometer-scale metal particles have usually been synthesized by impregnation of a catalyst support (e.g., porous carbon) with an aqueous metal salt solution followed by drying and gas-phase reduction of the dispersed salt at high temperature in H_2 . A second route to metal nanoparticles involves the evaporative deposition of metal atoms onto a surface from a hot filament source in vacuum (physical vapor deposition). One reason electrodeposition has been virtually excluded from consideration is because it has been impossible to produce dispersions of metal particles exhibiting a reasonable degree of size monodispersity [45]. The difficulty in production of dimensionally uniform structures by electrodeposition is often the progressive nucleation of metal particles where new particles are formed continuously during the application of a voltage pulse. If nucleation is progressive, the number density of particles on the surface increases as a function of time, and late nucleating particles are small compared with early nucleating particles and broad particle size distributions are obtained. The

topography of real solid surfaces plays an important role in defining the electronic energy distribution at surface sites, particularly when irregularities at the atomic level are taken into account. Likewise, surface irregularities at the nanometric level determine the electrocatalytic properties. In fact, the reactivity of small metal clusters has been found to vary by orders of magnitude when the cluster size is changed by only a few atoms. Furthermore, the high surface to volume ratio as well as the very small particle size provide nanostructured catalysts with unique properties [46].

It must be emphasized that the key factor in the determination of the catalytic activity is the electronic structure of a particular catalyst. Therefore, almost all catalysts contain transition metals or their ions since the catalysts must have electrons and/or unfilled orbitals to form bonds of appropriate strength. Usually intermediate bond strength between adsorbate and surface leads to the strongest catalysts [25]. The transition metal center in the catalytic mechanism can play an important role since it can exist in several oxidation states.

1.12 Stress in electrodeposition

Although the internal stresses (macrostresses) generated during electrocrystallization of metals and alloys have been known for over a century, there is still no unified theory which quantitatively describes their origin. Conversely, numerous hypotheses have been proposed to explain the particular experimental observations. In the majority of these hypotheses, the factors causing the change of deposit volume are considered: coalescence of crystallites, incorporation of hydrogen, occlusion of other foreign species, or generation of structural defects [37]. The theory based on the crystallite joining was first postulated by Kohlschutter and Jacober and it suggested that the deposit forms first in a dispersed state and then recrystallizes. Since it was doubtful that the recrystallization process generally takes place at deposition temperatures, other explanations were later proposed. They assume that when the individual crystallites grow, the attractive forces attempt to cancel the gap between them. Because the interaction of the substrate hinders any displacement, a stress results. Microscopic observations established that this was also essentially true after the deposit became continuous. The continuous coalescence of columnar grains with gaps between them is necessary

for deposit thickening. Since the volume decrease results from the joining of individual crystallites, one might expect a strong relationship between the stress and the parameters characterizing the deposit microstructure. Occasionally stress may serve a useful purpose. For example, in the production of magnetic films for use in high speed computers: stress in iron, nickel, and cobalt electrodeposits will bring about preferred directions of easy magnetization and other related effects [37].

Typically, with most deposits, there is a high initial stress associated with lattice misfit and with grain size of the underlying substrate. This is followed by a drop to a steady state value as the deposit increases in thickness. With most deposits this steady state value occurs in the thickness regime of 12.5 - 25 μm : the finer the substrate grain size, the more rapid this descent [37]. Atomic mismatch between the coating and substrate is a controlling factor for thin deposits. For example, when gold is plated on silver, the influence of mismatch is almost absent because the difference in the interatomic spacings of gold and silver is only 0.17%. This is quite different for copper and silver since the difference in this case is about 13% [47]. The initial high stress is due to lattice misfit and grain size of the underlying metal. With fine grained substrates, the maximum stress is higher and occurs very close to the interface. In terms of adhesion, the ideal case which would provide a true metallic bond between the deposit and the substrate is that wherein there is epitaxy or isomorphism (continuation of structure) at the interface. Although this often occurs in the initial stages of deposition, it can only remain throughout the coating when the atomic parameters of the deposit and the substrate are approximately the same.

Mainly three kind of stress exists in plating deposits [48] due to existence of lattice misfit between coating and the substrate, thermal stress in the thermal coefficient of expansion between the coating and the substrate and stresses caused by particular plating or bath conditions.

The origin of residual stresses in thin films can be attributed to the [49]:

- Epitaxial stresses

Epitaxial stress arise when the crystal lattice in films and substrates has perfectly coherent interfaces. The epitaxial strain gives rise to a misfit stress. Generally, a difference in the lattice constants of the deposit and the substrate leads to a stress at the interface. The influence of these

misfit stresses is only significant in the initial phase of deposition [50], because of the local lattice adaption at the interface area. When the film thickness increases, it becomes energetically favorable for misfit dislocations at the interface between film and substrate to reduce the stress in the film.

The mechanical behavior of metals is now known to be determined primarily by lattice defects called dislocations. Most of the recently developed theories (Fig. 1.15) [37] about the origins of internal stresses in deposited metals have included aspects of dislocation theory or they are totally based upon it. Of these theories, the best developed is one which explains the misfit stresses between a deposit and a substrate of a different metal when the former continues the structure of the latter. Furthermore, misfit stress can arise between the grain boundaries because of a different crystal orientation of neighboring grains.

- Thermal stresses

These stresses arise due to differences in the thermal expansion coefficients at the interface between the substrate and the deposit [48]. For the stress aspect the deposition process plays a key role. At first it should be noted that the deposition takes place at elevated temperatures. When the temperature is decreased, the volumes of the grains shrink and the stresses in the material increase during cooling down to room temperature.

- Intrinsic or growth stresses

These stresses arise during deposition because generally films are deposited under non-equilibrium conditions [49].

Generally, intrinsic stresses are caused by some of the following growth processes [49].

- Coalescence of Grain Boundaries

Individual islands formed first during deposition on a substrate usually exhibit compressive stress [51]. The Volmer- Weber growth mode proceeds by the initial formation of individual islands, followed by their coalescence into a continuous film. For a given amount of deposited film material, the

free energy of a morphology having large islands is less than one having smaller islands [52]. Compressive stresses prior to coalescence have been attributed to the Laplace pressure, where the pressure inside a small solid crystallite is larger than the outside pressure, associated with surface energy effects. The subsequent tensile stresses observed during and after island coalescence are usually attributed to grain boundary formation or to grain growth [51]. Reduction of the total free energy can be achieved by “zipping up” the interfaces, since the interfaces possess lower free energy in comparison to the surface energy of isolated islands. The participating islands become elastically strained and a tensile stress is generated [53].

- Grain growth

Reduction of the grain boundary area provides a driving force for grain growth. Since grain boundaries are less dense than the lattice [49] the elimination of grain boundaries leads to a densification of the film and, therefore, to an increase of the tensile stress.

- Annihilation of Excess Vacancies

The annihilation of vacancies produces a local volume change that may lead to stresses in the film when it is attached to the substrate, depending on where the vacancy is annihilated [49]. If the vacancies annihilate at the free surface, at the interface of the film or at a horizontal boundary no additional stress is generated. Annihilation at a vertical boundary results in an in-plane change of the film dimensions and in the development of a tensile stress [49].

For low temperature deposition, the generation of stress caused by the annihilation of vacancies is not significant [49].

- Insertion of Excess Atoms

Two model mechanisms proposed that the growth process in thin film occur either by crystal growth or by incorporation of excess atoms at the grain boundaries [51]. The new layer formed by traditional crystal growth by templating into the underlying crystal lattice and repeating the stress state of the previous layer as long as no relaxation is present (e.g. dislocation formation). The second mechanism is driven by the difference in the chemical potential between the free surface and the trapping site and can result in a

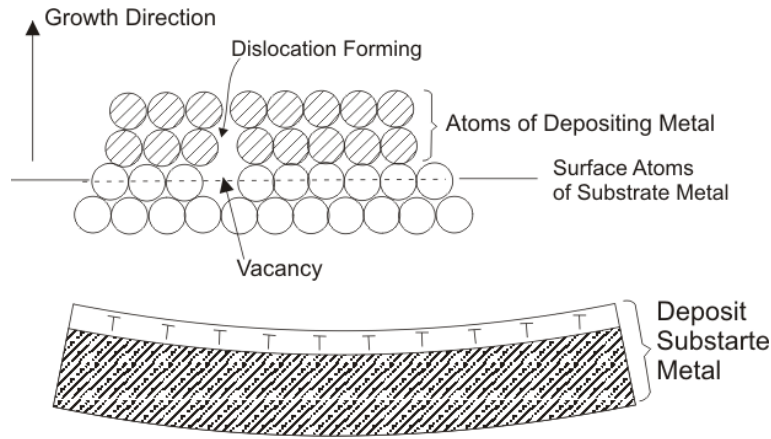


Figure 1.15: (Top) Edge dislocation forming in an electrodeposited metal near a surface vacancy in the basis metal. (Bottom) How an array of dislocations produces a tensile stress in electrodeposits, taken from [37].

driving force for diffusion of adatoms onto the trapping site which creates a compressive stress in the film [54, 51, 55].

- Impurity incorporation

A compressive stress can be caused by incorporation of different impurities into the electrodeposited Ni film [55]. Usually, the impurities found most frequently are carbon, sulfur and oxygen, although hydrogen can remarkably influences presence of stress in electrodeposited films [55] inducing a compressive stress when incorporated into Ni. Generally, electrodeposition is very complex process and the majority of the models describing stresses are developed for vacuum deposited films [55].

1.13 Wettability in electrodeposition

The contact angle θ , as seen in Fig. 1.16, is the angle at which the liquid-vapor interface meets the solid-liquid interface. The contact angle is determined by the resultant between adhesive and cohesive forces. As the tendency of a drop to spread out over a flat, solid surface increases, the contact angle decreases. Thus, the contact angle provides an inverse measure of wettability [56]. Controlling the wettability of solid materials is a classical and key issue in surface engineering. Roughly speaking, two extreme limits are often desired. The first limit is complete wetting, in which a liquid brought

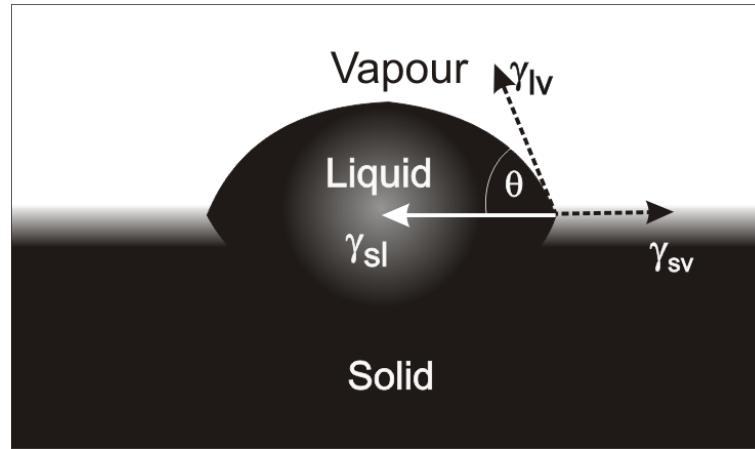


Figure 1.16: A droplet of liquid on a solid surface showing contact angle and how it can be calculated

into contact with a solid spontaneously makes a film. The second limit is complete drying: Liquid drops remain spherical without developing any contact with the substrate. They are thus readily evacuated, which prevents liquid contamination of the solid surface.

Figure 1.16 shows wetting of liquid on an ideal solid surface.

The wetting of a solid with liquid, with air or vapor as surrounding medium, is dependant on the relation between interfacial tensions, γ , liquid/vapor γ_{lv} , solid/vapor γ_{sv} and solid/liquid γ_{sl} . Interfacial energy is an energy that tends to minimize surface area of liquid drop in a particular atmosphere. In absence of other forces, surface tension of liquid will draw it into a sphere, which has smallest surface area. The ratio between these surface tensions determines the θ of a liquid droplet on a given surface and it is described by Young's equation:

$$\gamma_{sv} = \gamma_{ls} + \gamma_{lv} \cos \theta \quad (1.32)$$

A contact angle less than 90° (low contact angle) usually indicates that wetting of the surface is very favorable, and the fluid will spread over a large area of the surface. For the contact angles greater than 90° (high contact angle) wetting of the surface is unfavorable so the fluid will minimize contact with the surface and form a compact liquid droplet. For water, a wettable surface may also be termed hydrophilic and a non-wettable surface hydrophobic. Superhydrophobic surfaces have contact angles greater than

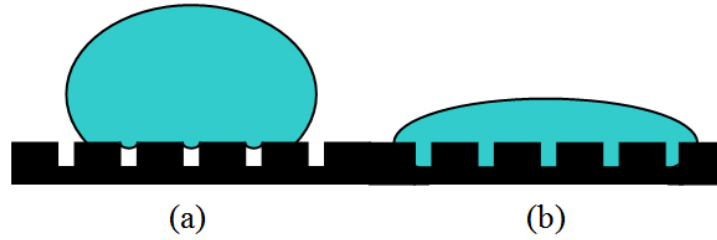


Figure 1.17: Schematic diagrams showing (a) Cassie-Baxter and (b) Wenzel wetting regimes.

150°, showing almost no contact between the liquid drop and the surface. This is sometimes referred to as the “Lotus effect” [57].

1.13.1 An influence of the surface roughness of a substrate on wetting

The study of wettability has been a major focal point for many researchers and has been applied to a wide range of applications such as biomedical, coating technologies and adhesion. As the interface between a solid and liquid can be very complex it is necessary to account for the wetting regime that takes place. Two of the most common wetting regimes is that of Wenzel and Cassie-Baxter which are explained in Fig. 1.17.

Surface roughness of a surface, defined as the deviation of actual surface from an ideal, atomically smooth and planar surface, is considered to be an important factor effecting spreading. Extensive research studies have been done and various theories were proposed in this area. Majority of works concentrated on the influence of roughness on contact angle. The roughness of the surface affects its wettability and depending how this is affected, two different models can be described. When a drop is placed onto a rough surface, it can fill the grooves or stay on the surface causing the formation of the “air-pockets”. In the first case, the Wenzel model is applied and in the second the Cassie-Baxter model is more appropriate.

The theoretical model developed by Wenzel, is one of the first models to include the influence of roughness on wetting. According to the model, additional area produced due to surface roughening was effective in raising surface energy, and resulting in good wetting. The model thus predicts that

a surface that has good wetting characteristics when smooth will wet even better when rough. Thus, increase in surface roughness of the substrate will result in smaller contact angle. The model holds good for systems with equilibrium contact angle, $\theta < 90^\circ$, i.e. for hydrophilic systems. The behavior predicted by this model is expressed by the relation below.

$$\cos \theta_r = r \cos \theta_o \quad (1.33)$$

In Eq. (1.33), r is the roughness area ratio also known as Wenzel's roughness ratio, given by ratio of true surface area to projected surface area. θ_r and θ_o are the equilibrium contact angles over rough surface and smooth surface, respectively. This relation implies that if roughness ratio r is increased, the apparent contact angle θ_r will decrease.

On hydrophobic solids, the situation is different from that for hydrophilic solids. If the solid is rough enough, we do not expect that the liquid will conform to the solid surface, as assumed in the Wenzel model. Rather, air pockets should form below the liquid, provided that the energetic cost associated with all the corresponding liquid/vapor interfaces is smaller than the energy gained not to follow the solid. This model is known as Cassie-Baxter model [58].

Aim of the work

Since the landmark paper of Gleiter [1], there has been increasing interest in the synthesis, processing, characterization, properties, and potential applications of nanostructured materials. Accordingly, a number of techniques have been developed to produce nanoscale particles as well as bulk nanostructured materials. Nanostructured material with their unusual mechanical, electrical and optical properties endowed by confining the dimensions of such materials due to the combination of bulk and surface properties to overall behaviour are also interesting for investigation of their catalytic properties.

One of the great challenges in the twenty-first century is unquestionably energy storage. The performance of storage and conversion devices depends intimately on the properties of their materials (nanostructured materials for advanced energy conversion and energy storage). Nanostructured materials are becoming increasingly important for electrochemical energy storage [59].

The main goals of this work is:

- to electrochemically make powders of the Ni-Co-Fe system that can be periodically mechanically removed from the electrode
- to produce deposits with highly developed surface area
- to investigate the influence of different deposition parameters on formation of disperse deposited layers
- to characterize their atomic structure, microstructure and their stresses
- to study their electrochemical properties
- to synthesize porous and dendritic layers of two or more different materials on different electrode surfaces

Chapter 2

Experimental Procedures

2.1 Electrolytic fabrication techniques

The processes of metal electrodeposition can be categorized into three main groups:

- 1 electroplating and electroforming
- 2 electrorefining and electrowinning
- 3 metal powder production

each of which have different requirements with respect to the physical state of the cathodic product. In electroplating the crystal layer is typically required to be fine grained, smooth, strongly adhesive i.e. to be easily polished or bright. In refining and electrowinning relatively coarse grained, rough, but adhesive deposits are required. They have to be of high purity and firm enough to endure handling before melting and casting into shapes suitable for further processing. In metal powder production by electrodeposition a controlled product particle size is necessary and it is preferable if the product is only weakly adhesive. The first kind of deposit can be obtained from solutions characterised by low exchange current densities at overpotentials close to the end of the Tafel linearity in the presence of different organic additives, with different effects on the cathode deposit. The deposits in electrorefining and electrowinning are obtained from electrolytes characterised by medium exchange current density at overpotentials close to the end of Tafel linearity. Spongy and granular electrodeposits appear during deposition by processes characterised by large exchange current densities at low

overpotentials. They are not often met in electrodeposition practice. Spongy zinc can be formed during the charging cycle of some alkaline storage batteries, and can be easily removed by electrodisolution at a given discharging rate, as can the whiskers which can be formed in some plating baths in the presence of organic additives.

It has been reported to successfully produce powders of about 60 metals by electrolysis. The majority of the metals are obtained by molten-salt electrolysis and powders of about 20 metals can be electrodeposited from aqueous solutions. However, while a larger number of metals can be obtained in powder form by molten-salt electrolysis, a much larger quantity of powder is produced by electrolysis from aqueous solutions. This is because the most important powders (copper, iron, and nickel) are obtained from aqueous solutions.

Electrolysis takes place in an electrolytic cell. A two compartment three electrode electrolytic cell used for electrochemical characterization through experiments is shown in Fig. 2.1. When a direct electric current is passed through an electrolyte (such as a molten salt or an aqueous solution of a salt, acid or base), chemical reactions take place at the electrode contacts between the electrical circuit and the solution. The combination of container, electrodes and electrolyte constitute the electrolytic cell. In such a cell, electrical energy from the current supply (potentiostat/galvanostat) is converted to chemical energy (Fig. 2.2). Various reactions may take place at the electrodes during electrolysis. In general, reduction take place at the cathode, and oxidation takes place at the anode.

2.2 Production of nanostructured deposits

There are three main electrochemical methods for preparing metal particle dispersions exhibiting excellent size monodispersity. The first of these, **pulse plating**, involves the application of a train of negative going voltage pulses approximately 10 ms in duration separated by much longer (e.g., 1 s) rest periods at open circuit (scheme a in Fig. 2.3). The objective of pulsed electrodeposition is to reduce the average growth rate of particles which, as already indicated, is expected to reduce the interactions between them. To date, this pulsed electrodeposition strategy has been applied to the growth of cadmium nanoparticles [61]. In electrochemical **slow growth**, growing

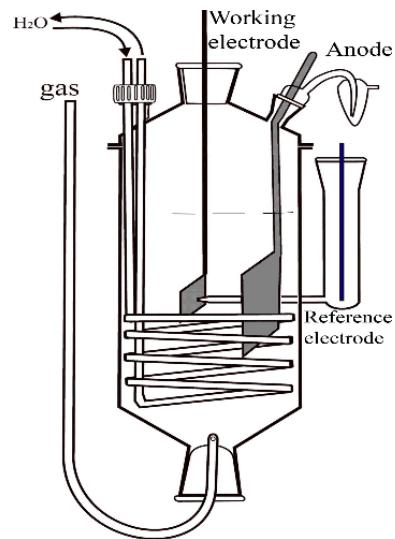


Figure 2.1: Schematic representation of the electrochemical cell.

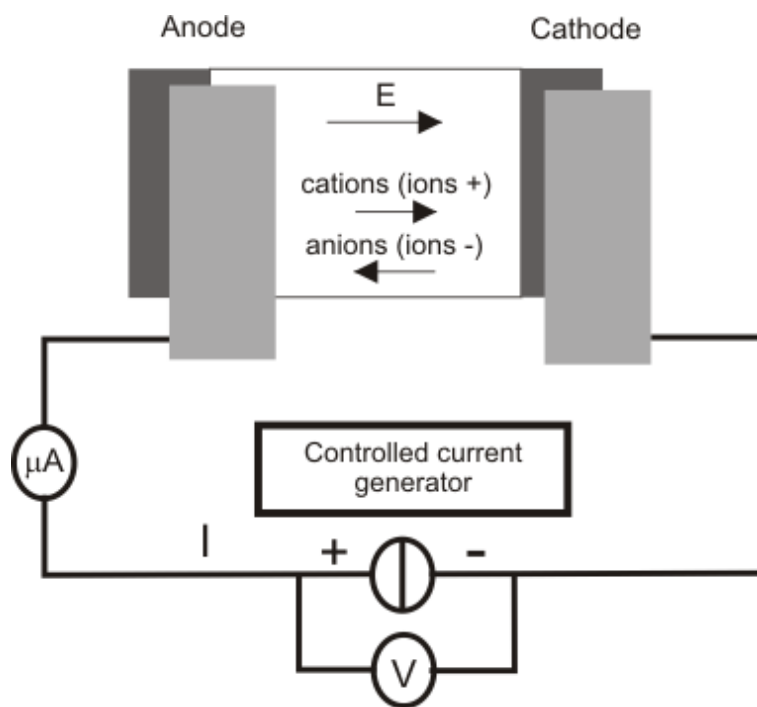


Figure 2.2: Schematic diagram for electrodeposition process [60].

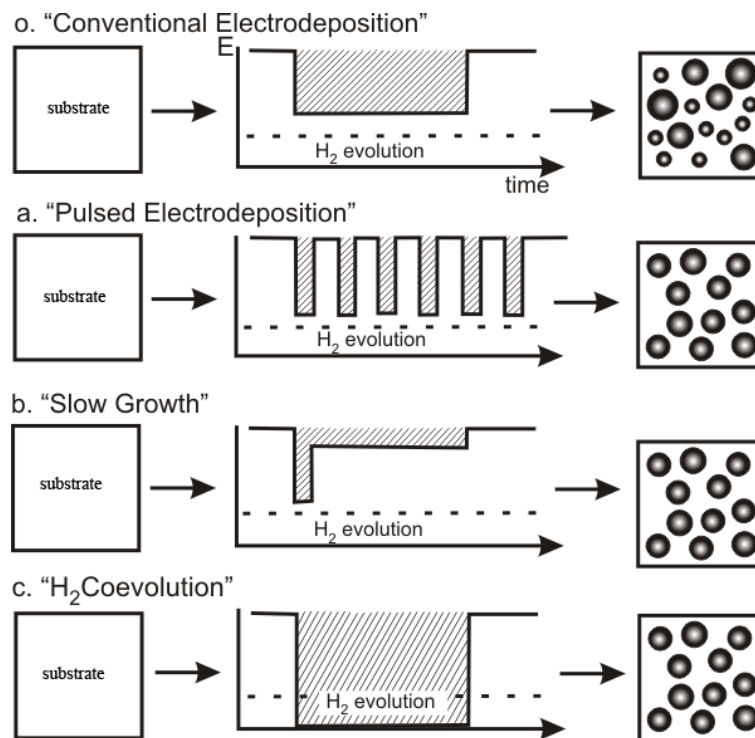


Figure 2.3: Three experimental methods for deposition of metal nano and micro particles dispersions exhibiting excellent size monodispersity [45].

nanoparticles at a reduced deposition overpotential (scheme b in Fig. 2.3) has much the same effect as applying multiple plating pulses. In practice, there are two beneficial effects of this strategy: A lower nucleation density is obtained, and the diffusive coupling between particles is reduced combine to produce metal nanoparticle dispersions exhibiting excellent particle size monodispersity.

- H_2 co-evolution method

A radically different approach involves the application of an extremely negative overpotential during metal plating shown (scheme c in Fig. 2.3). This potential must be so negative that it causes the decomposition of solvent to occur in parallel with the plating of metal onto the substrate surface. In the case of aqueous solutions, an applied potential of -1.5 to -2.0 V versus the normal hydrogen electrode is sufficient to cause the rapid reduction of protons at low pH or water at high pH to H_2 gas bubbles at the cathode [62]. This strategy was initially applied to the growth of nickel nano- and mi-

croparticles on graphite surfaces [63]. With increasingly negative deposition potential, the rate of H_2 evolution dramatically increases and this increased H_2 co-evolution rate is associated with a pronounced narrowing of the particle size distribution for nickel nanoparticles. Why does H_2 co-evolution work? Two factors combine to enable the preparation of size monodisperse nickel microparticles by this method. First, the generation of H_2 bubbles at the electrode surface stirs the plating solution in the immediate vicinity of the growing nickel particles (these particles actually catalyze the proton reduction reaction). This stirring has the potential to directly “erase” the depletion layer that develops at each growing nickel particle, thereby eliminating or reducing deleterious interparticle coupling.

2.3 Experimental setup

Electrochemical studies or experiments were conducted with a potentiostat/galvanostat system having a computer interface and three electrode electrochemical cell. Experiments were performed on polycrystalline Ti, polycrystalline Cu and single-crystalline Cu (111) substrates with different surface area exposed to the electrolyte. A platinum mesh rod and an Ag/AgCl electrode and saturated calomel electrode (SCE) served as counter and reference electrodes, respectively. Before each scan and subsequent experiment, electrodes were polished, washed and dried properly. Powdered and dendritic layers are obtained from the dilute solutions, but at current densities considerably larger than the limiting diffusion current density for the electrodeposition process.

2.3.1 Synthesis

Electrodeposition at high overpotentials is used as a route to fabricate dendritic layers. The deposition was commenced in galvanostatic mode under strong H_2 co-evolution. The operating parameters are variation in current density and varying Co^{2+} to Ni^{2+} ion concentration. The different bath was used for deposition of hierarchical dendritic structures of NiCoFe alloy. All experiments were conducted at room temperature.

2.3.2 Electrochemical characterization-Cyclic Voltammetry

The electrochemical phase formation is studied by cyclic voltammetry (CV). CV is characterized by smooth increase of a working electrode potential from one potential limit to an other and back. It follows that the potential limits and the potential sweep rate are the basic adjustable parameters. Also the properties of an electrolyte, mainly the concentration of electroactive species and temperature, could be affected. In this technique, the input potential signal is a potential of a stationary working electrode is scanned linearly by means of potentiostat and the resulting current is monitored. When the current is plotted versus the potential, a cyclic voltammogram curve is obtained (Fig. 2.4). Two different regions can be recognized in the resulting cyclic voltammogram; anodic (positive current values) and cathodic (negative current values) where the oxidation and reduction reactions take place, respectively. The peak current on this voltammogram shows the potential where the electrode reactions take place. The potential, shape, and the height of the peak current are functions of scan rate, electrode materials, and solution composition. The reversibility of an electrochemical reaction will depend on the rate of electron transfer at the electrode. If the rate of electron transfer is fast with respect to the timescale of the CV experiment, then the reaction is reversible.

2.4 Current efficiency

Besides the weight measurements, the efficiency of the overall electrodeposition process for comparison was determined by the measurement of evolved hydrogen on the cathode. The current for hydrogen evolution was obtained using equation for Faraday's law (the quantity of a substance produced by electrolysis is proportional to the quantity of electricity passed) applied to the process of gas evolution:

$$I_{H_2} = \frac{nFV_o}{rV_n} \quad (2.1)$$

where V_o is the experimentally determined volume of the evolved hydrogen at P_{at} and $T = 298\text{ K}$, t the time of hydrogen evolution under constant current, V_n the volume of 1 mol of hydrogen at normal conditions ($22.4\text{ dm}^3\text{ mol}^{-1}$), n the number of exchanged electrons and F is the Faraday's

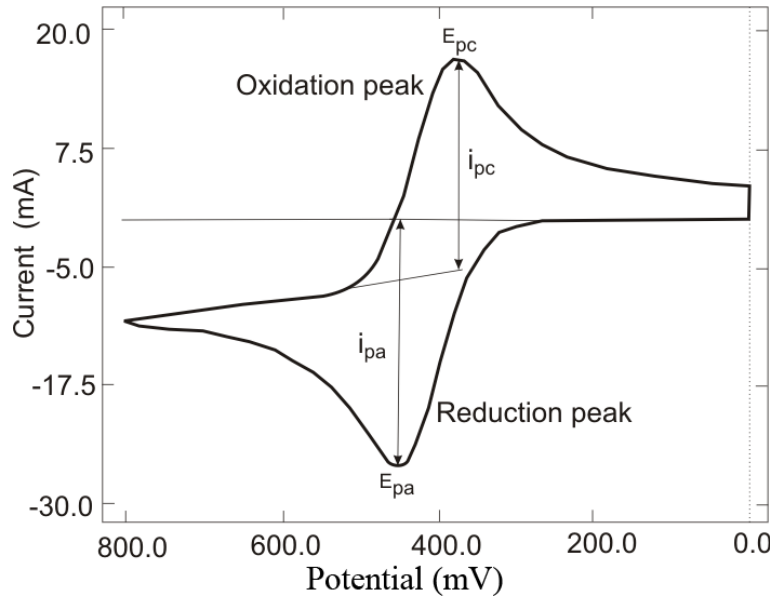


Figure 2.4: A typical cyclic voltammogram showing reduction and oxidation current peaks.

constant. The gas was collected in a purpose-built glass burette.

Current efficiency for the electrodeposition process was obtained from the relation:

$$\nu(\%) = \frac{j_{deposit}}{j_{tot}} \times 100 = \frac{j_{tot} - j_{H_2}}{j_{tot}} \times 100 \quad (2.2)$$

2.5 Characterization techniques

Several techniques have been used to characterize the electrodeposited dendritic layers. The X-ray diffraction, in the range of scanning angle 20-120° with CuK α radiation ($\lambda=1.5406 \text{ \AA}$) was done using a Philips X'Pert System, X-Ray Diffractometer.

2.5.1 Microscopy methods

A Philips scanning electron microscope (SEM) operating at acceleration voltages less than 30 kV, and a transmission electron microscope (TEM), CM 200 operating at 200 kV were employed to examine the morphology, particle size and microstructure of the dendritic layers. For the TEM study, bright-field, dark-field images and diffraction patterns were recorded. The

chemical composition/purity of the electrodeposits and layer was determined by energy dispersive spectroscopy (EDX) analysis.

In addition, SEM was used to characterize the surface topography of dendritic layers in more details. High resolution three dimensional (3D) data sets were obtained from the sample surface. 3D reconstruction from stereoscopic images (acquiring at varying specimen tilt angles) is based on the measurements of disparity, which is the shift in pixels of the specimen features from one image to another. The reconstruction of surfaces was done using two tilted images and it is affected by the tilt angle itself, the image resolution and the working distance.

Mechanical properties of the deposits were studied by microhardness measurements using a Vickers indenter mounted on a Olympus optical microscope.

2.5.2 X-Ray Diffraction

X-ray scattering techniques are a family of non-destructive analytical techniques which reveal information about the crystallographic structure, chemical composition, and physical properties of materials and thin films. X-ray diffraction peaks are broadened due to instrumental effects, small particle size, and lattice strain in the material. The crystallite size is determined by measuring the Bragg peak width at half the maximum intensity and putting its value in Scherrer's formula. The lattice strain in the powder particles can be determined by the dependance of the peak broadening on the diffraction angle.

2.5.3 Crystallite size

According to Scherrer it is possible to determine the average grain size of spherical crystallites by measuring the full width at half maximum- FWHM of the diffraction peaks corrected for the contributions from the diffractometer. The thickness of a crystallite consisting of p lattice planes of thickness d calculates to $L_{hkl} = p d$. The relation between L_{hkl} and the FWHM of the diffraction peak (hkl) can directly be derived from the Bragg equation. The final form used for calculation of crystallite size is:

$$\beta_{hkl} = \frac{0.89\lambda}{L_{hkl} \cos \theta} \quad (2.3)$$

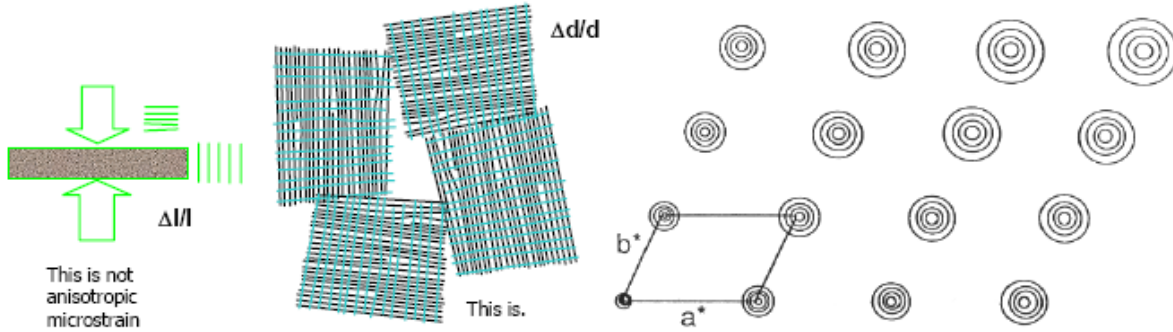


Figure 2.5: Left: Schematic drawing of the difference between strain induced by external forces and internal lattice strain due to the defects in the crystal structure. Right: Schematic drawing of a peak broadening in reciprocal space due to lattice strain [64].

With the average grain size L_{hkl} of a powder for grain sizes below $0.1 \mu\text{m}$ and the FWHM β_{hkl} in radians.

2.5.4 Lattice strain

Strain in a crystal lattice is a distribution of lattice parameters around an average value caused by defects, not by external force (Fig. 2.5). A sample with isotropic strain produces peak broadening in reciprocal space which is augmenting with increasing distance of the reflection from the origin (Fig. 2.5).

Each crystallite is considered to have its own set of lattice parameters which are different from the average values. This leads to a multidimensional distribution of lattice parameters over the entire powder sample.

2.5.5 Stress and texture

The intensity of a Bragg reflection for an ideal powder, where the crystallites uniformly occupy all orientations in space, only depends on the scattering angle 2θ but not on the rotation Φ or tilting Ψ of the sample (Fig. 2.6). In reality, the orientations of crystallites in polycrystalline material often produce anisotropic intensity distributions (textures) which can be visualized (pole figures) at constant 2θ by rotating Φ and tilting Ψ . Generally, the pole figures of at least 3 linear independent lattice planes (hkl) are required to quantitatively calculate the orientation distribution function (ODF) in

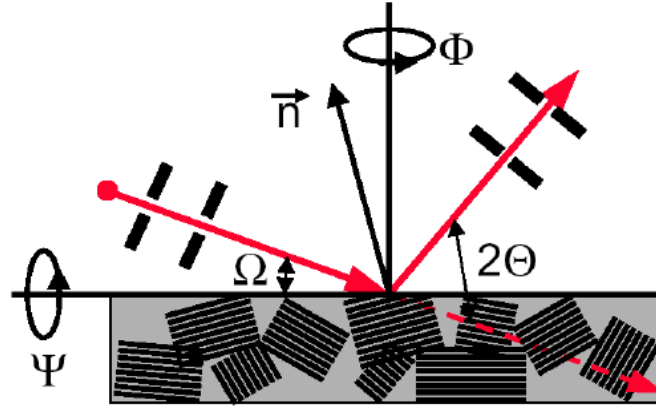


Figure 2.6: Schematic drawing of the orientation of crystallites in a polycrystalline sample. Ω denotes angle between incoming X-ray beam and the sample surface; 2θ the scattering angle; Φ the rotation of the sample; and Ψ the tilt angle of the sample. The orientation of the crystallite under investigation is described by its normal \vec{n} [64].

3-dimensional Euler space.

To perform texture and (macroscopic) stress measurements, the diffractometer must be equipped with an Eulerian cradle. The primary X-ray beam hits the sample and the reflected beam is then picked up via crossed soller slits so that the angular window within the pole figure is small enough in the plane of dispersion to enable good angular discrimination and is large enough in the vertical plane to collect as much intensity as possible. A typical setup is shown in Fig. 2.7.

X-ray powder diffraction is also powerful method to analyze macroscopic stress in all directions in space by exact measurements of the d-spacings of a Bragg reflection (hkl) in dependence of the inclination of the lattice plane ψ to the sample surface. In the case of a material under stress, the d-spacing is not independent of the orientation of the crystallites in the sample. When drawing the dilatation $\varepsilon = \Delta d/d$ in dependence of $\sin^2\psi$ the slope $\frac{\partial \varepsilon}{\partial \sin^2(\psi)}$ reveals the stress direction and in combination with the elastic constants the amount of mechanical stress. The method has been used to study thermally induced stress in metals.

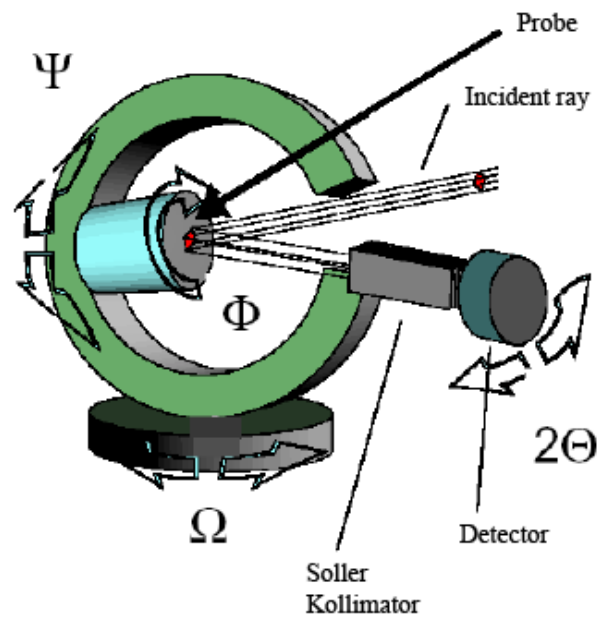


Figure 2.7: Diffractometer set up for texture and macroscopic stress measurements [64].

Chapter 3

Microstructure and mechanical properties of disperse Ni-Co alloys electrodeposited on Cu substrates ¹

3.1 Introduction

The recent interest in the electrodeposition of iron-group metals (Ni, Co and Fe) and their alloys is due to their unique magnetic and thermophysical properties [65, 66]. Electrodeposition is a process which is capable of depositing nanocrystalline metals and alloys [2] onto recessed and non-uniform surfaces, and therefore has found a role in microelectromechanical systems (MEMS) [66, 67, 68, 69, 70]. Both hardness and strength of the electrolytic deposits are better than that of alloys prepared by conventional metallurgical processes [66]. One of the most important aspects of the electrodeposition process is possibility for the production of nanocrystalline materials which exhibit unique properties compared to the microcrystalline counterparts [2].

A metal powder represents a loose deposit which can spontaneously fall off from the electrode or can be removed by tapping or by other similar ways [71, 72, 38]. Electrodeposition of the powders from the solutions, estab-

¹Based on the published article, L.D.Rafailovic, H.P.Karntaler, T.Trisovic, D.M.Minic, *Microstructure and mechanical properties of disperse Ni-Co alloys electrodeposited on Cu substrates*, Mater. Chem. Phys, 120 (2010) 409-416.

lished by the work of Calusaru [73] possesses significant advantages over other methods for synthesis of nanocrystalline materials [2]. This method usually yields products of requested chemical composition and high purity, which can be well pressed and sintered [74, 75, 76]. The effect of operating conditions, electrolyte composition, temperature and pH on the Ni-Co composition and properties of obtained deposits are widely investigated [77, 78, 79, 80]. On the other hand, electrodeposition at very high current densities and overpotentials is only investigated in the form of powders [81, 82, 83].

However, electrochemical synthesis of disperse deposits on the substrate is insufficiently investigated [71]. Investigations of such Cu deposits formed at high current densities whereby open and very porous structures with extremely high surface areas are obtained were initiated recently [84]. It has been stated that the open and porous structures of copper deposits obtained at high current densities were ideally suited for the use as electrodes in electrochemical devices such as fuel cells, batteries and chemical sensors [84], while the extremely high surface area is relevant for evaluating some electrochemical reactions [85]. Surface microstructure plays a crucial role in application such as magnetic storage, printing devices and all other similar technological procedures, but correlation of the surface morphology and roughness structure with deposition parameters is still an open topic [86]. Three-dimensional (3D) characterization seems more adapted for applied research. Therefore, the aim of this study is the investigation of the influence of the deposition current density on the microstructure of disperse Ni-Co deposits and the correlation between electrolysis conditions necessary for the formation of such rough deposits on substrates and their morphology, surface roughness and mechanical properties.

3.2 Experimental Procedure

The deposits were obtained in an open glass electrochemical cell with a volume of 1 dm³, thermostatically controlled at a temperature of 298 K. A Ti-plate covered with RuO₂, TiO₂ (10 cm² geometric area), placed close and parallel to the Cu plate, was used as an anode (DSA). The solutions were made from analytical grade chemicals and triple distilled water. The alloys were electrodeposited from mixed ammonium sulfate-chloride solutions of different Ni²⁺/Co²⁺ ions concentration ratios of 0.25, 0.5, 1, 2 and 4 in 0.12

mol dm⁻³ (NiSO₄+CoSO₄) using 0.5 mol dm⁻³ NH₄Cl and 3.5 mol dm⁻³ NH₄OH as a buffering agent and a supporting electrolyte at pH=10. The electrodeposition was performed with a constant current regime ranging from 65 to 400 mA cm⁻². The deposition time was adjusted to the same quantity of electricity passed.

Polarization diagrams were recorded with the three compartment standard electrochemical cell at a temperature of 298 K. The platinum foil counter electrode and the reference-saturated calomel electrode (SCE) were placed at separate compartments, connected to the working electrode by a Luggin capillary positioned at a distance of 0.2 cm from the working electrode surface. The working electrode was a copper electrode rod (d = 0.4 cm). Before each experiment the working electrode surface was polished using 0.05 μm alumina impregnated polishing cloths. The Ni-Co alloys were electrodeposited with the same amount of charge passed (43 mA h cm⁻²).

Polarization measurements were performed by a computer controlled electrochemical system (PAR M 273A) using the corrosion software (PAR M352/252, version 2.01) with a sweep rate of 1 mVs⁻¹. To obtain polarization curves corrected for the IR drop, current interrupt technique was used with the time of current interruption being 0.5 s. The current efficiency of alloy deposits was determined at different current densities by measuring the mass of the deposit on the copper cathode which was used as a working electrode.

Surface morphology was examined using an XL 30 ESEM-FEG (environmental scanning electron microscope with field emission gun, FEI Company, NL). The 3D reconstruction of the specimen surface was characterized by SEM using MeX software from Alicona (A). It enables to carry out a 3D analysis directly from the digital images yielding profile and roughness measurements and also area analysis as well as volumetric measurements. An alloy composition analysis was performed by ESEM using the energy dispersive X-ray spectrometry (EDX) software Genesis (USA). X-ray powder diffraction (XRD) analysis was carried out using a MPD diffractometer (Philips, NL) with CuKα radiation (40 kV/30 mA). Step scan mode was utilized with 0.03° in 2θ per 1.15 s step.

The micro-hardness of the deposits was determined using a Vickers micro-hardness indenter with a load of 50 μN. Cross-sections of the Ni-Co samples deposited on the Cu substrates were prepared for indentation measurements.

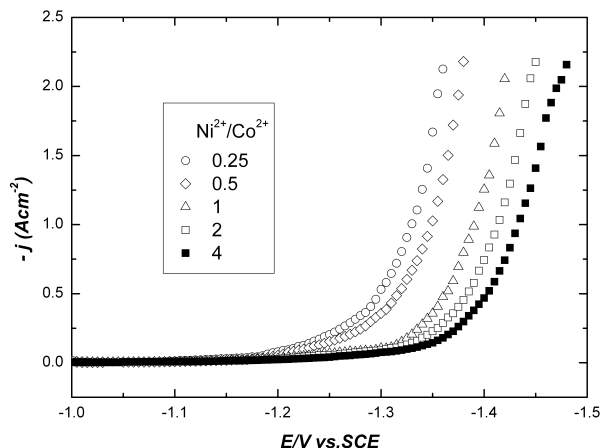


Figure 3.1: Polarization curves for the cathodic process of NiCo deposition on copper cathode for different composition of the electrolyte: \circ - $\text{Ni}^{2+}/\text{Co}^{2+}=0.25$; \diamond - $\text{Ni}^{2+}/\text{Co}^{2+}=0.5$; \triangle - $\text{Ni}^{2+}/\text{Co}^{2+}=1$, \square - $\text{Ni}^{2+}/\text{Co}^{2+}=2$ and \blacksquare - $\text{Ni}^{2+}/\text{Co}^{2+}=4$, corrected for IR drop. Scan rate 1 mV s^{-1} .

The final value quoted for the hardness of the deposits was the average of 10 measurements. Optical micrographs of the sample cross- sections were obtained by the optical microscope Olympus SZX 12 (JP).

3.3 Results and discussion

3.3.1 Current efficiency

Figure 3.1 shows the polarization curves for different compositions of the electrolyte performed on a Cu cathode. The shape and position of the polarization curves strongly depend on the electrolyte composition. A decrease in the content of Co^{2+} as well as an increase in the content of Ni^{2+} shifts the position of the corresponding polarization curves towards negative values of the potentials corresponding to the potential of the Ni/Ni^{2+} deposition of pure nickel.

Metal and alloy deposition of the iron group from aqueous solutions is accompanied by a concurrent hydrogen evolution reaction [87] which significantly affects the shape of the polarization curve and the morphology of the obtained deposits. According to the polarization diagrams, corrected

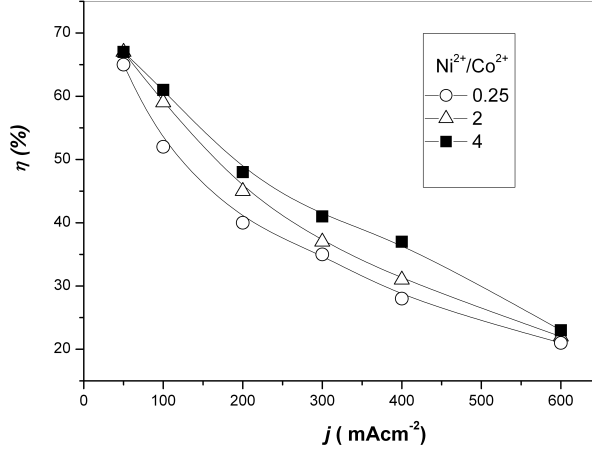


Figure 3.2: Current efficiency of the Ni-Co deposition process for the different current densities and compositions of the electrolyte: \circ - $\text{Ni}^{2+}/\text{Co}^{2+}=0.25$; \triangle - $\text{Ni}^{2+}/\text{Co}^{2+}=1$ and \blacksquare - $\text{Ni}^{2+}/\text{Co}^{2+}=4$.

for IR drop (which is indispensable because the galvanostatic deposition for production of disperse deposits is performed at high current densities using small ion metal concentration), the Ni-Co electrodeposition at overpotentials higher than -1.2 V is characterized by a sharp increase of the current density where disperse deposits with highly developed structures are formed. Formation of the disperse deposits is dependant on hydrogen evolution since at a current density higher than 200 mA cm^{-2} , the current efficiency is less than 50% (Fig. 3.2) for all investigated electrolyte compositions. Hydrogen provides some additional stirring effect and enhances formation of disperse deposits with more developed structures.

The hydrogen evolution during the deposition of the alloys diminishes the current efficiency, depending on the electrolyte composition as well as on the current density. These results are in agreement with polarization measurements where alloys with less nickel content have lower hydrogen overpotential and consequently a lower current efficiency. In the current density range, where the disperse deposits were obtained, the current efficiency decreases with the increase of the current density and with the decrease of the Ni^{2+} concentration in the electrolyte.

3.3.2 Composition of the Ni-Co alloys

In order to determine the influence of the electrolyte concentration on the composition of the obtained disperse Ni-Co deposits, electrodeposition at a current density of 65 mA cm^{-2} was performed. The chemical composition of the alloys deposited galvanostatically was determined for alloy samples as an average of 3 measurements with surfaces of $10 \text{ }\mu\text{m}^2$ with an error of $\pm 2\%$. Afterwards, current densities of 220 and 400 mA cm^{-2} were selected to determine the effect of the current density on the deposit composition for a chosen electrolyte composition.

According to the EDX analysis, the electrolyte composition ($\text{Ni}^{2+}/\text{Co}^{2+}$ - ion ratio) as well as the current density, affects the composition of the electrodeposited alloys remarkably (Fig. 3.3 and 3.4). However, the percentage of Ni in the deposit, especially for the deposit obtained from the electrolyte with $\text{Ni}^{2+}/\text{Co}^{2+} = 0.25$ was lower than in the electrolyte solution (Fig. 3.3). This indicates that the electrochemical alloying leads to an increase in the reaction rate of Co at relatively low current density of $j = 65 \text{ mA cm}^{-2}$ resulting in the higher content of Co in the alloy than in the electrolyte. Such behavior is in accordance with the term “anomalous codeposition” as introduced by Brenner [87] which refers to the preferential deposition of the less noble metal, i.e. Co. Besides, with the increase of the Ni^{2+} concentration in the electrolyte, the Ni content in the alloys almost reaches its content in the electrolyte.

The difference between the electrolyte composition and the deposit composition (Fig. 3.4) is much less pronounced at high current density, i.e. $j = 400 \text{ mA cm}^{-2}$. The composition of the obtained deposit is almost similar to the concentration of the metal ions in the electrolyte. In this case, the composition of the deposits is dependent on the current density, indicating that an increase of the current density is accompanied by a decrease of the Co content in the deposit. An increase of the current density leads to an increase of the overpotential which is accompanied by an increase of the activation of the electrode reaction. This results in an increase of the Ni content in the deposits.

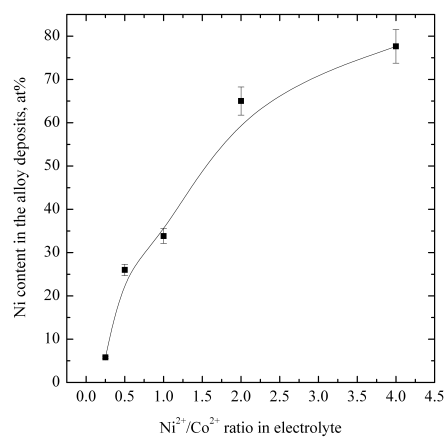


Figure 3.3: Dependence of the alloy composition on the $\text{Ni}^{2+}/\text{Co}^{2+}$ ratio in the electrolyte at a current density of 65 mA cm^{-2} .

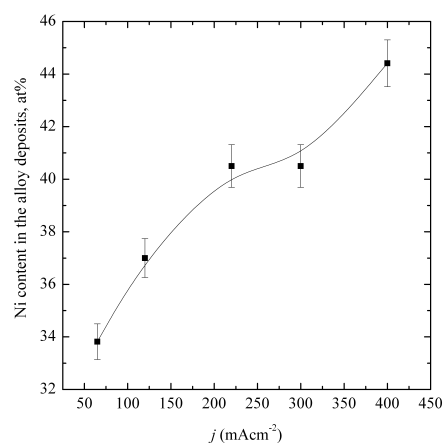


Figure 3.4: Dependence of the alloy composition on current density from an electrolyte with concentration ratio $\text{Ni}^{2+}/\text{Co}^{2+}=1$.

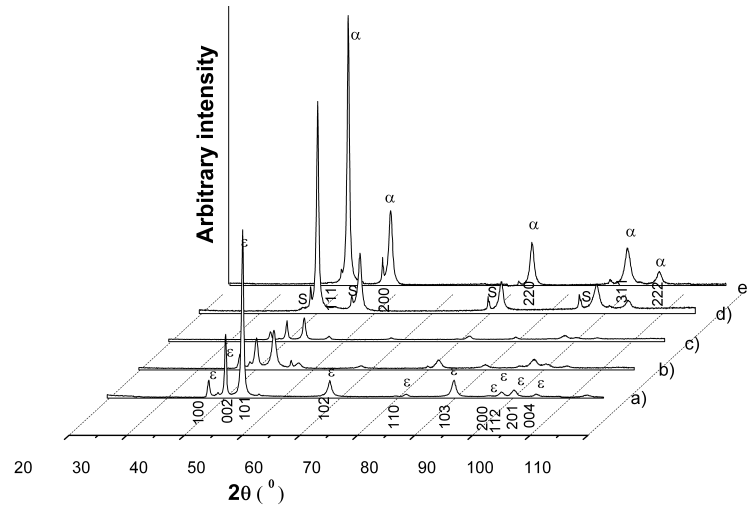


Figure 3.5: X-ray diffraction patterns of alloys deposited from the electrolyte with different $\text{Ni}^{2+}/\text{Co}^{2+}$ concentration ratio: a) 0.25, b) 0.5, c) 1, d) 2 and e) 4 at a current density of 65 mA cm^{-2} (α - reflections attributed to the α -Ni; ε - reflections attributed to the ε -Co; S-reflections attributed to the Cu substrate).

3.3.3 Microstructure of deposits

Influence of chemical composition of the electrolyte on the microstructure

Figure 3.5 shows a series of XRD patterns for all five alloys electrodeposited from different bath compositions at a selected current density of $j = 65 \text{ mA cm}^{-2}$ with same quantity of electricity and with an average sample thickness of $(25 \pm 5) \mu\text{m}$.

The X-ray analysis of the deposits shows the presence of solid solutions of Ni and Co with a structure which changes progressively with the change of their chemical composition depending on the used electrolyte. For the lowest content of Ni, a single phase deposit involves the hexagonal close-packed (HCP) phase also known as ε -phase (Fig. 3.5a). With the increase of the nickel content in the deposit ranging to 30-40 at%, the mixture of face centered cubic (FCC) also known as α -phase and the HCP phase was found (Fig. 3.5b-d). With the further increase of Ni content in the Ni deposit, only a single FCC phase is observed (Fig. 3.5e). The noticed diffraction peaks of Cu with low intensity belong to the substrate material. Deposits

rich in Co and deposits rich in Ni (Fig. 3.5 a and 3.5e) exhibit cell volumes comparable to the theoretical values of Co (22.1 \AA^3) and Ni (43.8 \AA^3), cf. Table 3.1. The morphology of all Ni-Co deposits strongly depended on the chemical composition of the alloy deposit i.e. the chemical composition of the electrolyte, Fig. 3.6. For the chosen current density of 65 mA cm^{-2} particles with a size varying from 5 to about $50 \text{ }\mu\text{m}$ composed of fine nanosized crystallites of different morphology were obtained. The morphology of the alloy deposited from electrolyte with the highest concentration of Co^{2+} ions in the electrolyte, at current density of a 65 mA cm^{-2} is shown in Fig. 3.6a. The deposit possesses the platelet structure.

Ni ²⁺ /Co ²⁺ current density	Crystal structure/concentration (%)	Grain size (nm)	a (Å)	c (Å)	Cell volume (Å ³)
0.25/ 65 mA cm ⁻²	HCP/100	20	2.506	4.069	22.126
0.5/ 65 mA cm ⁻²	FCC/27 HCP/73	11/9	3.533/2.505	4.076	44.114/22.153
1/ 65 mA cm ⁻²	FCC/28 HCP/72	19/15	3.529/2.505	4.072	43.955/22.127
1/ 220 mA cm ⁻²	FCC/71 HCP/20 amorphous phase/9	13/11	3.530/2.499	4.077	43.971/22.043
1/ 400 mA cm ⁻²	FCC/82 HCP/3 amorphous phase/15	11/10	3.533/2.495	4.100	44.096/22.100
2/ 65 mA cm ⁻²	FCC/87 HCP/13	14/5	3.528/2.480	4.057	43.901/21.610
4/ 65 mA cm ⁻²	FCC/100	13	3.526		43.833

Table 3.1: Phase composition, grain size and cell parameters of the Ni-Co alloys electrodeposited from the electrolyte with a different Ni²⁺/Co²⁺ concentration ratios.

For the concentration ratio $\text{Ni}^{2+}/\text{Co}^{2+} = 1$ in the electrolyte, the morphology of the deposit is slightly changed and consists of cauliflower particles exhibiting a surface morphology based on preferred oriented platelets (Fig. 3.6c). Figure 3.6b and 3.6d show enhanced dendritic growth with more disperse deposits obtained from the baths with the concentration ratio $\text{Ni}^{2+}/\text{Co}^{2+} = 0.5$ and 2, respectively. At one and the same current density of 65 mA cm^{-2} , more developed structures are formed leading an increase of the mean surface roughness. Finally, the particles deposited from the electrolyte with the highest content of Ni show cauliflower structure, Fig. 3.6e. The morphology of the deposits is similar to the morphology of the pure Ni obtained from the Watt's bath without addition of a surfactant substance [71, 82].

The SEM micrographs show that the surface morphology of the deposit is determined by the nature of the electrochemically active ions or complexes and the kinetics of the electrocrystallization process.

3.3.4 Phase analysis of deposits- Influence of current density on microstructure

A detailed Rietveld's analysis revealed that the phase composition of the deposited Ni-Co solid solutions depend on the composition of the electrolyte bath as well as on the applied current density (Fig. 3.7). Rietveld's refinement procedure [88] is able to simulate the XRD pattern from given starting parameters. The purpose of this simulation is therefore to refine individual parameters, e.g. phase content, grain size, and crystal lattice parameters, to obtain a good fit. For this purpose Rietveld's refinement program TOPAS V3.0 (Bruker AXS GmbH, Germany) was used [89]. The quality of the refinement progress was controlled by monitoring the fit parameter R_{wp} , the goodness of fit (GOF), and the Durbin-Watson factor.

Deposits obtained from an electrolyte with a equal ion metal concentration ratio, $\text{Ni}^{2+}/\text{Co}^{2+}=1$, have shown the formation of a mixture of both phases, HCP and FCC. The formation of solid solutions is a consequence of the mutual miscibility of Ni and Co in the range of concentration in the obtained deposits (Table 3.1) which is in accordance to the phase diagram [90]. The decrease of the current density results in pronounced crystallization and an increase of the size of crystallites as well as a higher HCP content in the alloys. Evolution of the FCC phase content from the same bath was achieved

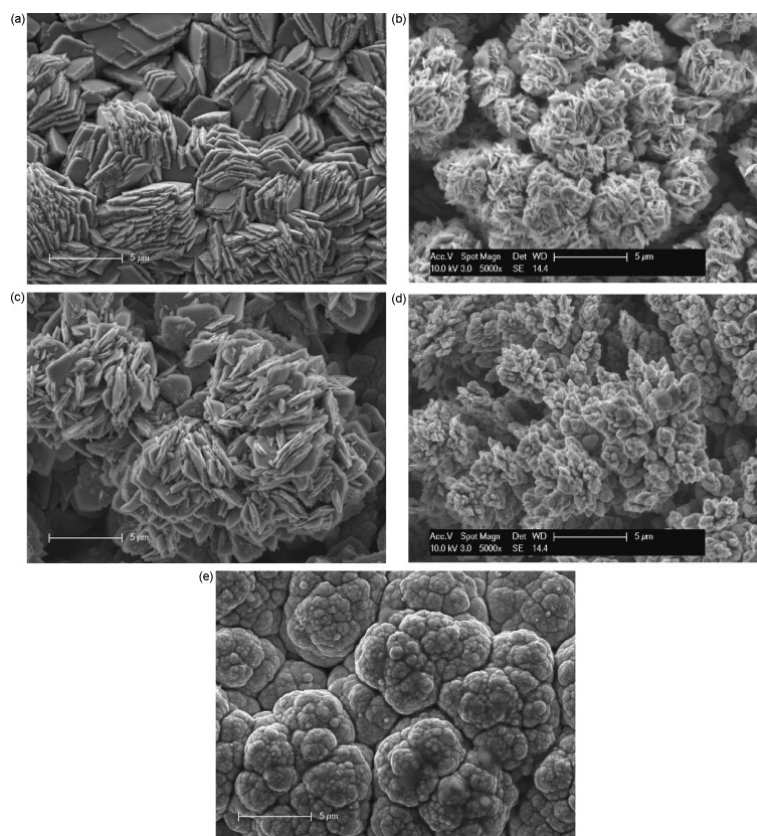


Figure 3.6: SEM micrographs of Ni-Co deposits obtained at a current density of 65 mA cm^{-2} from an electrolyte with different $\text{Ni}^{2+}/\text{Co}^{2+}$ concentration ratio: a) 0.25, b) 0.5, c) 1, d) 2 and e) 4.

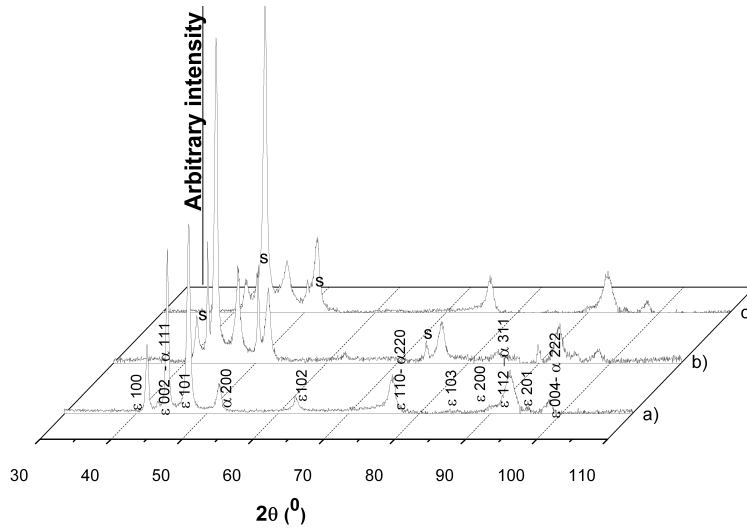


Figure 3.7: X-ray diffraction patterns of alloys deposited from an electrolyte with concentration ratio $\text{Ni}^{2+}/\text{Co}^{2+}=1$ at different current densities: a) 65 mA cm^{-2} , b) 220 mA cm^{-2} and c) 400 mA cm^{-2} (α -reflections attributed to the α -Ni; ε -reflections attributed to the ε -Co; S-reflections attributed to the Cu-substrate).

by the increase of the current density (Fig. 3.8).

If the kinetics of the deposition process is fast, a disperse deposit can be obtained at low driving force, while a much larger driving force is needed for kinetically slow processes such as Ni and Co deposition [71] resulting in an electrodeposition process far from equilibrium conditions, i.e., at high overpotentials, and in the formation of the FCC phase. At low overpotentials, a higher amount of Co in the HCP phase is formed.

3.3.5 Grain size of Ni-Co alloy deposits

The electrolyte composition and the current density have a great effect on the grain size of the deposits. Average grain sizes were calculated from the peak broadening from XRD according to the Scherrer equation with the Rietveld refinement method [88]. Obtained alloy deposits were composed of fine nanosized crystallites (cf. Table 3.1).

The alloy electrodeposited at a selected current density of 65 mA cm^{-2} from the electrolyte with the ratio $\text{Ni}^{2+}/\text{Co}^{2+} = 0.25$ (Fig. 3.5a) contains the ε -Co phase with the hexagonal close-packed lattice and with an average grain

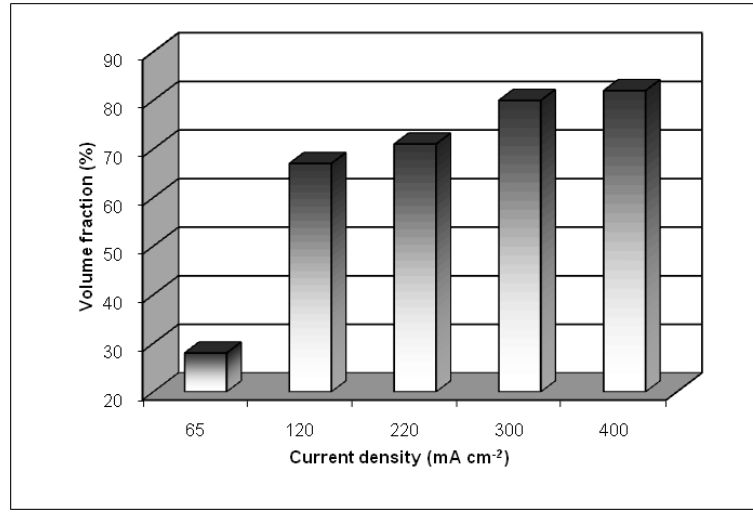


Figure 3.8: Evolution of the FCC phase content in deposits as a function of current density from an electrolyte with a concentration ratio $\text{Ni}^{2+}/\text{Co}^{2+}=1$.

size of 20 ± 2 nm. The average grain size in the deposits consisting single FCC phase was 13 ± 2 nm (Fig. 3.5e). In general, deposits with finer grain sizes are obtained with increasing Ni^{2+} concentrations in the electrolyte. With increasing Co content in the alloys (Table 3.1) the average size of crystallites increases ranging from 13 to 19 nm for the FCC phase and from 15 to 20 nm for the HCP phase. The mixture of two phases leads to a further grain size refinement of the deposits.

A reduction of the grain size was also achieved by an increase of the current density. Increasing the current density leads to the increase of the overpotential, and therefore increases the nucleus formation probability resulting in smaller critical radii and the number of atoms constituting the nucleus. Hence, the increase of current density decreases the grain size of the Ni-Co deposits (Table 3.1). The formation of electrochemical deposits from electrolytes with a higher $\text{Ni}^{2+}/\text{Co}^{2+}$ ratio is accompanied by higher overpotential values, therefore a deposit with finer grains is formed from a bath containing a higher Ni^{2+} ions concentration (Table 3.1). For the deposition of more disperse deposits consisting of fine nanosized crystallites, the use of overpotentials higher than 1.3V is requested, specifically in the case of the deposits obtained from an electrolyte with a concentration ratio $\text{Ni}^{2+}/\text{Co}^{2+} > 0.5$.

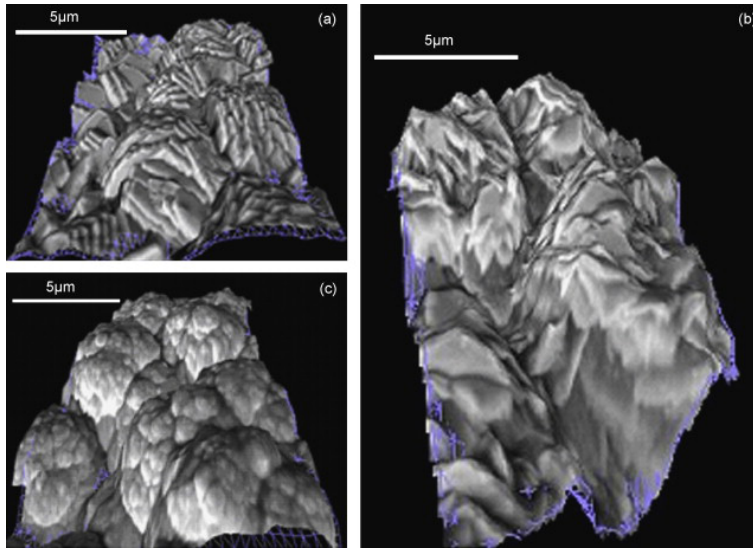


Figure 3.9: 3D SEM reconstruction of the surfaces of Ni-Co deposits obtained at a current density 65 mA cm^{-2} from the electrolyte with different $\text{Ni}^{2+}/\text{Co}^{2+}$ concentration ratios: a) 0.25; b) 1 and c) 4.

3.3.6 Surface roughness of Ni-Co alloy deposits

The 3D dataset was calculated from two stereoscopic images obtained by tilting the sample stage in the ESEM at the eucentric point with an angle of 5° (Fig. 3.9)a-c. The calculated roughness parameters are shown in Table 3.2.

The concentration ratios $\text{Ni}^{2+}/\text{Co}^{2+} = 0.25$ and 4 corresponding to single-phase systems, led to a surface with similar mean roughness values in spite of different morphology, (Fig. 3.6a and 3.6e respectively). In the case of an ion concentration $\text{Ni}^{2+}/\text{Co}^{2+} = 1$, involving more than one phase, the Ra values are almost 3 times higher, and the active surface increases in comparison to the specimens with ratios of 0.25 and 4. An increase in the current density results in a decrease in the mean roughness (Table 3.2), since at higher current densities the amount of crystal nuclei on the surface is enhanced. The larger the nucleation rate, the more homogenous is the grain size distribution leading to the formation of smoother deposits (see also, Fig. 3.6a and 3.6e). 3D SEM reconstruction experimental results confirmed the beginning of the disperse deposits formation in galvanostatic deposition using a current density of $j \geq 65 \text{ mA cm}^{-2}$.

$\text{Ni}^{2+}/\text{Co}^{2+}$	Current densities (mA cm ⁻²)	Ra (μm)	Rz (μm)	RS (μm^2)
0.25	65	0.7	4.7	1.64
0.5	65	1.3	5.2	1.34
1	65	3.0	13.1	1.98
1	220	1.1	5.2	1.38
1	400	1.0	6.5	1.62
2	65	2.1	9.2	1.37
4	65	1.0	4.7	1.64

Table 3.2: Roughness parameters of alloys deposited from electrolytes of different $\text{Ni}^{2+}/\text{Co}^{2+}$ concentration ratio and at different current densities; Ra- mean roughness, Rz- the difference between the highest and the lowest point in picture of a given scan, RS- active surface, i.e. the ratio of the real surface including topography to a projected surface of the measurements in a square with dimensions of 23x15 μm .

3.3.7 Mechanical properties of Ni-Co deposits

Microindentation tests were performed to investigate the mechanical properties of the deposited samples. A load of 50 μN was applied on the cross-section of the samples (deposits on copper substrate). The low applied load is needed to make penetration depths small enough to avoid the influence of the substrate on the hardness measurements. The microindentation test demonstrated that nanocrystalline deposits with a higher Ni content have a higher hardness (Fig. 3.10). The hardness of the Ni-Co alloys deposited from the same bath composition but at different current densities show a reduction of the hardness, not as significant as in the case of the hardness measured on the samples prepared from the different bath compositions.

In contrast to data found in [91], the hardness is increased with an increase of the Ni content in the deposits. According to the optical micrographs of the cross-sections of the deposits obtained on the Cu substrate presented in Fig. 3.11, two possible reasons can cause such a behavior. One is the grain size and the second is porosity inside the deposit with high Co content (Fig. 3.11a). The release of hydrogen in the layer surrounding the electrode also affects the properties of the obtained deposits, causing the formation of craters in the deposit (Fig. 3.11c). The deposit obtained from the electrolyte with the highest concentration of Ni^{2+} is compact (Fig. 3.11c), while the deposits obtained at the same current density from the bath with the

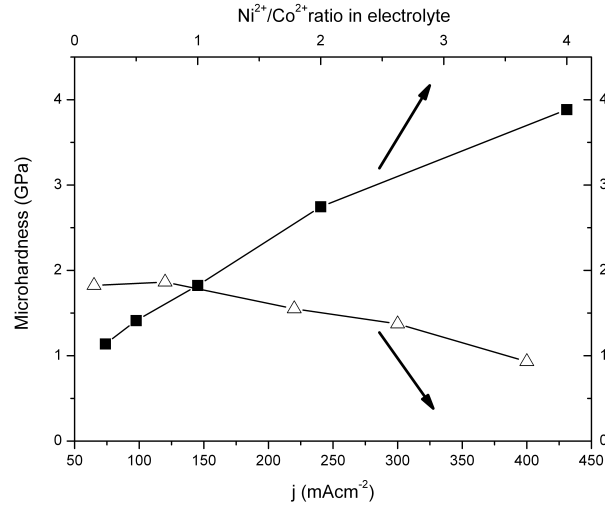


Figure 3.10: Hardness of Ni-Co deposits as a function of current density and electrolyte composition: Δ -concentration ratio $Ni^{2+}/Co^{2+}=1$ at different current densities, \blacksquare -different Ni^{2+}/Co^{2+} concentration ratios at a current density of 65 mA cm^{-2} .

concentration ratio $Ni^{2+}/Co^{2+}=1$ show a dendritic structure (Fig. 3.11b). It should be indicated that when the grain size is smaller than 10 nm, the grain refinement may cause softening of the nanocrystalline metals. In these measurements, differences in the grain size have not been so significant, but they still affect the large difference in the hardness value (Fig. 3.12).

The hardness measurements performed on the Ni-Co deposits obtained from an electrolyte with a concentration ratio $Ni^{2+}/Co^{2+} = 1$ at different current densities have shown a reduction of hardness. This can be attributed to the fact that at higher current densities a more disperse deposit with porous structure and very high surface area is formed. The hardness of deposits decreases with increasing current density since the evolution of the dendritic structure occurred during deposition at different current densities. The grain size is the main parameter influencing the grain boundary hardening. Based on the Hall-Petch relationship, nanocrystalline material is expected to exhibit a higher strength than its microcrystalline counterparts [92]. In the present study, the nanograin size did not affect the softening of the deposits formed from electrolytes with equal ion compositions, $Ni^{2+}/Co^{2+}=1$ at different current densities, considering grain sizes of the deposits were in the range of 10 nm. Although the more dendritic deposits produced at higher

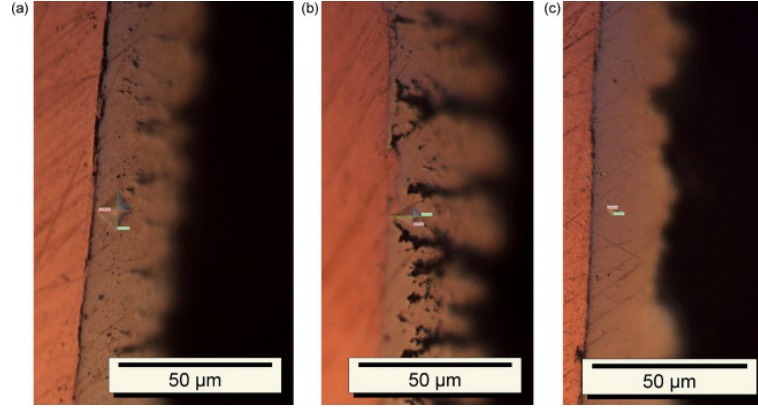


Figure 3.11: Cross-section of Ni-Co deposits obtained on a copper substrate from an electrolyte with concentration ratio $\text{Ni}^{2+}/\text{Co}^{2+}=1$: a) 0.25; b) 1 and c) 4 at a current density of 65 mA cm^{-2} .

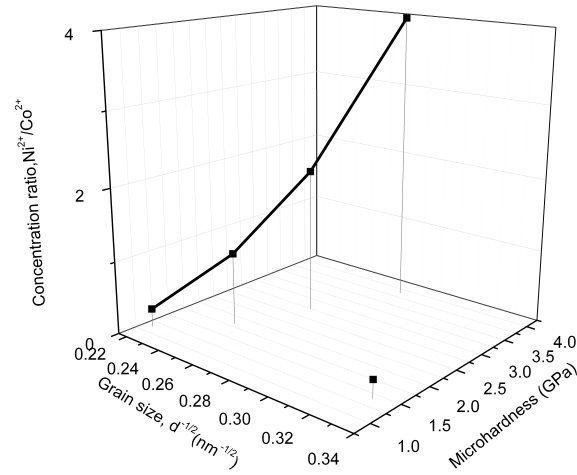


Figure 3.12: Effect of the grain size on hardness of Ni-Co deposits performed from an electrolyte with different $\text{Ni}^{2+}/\text{Co}^{2+}$ concentration ratios (d- average value of grains).

current densities, are characterized by a reduced grain size, the formation of the deposits with a very disperse dendritic structure has a decisive influence on the measurements.

3.4 Conclusions

The microstructure as well as the morphology of the Ni-Co alloy deposits electrochemically obtained from an ammonium sulfate-chloride solution depends on the deposition current density and the bath composition. The increase of the HCP phase content in the nanocrystalline deposits appears as a result of both an increase in the Co^{2+} ions concentration in the bath and a decrease of the deposition current density. The increase of the current density and the decrease of the Co^{2+} ions concentration in the bath results in finer grain deposits. Surface morphology and mean roughness of the deposits depend on the concentration ratio in the electrolyte; In the case of equal ions concentration of $\text{Ni}^{2+}/\text{Co}^{2+}$ in the electrolyte, the mean roughness of the deposit is highest. It is possible to achieve a variety of microstructural properties by choosing the current density or the electrolyte composition appropriately.

Chapter 4

Study of the dendritic growth of Ni-Co alloys electrodeposited on Cu substrates ¹

4.1 Introduction

Electrodeposition is one of the well-known approaches developed in recent years for the preparation of nanostructured pure metals and alloys [93, 2]. Ni-Co alloys have been widely investigated due to their unique magnetic and electrical properties which have found a potential application in different computer read/write heads and microelectromechanical systems (MEMS) [94, 69].

In general, electrolytic deposits can be compact or disperse [95, 72]. Disperse deposits are formed under electrolysis conditions which favor complete diffusion control of the process. Electrodeposition represents an excellent tool for the formation of metal disperse deposits with a highly developed surface area which can be successfully used as electrodes in electrochemical devices such as fuel cells, batteries and sensors [84]. The basic characteristics of these electrodes which should be fulfilled to be used for these purposes are:

¹Based on the published article, L.D.Rafailovic, D.M.Minic, H.P.Karnthaler, T.Trisovic, J.Wosik, G.E.Nauer, *Study of the dendritic growth of Ni-Co alloys electrodeposited on Cu substrates*, J. Electrochem. Soc., 157 (2010) 295-301.

the open porous structure which enables rapid transport of gas and liquid, and the extremely high surface area which is desirable for electrochemical reactions. According to this, in galvanostatic powder deposition, the initial deposition current density must be larger than the limiting diffusion current density [38]. Electrodeposition at overpotentials belonging to the plateau of the diffusion-limiting current density leads to the formation of dendritic deposits. The strong hydrogen codeposition leads to a stirring of the solution and changes the mass-transfer limitations at the electrode surface [85]. At the same time, the evolved hydrogen affects the mass and heat transfer, limiting current density and ohmic resistance leading to the formation of open porous deposit structures with a high surface area [85, 96, 97].

In this work, Ni-Co nanoscaled deposits were prepared and characterized using different techniques, with respect to elucidate the effect of current density and electrolyte composition on the formation of the dendritic deposits.

4.2 Experimental Procedure

The Ni, Co and Ni-Co nanostructured deposits were obtained in the galvanostatic regime at a current density range of 65 - 400 mA cm⁻². The electrolyses were performed from ammonium sulfate-chloride solutions for the concentration ratio Ni²⁺/Co²⁺=1 of a solution composition as follows: total concentration 0.12 M (NiSO₄+CoSO₄); 0.5 M NH₄Cl and 3.5 M NH₄OH at pH=10. Parent metal deposits were prepared from the same supporting electrolyte with total metal ion concentration of Co²⁺ or Ni²⁺ being 0.12 M. Reagents of analytical purity and deionized water were used for the bath preparation. The temperature of the bath during deposition was maintained at 298 K. The Ni, Co and Ni-Co deposits were prepared at constant current density with quantity of electricity passed of 0.043 Ah cm⁻² and an average sample thickness of (25±5) μm. Cu electrodes placed in the center of the cell with a 1.0 cm² surface area and 0.2 cm of thickness were used as working electrodes. A Ti plate covered with RuO₂, TiO₂ (10 cm² geometric area), placed close and parallel to the Cu plate, was used as anode (dimensionally stable anode- DSA).

The polarization measurements were carried out by a computer controlled electrochemical system (PAR M 273A, software PAR M352/252, version 2.01) with a sweep rate of 1 mV s⁻¹. For the correction of the IR drop,

the current interrupt technique was used with a time of current interruption of 0.5 s. The polarization curves were measured in a three-electrode electrochemical cell at (298 ± 1) K where the DSA was replaced by a large-area platinum mesh. The Luggin capillary connecting the reference electrode (saturated calomel electrode - SCE) to the electrolyte was positioned at a distance of 0.2 cm from the working electrode (copper rod embedded in resin, $d = 4$ mm). Before each experiment, the working electrode was highly polished with an alumina paste ($0.05 \mu\text{m}$) impregnated polishing cloth.

The average current efficiency for the hydrogen evolution reaction is determined by the measurement of the quantity of evolved hydrogen based on Faraday's law. The total electrodeposition current was calculated as a function of the electrodeposition time. The thickness of the deposits was estimated based on their cross-section images. The surface morphology was analyzed by XL 30 ESEM-FEG (environmental scanning electron microscope with field emission gun, FEI Company, Netherlands). The profile and roughness measurements, as well as 3D area analysis directly from the stereoscopic images of the specimen surface were carried out using MeX software from Alicona (A). The cross-section alloy composition analyses of the deposited samples embedded in the resin were performed by ESEM using the EDX technique (Genesis, USA).

X-ray powder diffraction (XRD) analysis was carried out using a MPD diffractometer (Philips, NL) with $\text{CuK}\alpha$ radiation (40 kV/30 mA) in Bragg/-Brentano geometry. Step scan mode was utilized with 0.03° in 2θ per 1.15 s step. The angular 2θ range investigated was 20° - 110° .

4.3 Results and discussion

4.3.1 Cathode polarization and efficiency

During the cathodic electrodeposition of iron group metals from aqueous solutions, competitive cathodic hydrogen evolution reaction occurs [29]. Since the formation of disperse and powder deposits is enhanced by a small metal ion concentration and a high deposition current density, polarization curves were measured with a correction for the IR drop. In this case, the plateau corresponding to the limiting current density cannot be established as in the case of electrodeposition performed from aqueous solutions containing an electropositive metal such as Cu due to the intensive hydrogen evolution

reaction almost from the beginning of the deposition. At the end of this plateau and at larger overpotentials, the intensive hydrogen evolution takes place. Therefore, polarization curves for electrodeposition of Ni, Ni-Co and Co are complex with the appearance of the limiting current density in a wide range of potential (Fig. 4.1a), characterized by the electrodeposition currents that grew (Fig. 4.1b) with the increasing of the overpotential. The corresponding overpotential needed for the deposition is most positive for deposition of Co, followed by the deposition of Ni-Co alloy and Ni.

The electrodeposition potentials of Ni, Ni-Co and Co are very similar with values of about -0.5 V vs. SCE. The range of potentials from -0.6 to -1.0 V is the activation control region of the metal and alloy electrodeposition. Deposition at overpotentials higher than -1.1 V is characterized by a sharp increase of the current density most probably as a consequence of the formation of a dendritic deposit with more developed structures.

The hydrogen evolution reaction in alkaline solution proceeds according to the three reaction mechanisms [98] resulting in release of OH^- ions in the layer surrounding the electrode and therefore, an increase of pH. However, the bath for electrodeposition consists of the $\text{NH}_4\text{Cl}/\text{NH}_4\text{OH}$ used as a buffering agent for pH=10 and no significant increase of pH during deposition was observed.

The hydrogen overpotential can manifest itself through cathodic current efficiency (Fig. 4.2). The hydrogen evolution during the deposition of the alloys diminishes the current efficiency, depending on the electrolyte composition and on the current density. These results are in good agreement with the polarization measurements where electrodeposition performed from Co bath has a lower hydrogen overpotential and consequently a lower current efficiency. Also, the evolution of hydrogen provides some additional stirring effect and enhances the formation of disperse deposits with more developed structures. Deposition becomes dependent on hydrogen evolution since at current densities, $j \geq 200 \text{ mA cm}^{-2}$, hydrogen evolution is predominant in the overall cathodic process. Current efficiencies $\nu \leq 50\%$ (Fig. 4.2) for the Ni containing electrolyte, and $\nu \leq 40\%$ for the Co containing electrolyte at a current density of 200 mA cm^{-2} were found. The hydrogen method used for calculation of the current efficiency of the Ni, Co and Ni-Co alloys results in slightly higher values in comparison with the current efficiency data obtained by the gravimetric method. The explanation is attributed to the

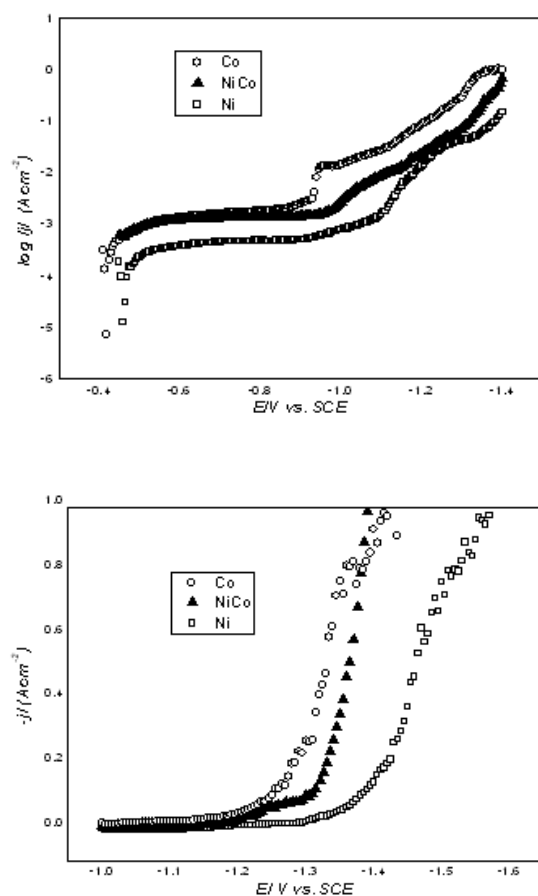


Figure 4.1: Polarization curves for galvanostatic Ni, Ni-Co and Co deposition from the solution containing: \square - 0.12 M NiSO₄; \blacktriangle -0.12 M (NiSO₄+CoSO₄) with concentration ratio Ni²⁺/Co²⁺ =1 and \circ - 0.12 M CoSO₄ in 0.5 M NH₄Cl and 3.5 M NH₄OH measured with IR drop correction. Scan rate 1 mVs⁻¹.

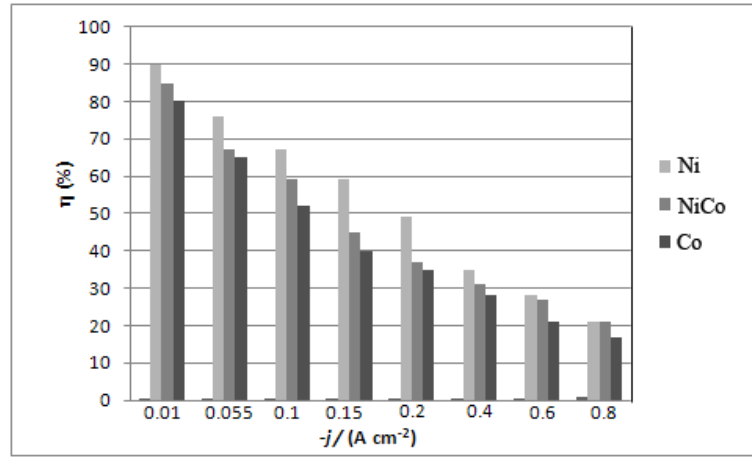


Figure 4.2: The dependence of the current efficiency on current density for Ni, Ni-Co and Co electrodeposition (electrolyte composition: Ni- 0.12 M NiSO₄, NiCo alloy - 0.12 M (NiSO₄+CoSO₄), Ni²⁺/Co²⁺ =1 and Co - 0.12 M CoSO₄).

fact that the formation of dendritic deposits at higher current densities can cause the fall of some amount of deposit into the solution resulting in less weight values and consequently diminished values of the calculated current efficiency.

4.3.2 Growth of Ni, Co and dendritic Ni-Co deposits on Cu substrates.

The needle-like deposits known as dendrites are usually obtained by electrodeposition at low cation concentrations. By definition, a dendrite represents a skeleton of monocrystals and consists of stalk and branches resembling a tree [38].

The scanning electron microscopy (SEM) of the Ni-Co deposit cross sections obtained on copper substrates has shown the gradual evolution of the dendritic formation (Fig. 4.3a-c). With an increasing current density, a detailed investigation of the deposits morphology has shown a formation of primary dendrites, which further grows with increasing current density. The sample obtained at a current density of 65 mA cm⁻² revealed the formation of a rough deposit (Fig. 4.3a). The propagation of this structure by branching produces dendrites as shown in Fig. 4.3b. The dendrites obtained at a higher current density of 400 mA cm⁻² (Fig. 4.3c) have shown more

at% Ni	at% Co	j(mA cm ⁻²)	Spot position
40	60	65	interface
22	78	65	bulk
39	61	220	interface
49.5	50.5	220	bulk
37	63	400	interface
49.5	50.5	400	bulk

Table 4.1: Cross-section composition analysis of Ni-Co alloys deposited at different current densities.

developed structures with smaller dendrites that have more pronounced secondary branches and high-order branches. A comparison with deposits obtained from pure Ni baths revealed the formation of a rough deposit only (Fig. 4.4a). In contrast, electrodeposition performed at the lowest value of the current density, i.e. 65 mA cm⁻² from pure Co bath has shown formation of dendritic growth (Fig. 4.4b). In the particular case of anisotropic Co deposition when the hexagonal close-packed lattice is formed, the growth along the high index axis does not lead to a formation of low index planes. Therefore, the HCP lattice serves as a growth site for the dendrite formation since the development of protrusions along some axis in the direction of the increasing concentration is more favorable. Repeated nucleation results in dendrite formation. Although, deposits produced from simple solution salts without additives are often dendritic or tree like, real dendritic structures are formed only from Ni-Co baths ($\text{Ni}^{2+}/\text{Co}^{2+}=1$) whereas with increasing current density, dendritic growth is even more pronounced (Fig. 4.3b and 4.3c). In this range of concentration, Ni and Co exhibit mutual solid solubility. Deposition from a bath with different $\text{Ni}^{2+}/\text{Co}^{2+}$ concentration ratios, i.e. 0.25, 0.5, 2 and 4 results in more disperse than dendritic growth [99].

4.3.3 EDX composition analysis of Ni-Co deposits.

The cross-section composition analysis of the alloys galvanostatically deposited from the solution containing the total concentration of 0.12 mol dm⁻³ of ion metal with a ratio $\text{Ni}^{2+}/\text{Co}^{2+}=1$, are presented in Table 4.1. The composition of the dendritic deposit samples near the electrode surface and in some distance is different (cf. Table 4.1).

An EDX analysis revealed that at higher current densities, i.e. 220 and

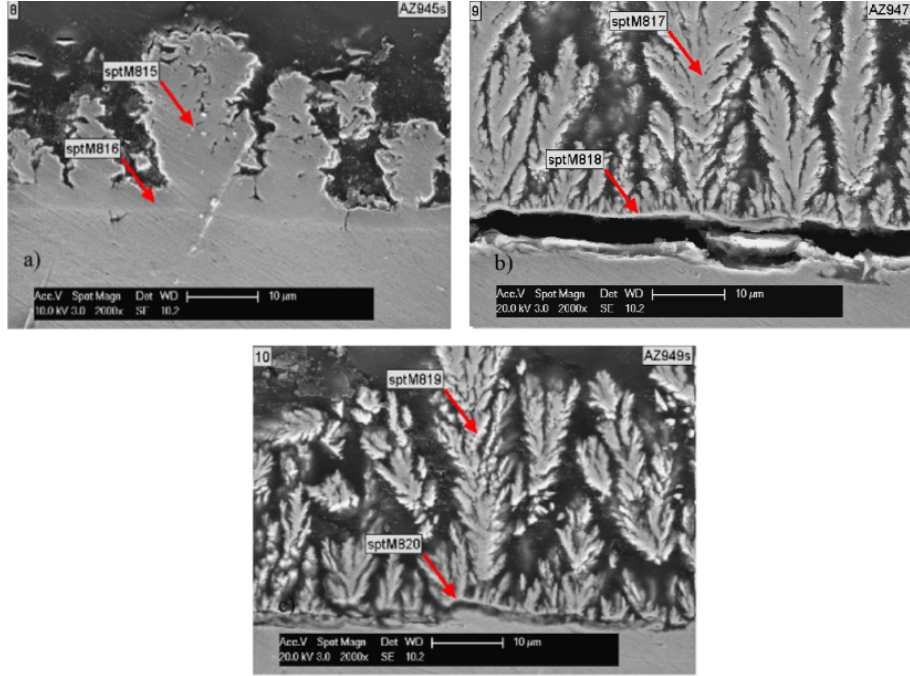


Figure 4.3: Cross-sections of Ni-Co deposits galvanostatically obtained from the solution containing 0.12 M ($\text{NiSO}_4 + \text{CoSO}_4$), $\text{Ni}^{2+}/\text{Co}^{2+}=1$ at current density: a) 65 mA cm^{-2} , b) 220 mA cm^{-2} and c) 400 mA cm^{-2} .

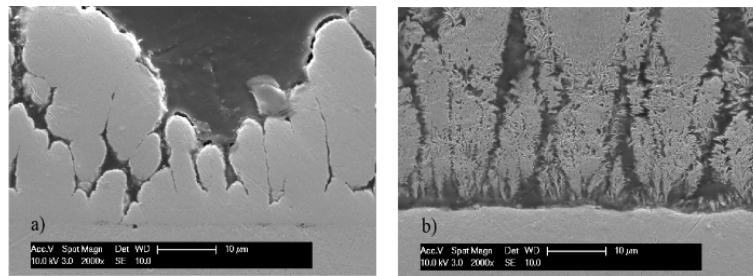


Figure 4.4: a) Cross- section of Ni deposit galvanostatically obtained from solution containing 0.12 M NiSO_4 at current density of 65 mA cm^{-2} . b) Cross- section of Co deposit galvanostatically obtained from solution containing 0.12 M CoSO_4 at current density of 65 mA cm^{-2} .

400 mA cm⁻², the deposition of the Co is enhanced near the electrode surface ($\sim 1\mu\text{m}$) due to the lower overpotential for the Co electrodeposition (sptM818, sptM820 in Fig. 4.3b-c) reaching values of the corresponding ions in the solution (sptM817, sptM819 in Fig. 4.3b-c). An explanation can be attributed to the fact that at high current densities, hydrogen evolution is higher (Fig. 4.2) providing some stirring effect and leading to the more uniform distribution of Ni²⁺ and Co²⁺ ions in the diffusion layer and therefore, resulting in a more uniform composition of the deposit. At high current densities, high growth velocities deplete the cations in the double layer and the growth is controlled by mass transfer in the electrolyte. However, for the lower current density of 65 mA cm⁻² (Fig. 4.3a), the deposition comes more under activation control, so deposition of the Co is enhanced compared to Ni.

At a current density of 65 mA cm⁻², the content of Co in the deposit is higher than in the electrolyte, as a consequence of the lower overpotential for the Co²⁺ reduction compared to Ni²⁺ as can be seen also from the polarization curves (Fig. 4.1). In the current density range 65 - 400 mA cm⁻² the increase in current density results in an increase in Ni content in the deposits. The phenomenon of anomalous codeposition (characteristic for the electrodeposition of iron group metals) is very pronounced in the production of compact deposits. In the case of disperse deposits, anomalous codeposition is much less pronounced, so that the composition of the deposits obtained at high current density is almost similar to the concentration of the metal ions in the electrolyte (Fig. 4.3c). Increasing the current density shifts the ratio of Ni and Co in the alloys closer to the value of the concentration of the corresponding ions in the electrolyte.

4.3.4 Structural analysis of Ni-Co deposits.

Nanostructured dendritic deposits were analyzed by XRD (Fig. 4.5). The Rietveld refinement procedure [88] was used to determine the structure and the grain size of the deposits. For this purpose Rietveld's refinement program TOPAS V3.0 (Bruker AXS GmbH, Germany) was used [89]. The quality of the refinement progress was controlled by monitoring the fit parameter R_{wp} , the goodness of fit (GOF), and the Durbin-Watson factor.

A detailed Rietveld's analysis revealed that Ni-Co alloys obtained by galvanostatic deposition using the same electrolyte at different current den-

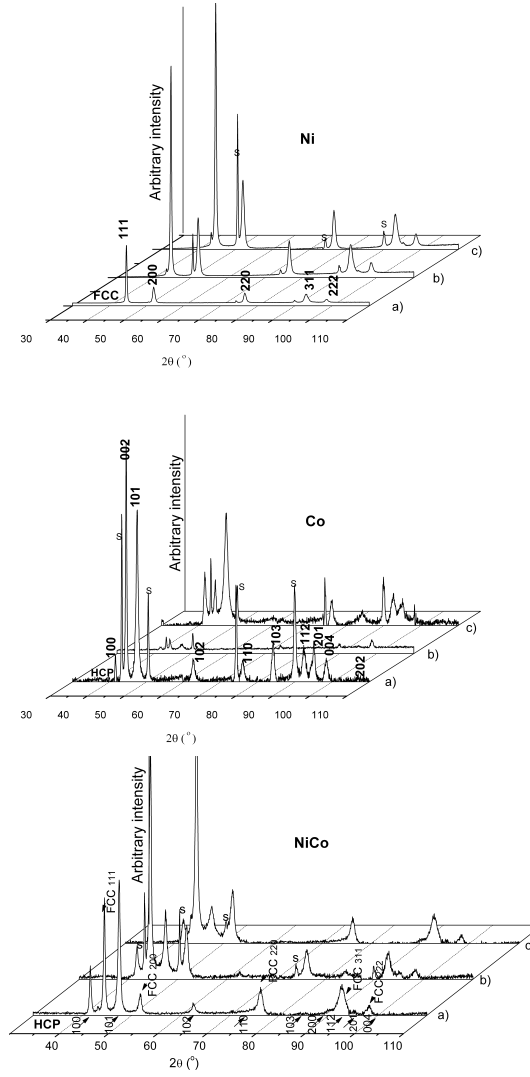


Figure 4.5: XRD of Ni, Co and Ni-Co deposits galvanostatically obtained on Cu substrates from the solution containing 0.12 M NiSO_4 , 0.12 M CoSO_4 and 0.12 M $(\text{NiSO}_4 + \text{CoSO}_4)$ at current density: a) 65, b) 220 and c) 400 mA cm^{-2} ; (S - reflections attributed to the Cu substrate).

Current density (mA cm ⁻²)	phase cont. amorphous	(at.%)		Grain size ±3 nm	Lattice parameters		Cell volume Å ³
		FCC	HCP		a Å	c Å	
65	/	72		15	3.5291		43.953
		28		19	2.5053	4.0717	22.132
220	9	20		13	3.5296		43.972
		71		11	2.4987	4.0767	22.043
400	15	5		11	3.5329		44.095
		80		10	2.4947	4.1005	22.100

Table 4.2: Phase composition, grain size and cell parameters of the Ni-Co alloys deposited from solution containing 0.12 mol dm⁻³ (NiSO₄+CoSO₄), ratio Ni²⁺/Co²⁺=1 at current density: a) 65, b) 220 and c) 400 mA cm⁻².

sities consist of a mixture of solid solutions. The crystal structure obeys the phase diagram [90] since the obtained bulk deposits are in the range of concentrations where Ni and Co exhibit solid solubility (cf. Table 4.1.)

The face-centered cubic phase (FCC) whose structure is defined by the Fm $\bar{3}$ m space group and hexagonal-close packed (HCP) defined by the space group P6₃/mmc, were identified. By increasing density, structure and composition of the obtained deposits is progressively changed.

The increase of current density leads to the increase in the content of FCC phase as well as the formation of significant amounts of amorphous phase (Table 4.2). Furthermore, it can be seen that the cell volume of the FCC phase increases slightly with increasing current density (Table 4.2).

Corresponding XRD patterns of parent metals, Ni and Co (Fig. 4.5) show the FCC phase for parent Ni and the HCP phase for parent Co. With increasing current density the grain size decreases. In the range of the current density of 65 mA cm⁻² to the highest current density used for deposition, i.e. 400 mA cm⁻², grain sizes decreases for Ni from about 20 nm to 10 nm and for Co from about 45 nm to 25 nm.

At a current density of 65 mA cm⁻², mainly the HCP phase, equilibrium phase of Co stable at room temperature is generated, and it is in good correlation with EDX results of the bulk material (Table 4.1). At higher electrode polarization, i.e., far from equilibrium, at a current density of 220 mA cm⁻², the FCC phase grows preferentially on the polycrystalline FCC structured Cu substrate. Still, an amount of 20% HCP phase (Co) calculated by XRD Rietveld refinement is present (Table 4.2). Taking into account the

amount of an amorphous phase of 9%, this means that approximately 70% of the deposit is composed of the FCC solid solution.

In the case of deposition at a current density of 400 mA cm^{-2} , even further from equilibrium in comparison with deposits obtained at 220 mA cm^{-2} , growth of FCC phase is more pronounced (Table 4.2). As determined by TOPAS using the Rietveld method, the disperse deposits with more developed structures obtained at high current density, i.e. 400 mA cm^{-2} , also contained up to 15% amorphous phase. The amorphous phase content, attributed to the enhanced background intensity, was estimated by determination of the integral area of the broad diffuse diffraction halo which cannot be assigned to distinct diffraction maxima correlated with crystalline phases and by comparing with samples without an amorphous phase.

The classical expression for the steady state nucleation rate, J , is given by Eq.(1.28). The nucleus probability formation is enhanced by the increase of overpotential η . The electrochemical deposit formation at higher current densities is accompanied by higher overpotential values. Based on the equation, it is obvious that a further increase of the current density decreases the grain size of the deposits down to 10 nm (Table 4.2).

4.3.5 Surface morphology of Ni-Co deposits

The nature and magnitude of the applied electric field across the counter-working electrode arrangement determines: 1) grain size, 2) surface roughness and 3) dendritic electrodeposition growth.

The surface roughness of the Ni-Co deposits was determined by 3D SEM reconstruction of the specimen surface (Fig. 4.6a-c). Such a characterization gives quantitative results of the mean surface roughness: $\sigma = 3 \text{ }\mu\text{m}$ in the case of the deposit obtained at a current density of 65 mA cm^{-2} (Fig. 4.6a) and $\sigma = 1 \text{ }\mu\text{m}$ in the case of the deposits obtained at current densities 220 and 400 mA cm^{-2} (Fig. 4.6b-c). The value σ represents a picture of local surface irregularities and gives the height deviation of the surface from the mean level. An increase in the current density results in a decrease of the mean roughness because at higher current densities the amount of crystal nuclei on the surface is enhanced causing a more homogenous grain size distribution and therefore, formation of a smoother deposit.

On the other hand, the effective surface roughness increases due to the increase of the coarseness of the deposit with increasing current density

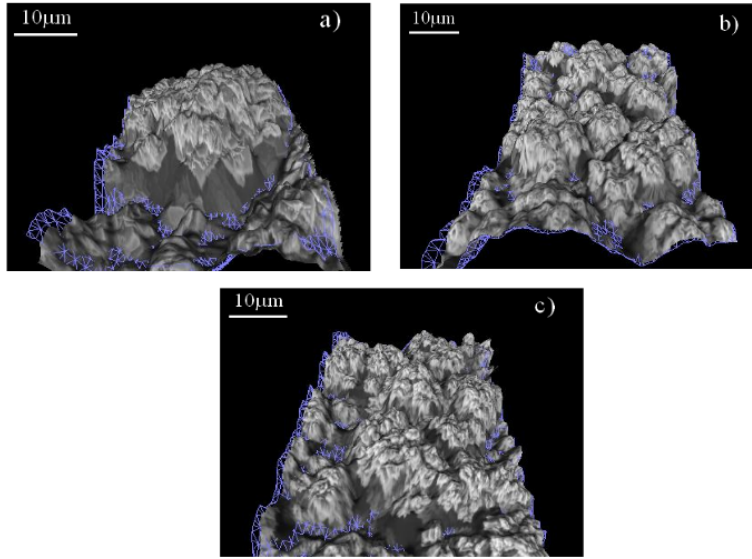


Figure 4.6: 3D SEM reconstruction of the surfaces of Ni-Co deposits galvanostatically obtained at current densities: a) 65, b) 220 and c) 400 mA cm⁻².

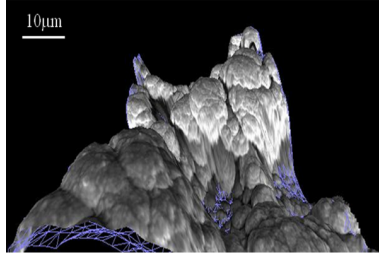


Figure 4.7: 3D SEM reconstruction of the surface of Ni deposit galvanostatically obtained at current density of 400 mA cm⁻².

(Fig. 4.6b-c). This surface amplification leads to the initiation of preferential growth of protrusions or dendrites. The Ni deposits obtained from simple solution salts are characterized by a cauliflower surface morphology and mean surface roughness values of $\sigma = 4 \mu\text{m}$ for all analyzed deposits obtained at current densities of 65, 220 and 400 mA cm⁻². A typical 3D SEM reconstruction of the surface of Ni deposit is presented in Fig. 4.7.

Co deposits have shown mean σ values of $1 \mu\text{m}$ and the result of the deposition is the appearance of smoother deposits in comparison to Ni deposits (Fig. 4.8). One of the consequences of hydrogen evolution is that H₂ bubbles are attached to the surface during deposition and therefore can cause the

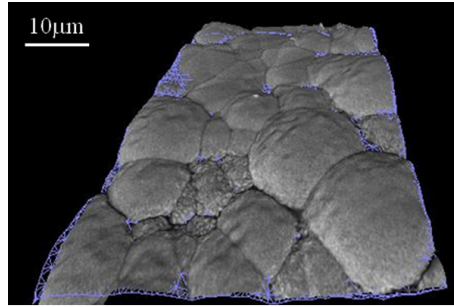


Figure 4.8: 3D SEM reconstruction of the surface of Co deposit galvanostatically obtained at current density of 220 mA cm^{-2} .

growth of the deposit around the bubbles before they are released. Such impact of hydrogen during the codeposition of Ni can cause larger mean surface values of Ni deposits. The confirmation of these is the presence of craters or holes in the Ni deposit (Fig. 4.9a) clearly visible on the surface of a typical SEM micrograph. The bottoms of the holes consist of small Ni particles, while around them during codeposition, larger cauliflower particles are formed. A faster growth of the deposit around bubbles is caused by increasing current density because the overall current is concentrated around bubbles which are not conductive. This directly results in the formation of high surface area disperse deposit confirmed by 3D SEM results and in the value of surface roughness of $\sigma = 4 \text{ } \mu\text{m}$. A typical SEM micrograph of particles of Co deposit (Fig. 4.9b) separated by boundaries is characterized by the platelet morphology with very fine nanosized crystallites growing on the surface during codeposition from the Co- containing bath. In both cases, the particles consist of smaller agglomerates of grains.

The surface morphology of the Ni-Co deposit is characterized by the formation of dendrites. Figure 4.9c. shows cauliflower-shaped particles with dendrites growing on their surface. Increasing the overpotential under a strong hydrogen codeposition leads to dendritic deposits formation in the Ni-Co alloy deposition.

The basic cause of dendritic growth is the formation of the diffusion field of depositing ions that favors the development of protrusion in the direction of increasing concentration. Dendrite exhibits a highly ordered structure and grows and branches in well defined directions.

The motion of the growing interface is controlled by a concentration of the

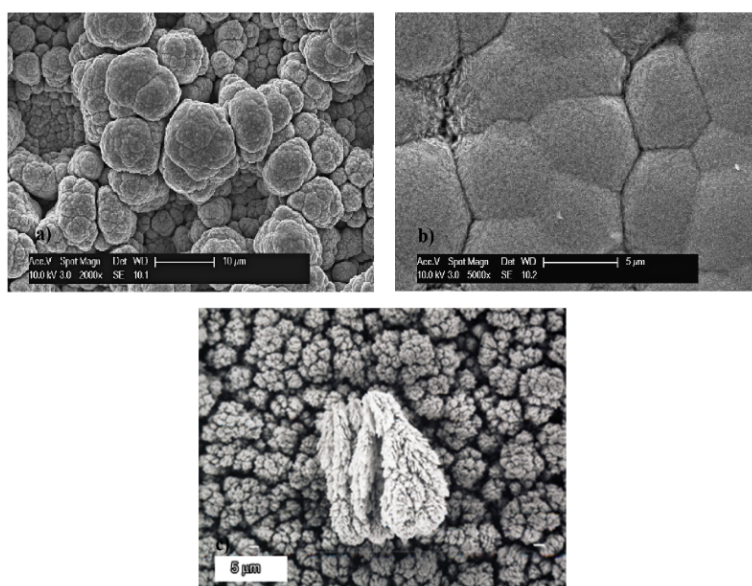


Figure 4.9: a) SEM micrograph of Ni deposit formed by galvanostatic deposition at current density of 400 mA cm^{-2} . b) SEM micrograph of Co deposit formed by galvanostatic deposition at current density of 220 mA cm^{-2} . c) SEM micrograph of Ni-Co dendrites formed by galvanostatic deposition at current density of 400 mA cm^{-2} .

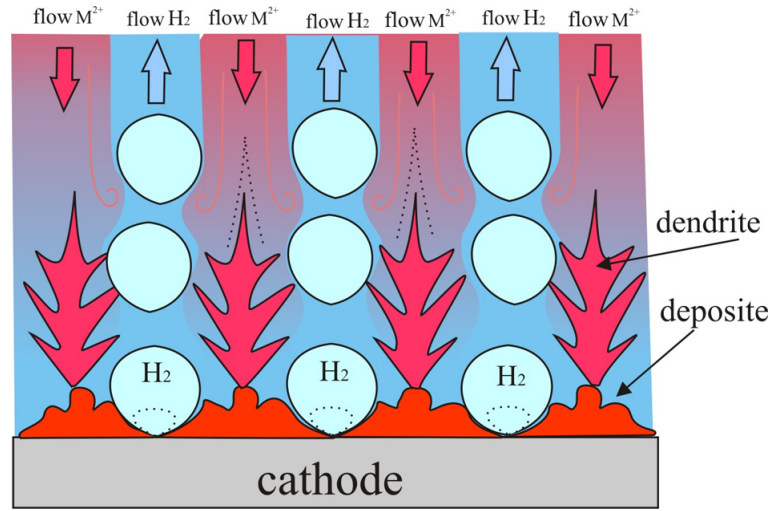


Figure 4.10: Schematic representation of the dendrite formation.

diffusing particle and electric potential [86]. According to Fick's law, which satisfies equation for a non-local growth process, such as electrodeposition, the low value of the growth velocity and large value of the diffusion length enhance deposition preferentially on protrusions.

Well defined organizations, such as dendritic, are formed under such conditions. A schematic representation of the common effect of hydrogen and electrolysis conditions, which favor the dendrite formation, is shown in Fig. 4.10.

Apart from decreasing the concentration of the depositing ion, the formation of a dendritic deposit can also be enhanced by increasing the concentration of the supporting electrolyte, increasing the viscosity of the solution, decreasing the temperature, and decreasing the velocity of motion of the solution.

4.4 Conclusions

The grain size of Ni-Co deposits is determined by the applied overpotential. Increasing current density results in finer grain deposits. The structure of Ni-Co deposits is characterized by solid solution formation; increasing current density results in an increase in the volume fraction of the cubic phase. The morphology of Ni-Co is affected by conditions applied during electrolysis. Morphology is determined by the nature of depositing ions. The Ni deposit

exhibits spherical growth during deposition, which manifests itself by typical cauliflower structure; the surface pattern of the Co deposit is characterized by a platelet structure. The composition of the alloy deposit is determined by the hydrodynamic conditions in the near electrode layer; with increasing current density the hydrogen evolution is predominant, leading to the more uniform distribution of Ni and Co ions in the double layer, and, therefore, the composition of the deposits reaches the real value of the corresponding ions in the solution. The whole process determines the density of nucleation sites and the final morphology of the deposit. It was found that the formation of dendritic Ni-Co alloy deposits is enhanced by increasing the current density and leads to a decrease of the mean roughness. The number of atoms in the nucleus having the critical radius declines with the overpotential square, resulting in a more rapid nucleation at higher current density and in the formation of smaller crystals with the average grain sizes of 10 nm. The increase of current density leads to an increase of the volume fraction of the cubic phase in the nanocrystalline alloy deposits with a corresponding decrease in the grain size.

Chapter 5

Substrate Controlled Electrodeposition of CoNi Porous Layers with Enhanced Catalytic Properties ¹

5.1 Introduction

Electrodeposition is regarded as a viable process for nanofabrication and - even though electrocrystallisation has received considerable attention from both theoretical and experimental viewpoints - there is still much to be discovered in the production of tailored nanosized structural features especially for alloys [3]. Recently, attention has been paid to deliberate dendritic nanomaterial fabrication by electrochemical procedures [38, 100, 101, 102]. Dendritic structures formed by electrodeposition on the surface of chosen substrates can yield a high surface area that is advantageous in certain electrochemical devices (e.g. fuel cells, sensors and batteries). An open structure is crucial for high rates of mass transport, which is important generally for catalysts and electrodes [103, 104]. A new technique based on hydrogen co-evolution during electrochemical deposition of metals (Cu, Sn) and their alloys has been used to produce open dendritic structures. Hydrogen bubbles seem to be important as a dynamic negative template; the resulting struc-

¹Based on a submitted article

tures are foams with porous walls. It is an aim of this work to investigate the influence of the substrate and that of hydrogen bubble detachment on the formation of dendritic foam structures. Therefore, two very different substrates, polycrystalline Cu, PC, (grain size about 50 nm) and single-crystalline Cu (111), SC, were applied. Care was taken to use a single-crystalline substrate containing a minimum of impurities and structural defects to ensure a restricted number of nucleation sites in comparison to the polycrystalline Cu substrate during electrodeposition. A special attention was devoted to the phenomena of wetting. Increasing interest in the construction and application of surfaces with switchable liquid-solid adhesion for various practical purposes in smart and fluid-controllable devices, mainly tailored by surface morphology emphasizes the importance of fundamental research [105]. Wettability plays an important role in electrodeposition, that can be even used as a novel approach for selective growth of porous hierarchical structures in superhydrophilic region [106]. Therefore, at first instance, the surface wettability governed by microstructure and interfacial energy, was investigated and compared for both substrates to give insight into the nature of solid-liquid-gas interactions during electrolysis in aqueous solutions.

One of the greatest challenges in the forthcoming years is unquestionably energy storage where nanostructured materials become increasingly important due to their unique properties [59]. Electrodeposition with high applied overpotential during metal plating represents an excellent approach to achieving hierarchical structures with nanometer size domains. In recent years, Co compounds have been used as positive electrode materials to improve electrochemical performance [107]. As charge/discharge processes in general are limited by the reaction kinetics, the search for a device that can deliver high power is an active field [108]. Therefore, the preparation of materials with high surface area can improve device performances because more material is available on the surface for charge compensation as well as for energy storage [108].

5.2 Experimental Procedure

Electrodeposition was conducted in the galvanostatic regime at a current density of 0.1 A cm^{-2} at room temperature without stirring, using the potentiostat IMP 83 PC-10, (Jaissle, D). The electrodeposition was performed on

both, polycrystalline Cu and single-crystalline (111) oriented Cu substrates from a simple bath without using organic additives in a solution containing: 0.025 M NiSO_4 +0.1 M CoSO_4 ; 0.5 M NH_4Cl and 3.5 M NH_4OH (Sigma-Aldrich) at pH=10. As an anode, a Ti plate covered with $\text{RuO}_2/\text{IrO}_2$ (10 cm^2 geometric area), placed parallel at the distance of 2 cm to the substrate, was used. The polycrystalline Cu substrate (a platelet with dimensions 1x1cm and a thickness of 1mm) having a grain size of about 50 nm as determined by XRD was cut out from Cu rods electrolytically prepared. The surface preparation of the polycrystalline Cu substrates prior to deposition included polishing with SiC emery paper (1200), washing and treating in an ultrasonic bath, etching in concentrated HCl, cleaning with distilled water and drying in a stream of compressed nitrogen. The single-crystalline substrate was prepared from a Cu single-crystal of high purity (5N) grown by a modified Bridgman technique. The single-crystal was cyclically annealed and furnace cooled to minimize the density of the grown-in defects ($<5 \cdot 10^6 \text{ cm}^{-2}$) [109]. The single-crystal was oriented by X-ray Laue method and cut parallel to (111) planes. The surface treatment of the single-crystalline substrates was the same as that of the polycrystalline ones plus a final electropolishing step in a solution of a mixture consisting of H_3PO_4 and $\text{CH}_3\text{OH}/\text{C}_2\text{H}_5\text{OH}$.

Cyclic voltammograms (CV) were obtained in a three electrode cell using the potentiostat VoltaLab 40, PGZ 301 (Radiometer Analytical, F). The working electrodes were prepared from polycrystalline (PC) and single crystalline (111) Cu substrates (SC) cut by spark erosion into a disk with a diameter of 3 mm. The counter electrode was a Pt mesh with a high surface area much larger than that of the working electrode and a silver chloride electrode (Ag/AgCl) was used as a reference electrode.

The sessile mode is a contact angle technique used to quantitatively measure the wetting of a solid by a liquid. Contact-angle (CA) measurements were carried out by applying droplets of 10 μl of distilled water to 1 cm^2 of the PC and SC substrate surface. The static CA was measured using an instrument equipped with a CCD camera (Krüss, DSA10). The mean value of the CA is given as an average of 5 measurements.

The surface roughness measurement was performed on an evaluation length of 1.75 mm on bare PC and SC substrates using the computer controlled device Perthometer S2, Mahr (D). Each measurement was repeated three times.

The phase content and the crystallite size were determined by X-ray diffraction (XRD) [110] using a X'Pert Powder diffractometer from PANalytical, (CuK α 40 kV/ 30 mA) in Bragg-Brentano geometry. The measurements were performed in step-scan mode over the range $2\theta=20-110^\circ$ with a step size of 0.05° and a counting time of 10 s/step. Evaluation of the phase volume and crystallite size was done by Rietveld refinement [88] using the TOPAS software (Bruker AXS, D). The stress determination [111] was done on the same device using an automatic Eulerian cradle. The area of the sample irradiated by the X-ray beam was in the range of several mm². D-lattice spacing measurements were performed for the stress detection on the lattice planes: (100), (002), (101) of the hexagonal Co phase. This procedure was repeated for each sample at three different azimuthal positions (due to the assumed radial stress symmetry a mean value of d was taken) and at six different tilt angles (ψ). For each sample orientation a corresponding strain value $\epsilon(\psi)=(d-d_0)/d_0$ was calculated. In this relation d_0 refers to the lattice spacing of the stress-free reference sample (electrodeposited HCP Co₉₀Ni₁₀ powder embedded in epoxy resin). The residual stress in the samples was then calculated by means of linear regression in an $\epsilon(\psi)$ versus $\sin^2 \psi$ diagram using the modified equation describing a stress state with cylindrical symmetry ($\sigma_{22}=\sigma_{11}$):

$$\epsilon(\psi) = \frac{1+\nu}{E}(\sigma_{11} - \sigma_{33})\sin^2(\psi) + \frac{1}{E}(\sigma_{33} - 2\nu\sigma_{11})$$

whereby σ_{11} and σ_{33} refers to the stress component parallel and normal to the layer surface, E denotes the corresponding Young's modulus (stiffness), and ν refers to the Poisson's ratio of the material [112, 113]. The surface morphology of the obtained deposits was analyzed with a scanning electron microscope (SEM) with a field emission gun (XL 30 ESEM-FEG, FEI). The profile and roughness measurements, as well as 3D area analysis directly from the stereoscopic images of the specimen surface were carried out using MeX software from Alicona (A).

5.3 Results and discussions

5.3.1 Wettability of single-crystalline Cu (111) and polycrystalline Cu substrates

The wetting of a solid with water, with air as a surrounding medium is dependent on the interfacial tensions, γ , of solid-air, solid-liquid and liquid-air. The ratio between them determines the contact angle. A contact angle (CA) less than 90° for water indicate hydrophilic and higher than 90° hydrophobic surfaces. CA measurements revealed mean angles in the hydrophilic region for both substrates, $CA=85^\circ \pm 1.5^\circ$ for bare SC and $CA=68.5^\circ \pm 1.2^\circ$ for bare PC. Lower wettability on flat and smooth surface of electropolished substrate can be explained by the Wenzel model [114]. The area of material in contact with liquid on rough surface of PC substrate is higher than on the smooth surface of SC substrate and CA decreases according to Wenzel model. In other words, the amplification effect of surface roughness causes increased hydrophilicity on rough substrate surface of polycrystalline Cu. This assumption is confirmed by surface roughness measurements obtained on bare PC and SC substrate that yield mean roughnesses (Ra) of $0.211 \mu\text{m}$ for PC and $0.079 \mu\text{m}$ for SC substrates, respectively. In addition, the SEM image (Fig 5.1) shows locally enhanced roughness of PC compared to the mirror-like SC substrate. Wettability is also influenced by microstructure of the substrate, because crystal orientation of the surface can significantly alter surface wettability and consequently the value of CA [115]. Hasouna et.al. showed that according to the Young equation CA increases with increasing fraction of grains having their surface parallel to the crystallographic (111) plane, since the surface energy for the (111) plane is smallest compared to the surface energy of any other plane of the FCC structure. This is in accordance with our result of a higher CA for the SC substrate with (111) surface as the surface energy is lower compared to that of any PC substrate.

5.3.2 Surface characteristic of microscopically rough CoNi dendritic deposits on single-crystalline Cu (111)

Production of dendritic deposits can be achieved in the galvanostatic regime at high current density in additive-free aqueous electrolytes, leading simultaneously to significant hydrogen evolution as a parallel and competitive

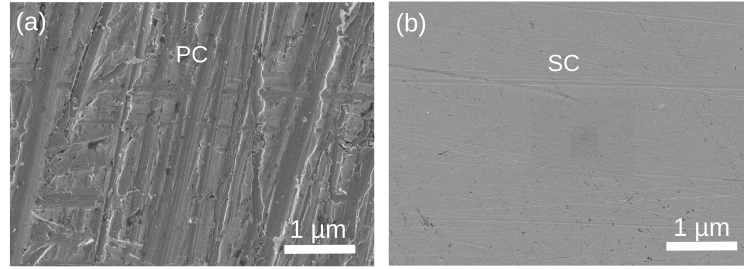


Figure 5.1: SEM image of the surface of the polycrystalline Cu substrate (PC) and the single crystalline Cu (111) substrate (SC).

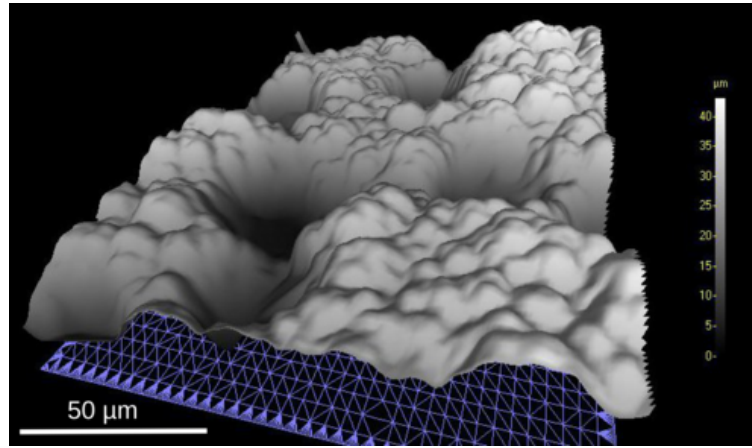


Figure 5.2: 3D SEM reconstruction of the foam surface of CoNi deposited on single crystalline Cu (111) substrate.

cathodic side reaction [116]. We have shown in previous works that the conditions necessary for production of dendritic deposits on Cu polycrystalline substrates depend on the electrolyte composition and on the current density. Production of dendritic deposits on polycrystalline substrates were enhanced by higher Co^{2+} concentration in the electrolyte and by increasing the current density. However, by performing electrodeposition at a constant, relatively low current density (0.1 A cm^{-2} for 39 min) on SC it was possible to achieve a morphology characterized by a very pronounced dendritic structure (Fig. 5.2) with circular depressions of around $50 \mu\text{m}$ diameter and about $40 \mu\text{m}$ depth.

5.3.3 Morphology of CoNi layers on polycrystalline Cu and single-crystalline Cu (111) substrates

For comparison, electrodeposition was performed under the same conditions on polycrystalline Cu and single-crystalline Cu (111) substrates. Figure 5.3a shows a SEM image of CoNi deposited on polycrystalline Cu using a current density of 0.1 A cm^{-2} . Particles with platelet structures and a size from 1 to $5 \mu\text{m}$ composed of nanograined crystallites are obtained. Figure 5.3b shows a SEM cross section image of the $30 \mu\text{m}$ thick CoNi deposit (D). The deposit is rather dense although it contains some voids and a crack (C) at the interface between the substrate (S) and (D). At larger scale the surface is smooth without large craters (Fig. 5.3c). The formation of the homogeneous fine grained deposit is a consequence of the surface properties of the substrate. The surface structure of the polycrystalline Cu substrate formed by nanosized grains of different orientation and their grain boundaries provides numerous nucleation sites, so the crystal nuclei density on such a surface may be very high. The high nucleation density results in a homogenous fine-grained deposit (Fig. 5.3c).

In Figure 5.3d,e and f SEM micrographs of CoNi electrodeposited foams on a single crystalline (SC) substrate are shown. The deposit shows a platelet structure as in the case of CoNi electrodeposited on the PC substrate, but with a finer morphology (compare Fig. 5.3a and d). Applying the same experimental conditions as in the case of deposition on the PC substrate, the deposits formed on the SC substrate consists of approximately 10 times smaller platelets (length of $0.1\text{-}0.5 \mu\text{m}$) that are elongated in this case. Furthermore these deposits exhibit an open dendritic structure and the platelets contain very fine grains (Fig. 5.3d-f and Table 5.1).

It is proposed that the formation of hydrogen bubbles formed on the CoNi deposit during the initial stage of electrocrystallization due to the influence of the SC substrate, provides conditions for the formation of the 3D open dendritic foam structure on the whole electrode surface (Fig. 5.3d). Intensive hydrogen evolution during alloy growth acts as a dynamic negative template in a manner already reported for single metal electrodeposits [38] for the formation of highly developed open dendritic deposits. This process leads to a fine nanograined deposit around the bubble and larger pore sizes of the deposit (Fig. 5.3f). In contrast, the CoNi deposit obtained on the PC

substrate shows only a few craters that are rather shallow (Fig. 5.3c).

In addition, the surface roughness of the substrate prior to deposition plays also an important role for the structure of the deposit. It is expected that the surface roughness correlates with the density of the structural defects of the substrate due to the special surface treatment. Accordingly, the low density of the structural defects of the substrate (e.g. grown-in dislocations and stacking faults [109]) resembles the density of the main dendrites that occur within the pronounced dendritic structure (about 10-20 μm apart).

Based on Faraday's law and weight measurements of the dried deposits, current efficiencies were calculated. In both cases the current efficiency was approximately 50%. Therefore, it can be concluded that the deposition process is not strongly influenced by the concurrent hydrogen evolution reaction per se, but rather the bubble detachment size. Further growth of such open dendritic structures formed on the single-crystalline substrate provides numerous crystallization sites and results in a uniform distribution of fine nanograins that deposit in all directions forming very fine platelets.

5.3.4 Microstructure of CoNi layers

CoNi forms a solid solution over the whole range of compositions. At low Ni contents ($< 25\text{at.}\%$) the hexagonal closed packed (HCP) phase is formed whereas at higher Ni contents the face centered cubic (FCC) phase is the equilibrium phase. In Table 1 the results of the XRD measurements are summarized. The deposits on the polycrystalline substrate with a thickness of 30 μm have an average crystallite size of the HCP phase of 14 nm. Nevertheless, XRD analysis yields a Ni-rich FCC phase of 7 wt% for the deposit near the polycrystalline substrate. At the beginning of the deposition a higher content of Co would be expected, as deduced from the polarization diagram due to the lower overpotential for Co deposition on a Cu substrate in comparison to Ni for the electrolyte used in this case [99]. This is not the case here, possibly because for the current density applied the deposited metal follows the structure of the substrate by quasi-epitaxial growth that leads to the alignment of crystal planes parallel to the substrate [37]. Therefore, at the beginning of the deposition process the growth rate of the Ni-rich FCC phase on the FCC Cu substrate is enhanced, as was also supported by localized energy-dispersive X-ray spectroscopy of the cross-sectional sample

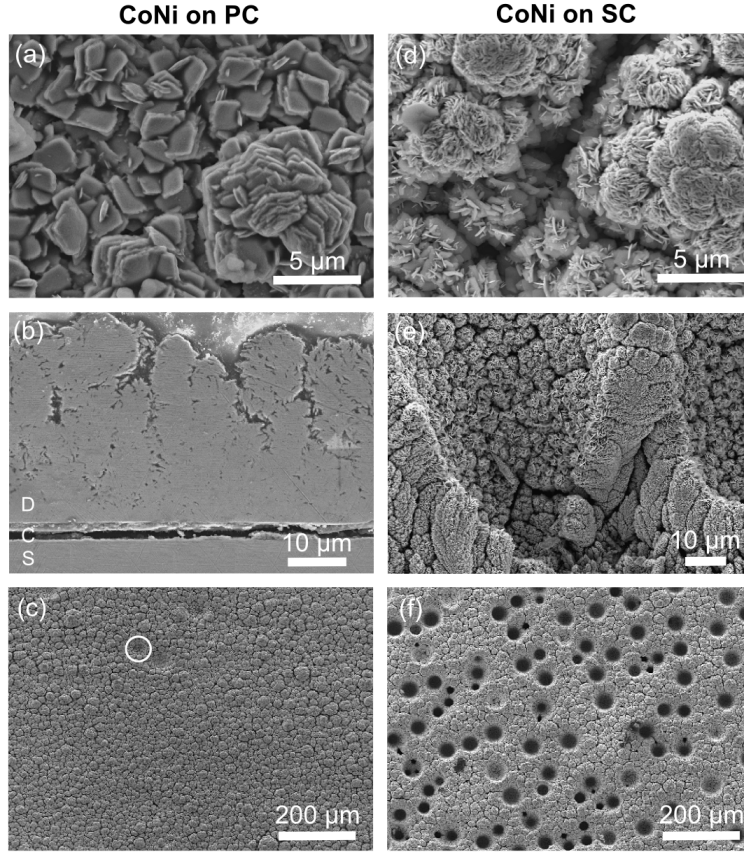


Figure 5.3: SEM micrographs of $\text{Co}_{90}\text{Ni}_{10}$ electrodeposits on the different substrates after the same deposition time ($t=39$ min); (a)-(c) polycrystalline Cu substrate (PC). (a) Top view of the deposit (thickness $30\text{ }\mu\text{m}$) showing platelets ($1\text{--}5\text{ }\mu\text{m}$). (b) Cross-section of (a), the Cu substrate (PC) and the crack (C) between the substrate and the deposit (D) are marked. (c) Dense CoNi deposit with just a few craters (marked in the image) obtained during hydrogen codeposition. (d)-(f) (111) Cu single-crystalline substrate (SC). (d) Top view shows an open dendritic structure dominated by big dendrites (about $20\text{ }\mu\text{m}$ apart) that are formed of small elongated platelets ($0.1\text{--}0.5\text{ }\mu\text{m}$). (e) 3D dendritic foam structure of CoNi deposit. (f) Plan view of the open dendritic structure made on the single-crystalline substrate.

(Fig. 5.3b and e). On further deposition, as expected, the lower overpotential for Co deposition in comparison to Ni increases the Co content in the deposit building up the HCP structured $\text{Co}_{90}\text{Ni}_{10}$ phase. The anomalous character of the codeposition of Co^{2+} and Ni^{2+} ions from the solution, where the less noble element (Co) is deposited preferentially to the more noble (Ni), is characteristic for electrodeposition of iron group metals (Co, Ni, Fe) [117], and is enhanced in addition by the lower Ni^{2+} concentration in the electrolyte.

X-ray patterns of CoNi deposited both on the single crystalline and the polycrystalline Cu substrate using the same deposition conditions are shown in Fig. 5.4. Rietveld analyses yield an average grain size of 9 nm for the deposit on the SC substrate and thus a grain refinement when compared to CoNi with an average grain size of 14 nm deposited on the PC substrate (Table 1). Peaks corresponding to the HCP phase (marked by *) are dominating. In addition to the HCP phase, some peaks corresponding to the FCC phase (marked by x) are identified. In the XRD intensity profile of CoNi the (111) Cu reflection of the single-crystalline substrate is present since the deposit is porous with pronounced open structure (Fig. 3e). Some peaks corresponding to the Cu polycrystalline substrate are observed at higher 2θ angles since the X-ray beam partially penetrates the deposited layer (Fig. 5.4b).

Deposits on the single-crystalline substrate show a higher percentage of the Ni-rich FCC phase (20%) than on those of the polycrystalline substrate (7%) (Table 1). The deposition of the FCC phase occurs in direct vicinity to the Cu substrate due to the epitaxial growth during deposition. As epitaxial growth is more pronounced on SC it results in a higher percentage of Ni-rich FCC phase. In addition, the open structure increases the relative phase content of the FCC structure since the XRD information obtained from the near substrate layer is increased. The epitaxial growth on Cu was additionally checked by using HCP Ti as a substrate and applying the same conditions: in this case only the HCP phase and no FCC phase has been observed.

5.3.5 Effect of the hydrogen bubble desorption on the formation of an open dendritic structure

A schematic drawing comparing the electrodeposition on the single-crystalline (111) substrate with that on the polycrystalline substrate is presented in Fig. 5.5. Although the current efficiency was similar in both cases, implying the same rate of hydrogen evolution, the microscopic location of bubble

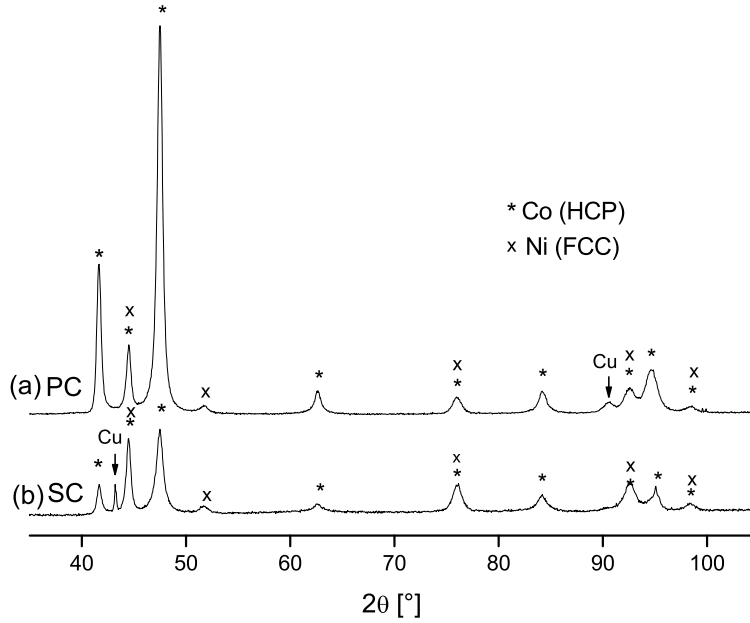


Figure 5.4: $\text{Co}_{90}\text{Ni}_{10}$ electrodeposits; the XRD patterns show the intensity (in arbitrary units) as a function of the scattering angle 2θ . (a) polycrystalline Cu substrate, (b) single-crystalline Cu (111) substrate.

formation differed. In the case of the electropolished single-crystalline (111) substrate the low density of grown-in defects offer a restricted number of nucleation sites in comparison to the polycrystalline Cu substrate. In a first step an epitaxial Ni-rich FCC layer is formed with an increased deposition at surface steps near structural defects. The localized flow of the metal ions leads to the coalescence of hydrogen bubbles formed at the edges of the deposited islands (Fig. 5.5c). Hydrogen coalescence leads to the formation of larger hydrogen bubbles resulting in the outgrowth of an open foam structure with electrolysis (Fig. 3d,e). Larger hydrogen bubbles attached to the substrate result in very large and deep holes (Fig. 5.3e, f).

Furthermore, the hydrogen bubble desorption is affected by the surface tension and therefore depends on the substrate rather than on the kinetics of the hydrogen evolution reaction [29]. The single-crystalline substrate is, apart from the defects, almost atomically flat while the polycrystalline substrate provides a surface that is very rough on a microscopic scale. Thus, in analogy to the Wenzel model to describe wettability, gas bubbles do not stick well to the rough surface and thus the radius at which bubbles detach

from the surface is small [118]. In the case of the single crystalline substrate however the wettability is reduced and the bubble departure radius is larger. The gas bubbles that stick to the substrate cover the substrate partly templating the formation of holes in the deposited foam.

Higher local current densities concentrated around bubbles, due to their non-conductivity, causes faster growth of finer dendrites containing small platelets and fine grains. The microscopic current distribution is changed due to the adsorption of bubbles decreasing both conductivity and the effective electrode area [85]. As a final result, the current density distribution and coalescence of hydrogen bubbles create porous, foam-like, dendritic structures on different length scales (Fig. 5.3e, f and 5.5d). In contrast, due to multiple nucleation sites, the deposit obtained on the polycrystalline substrate shows no preferential hydrogen evolution sites. Thus a dense deposit is formed incorporating more hydrogen and containing only a small number of very shallow craters (Fig. 5.3c).

5.3.6 Internal stresses of the CoNi layers

For the electrodeposits on the PC substrate compressive stress (Table 5.1) leads to the formation of cracks at the interface (Fig. 5.3b). To determine the stress the anisotropy of the elastic parameters in the deposited crystals were taken into consideration in a first approach. The elastic stiffness constants in the crystallographic direction corresponding to the observed specific diffraction peak were used for the residual stress calculations. Such an assumption would fit to the Reuss model (which assumes a homogenous stress)[119]. However, the stress values calculated from the different diffraction maxima show a strong variation suggesting that the Voigt model [120] is more adequate as it assumes a homogenous strain. This behaviour is most likely caused by the specific grain-grain interaction properties of the material. For further determination of residual stress determinations isotropic elasticity constants [121] were applied.

The presence of compressive stress is in agreement with the results obtained for conventional direct current plating of nickel electrodeposits [48, 55]. The high compressive stress is expected for deposits obtained from additive-free electrolytes and for deposits with structural parameters different to the substrate. Impurities in the deposit can also significantly increase the internal stress. In electrodeposited Ni, impurities are typically limited

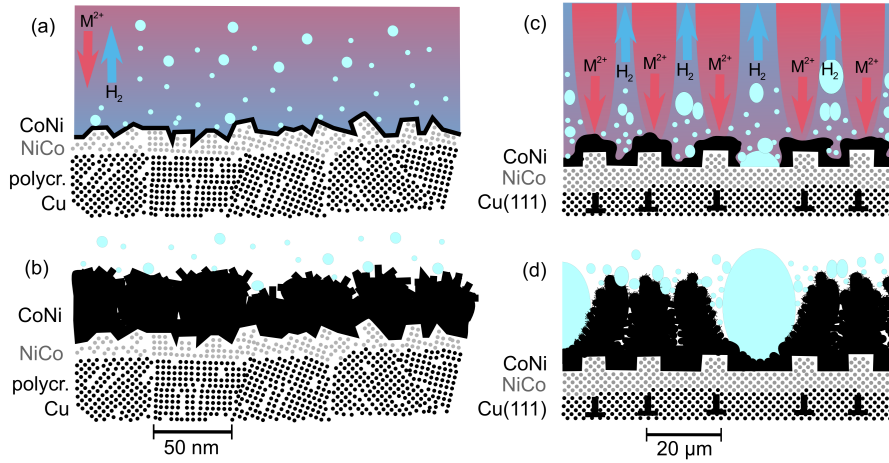


Figure 5.5: Schematic representation of the CoNi electrodeposition process during concurrent hydrogen evolution reaction. Flow of metal ions and hydrogen bubbles are indicated. (a) Initial stage of electrodeposition with epitaxial growth of FCC NiCo on polycrystalline Cu dominated by the numerous nucleation sites of the inhomogenous surface of the substrate. The hydrogen bubble departure radius is rather small due to the high surface roughness. (b) Final stage of electrodeposition of a dense and thin CoNi deposit on polycrystalline Cu incorporating more hydrogen. (c) Initial stage of electrodeposition on single-crystalline (111) Cu substrate with epitaxial growth of a few layers of (111) NiCo influenced by surface steps; the observed formation of CoNi dendrites (10-20 μm) apart corresponds to the density of steps. The hydrogen bubble departure radius is much larger as bubbles stick to the flat surface. (d) Formation of a dendritic foam structure as a consequence of hydrogen template.

to interstitial types, particularly hydrogen, which can exist in solid solution or in form of bubbles within the grains in the grain boundaries and triple junctions [55, 122, 123]. During the electrodeposition of the $\text{Co}_{90}\text{Ni}_{10}$ deposit, an intensive parallel hydrogen evolution reaction occurs. Therefore, it can be assumed that incorporation of hydrogen takes place resulting in an increase of internal stress.

The XRD measurements of the CoNi deposits on the SC substrate show much lower values of the internal stress (Table 5.1) than those on the PC substrate. In general, a decrease in grain size is accompanied by an increase of the internal stress [124] but in the present case the positive effect of the SC substrate is more than compensated since it leads to reduced stress even though the grain size is reduced (Table 5.1). In the case of the SC substrate less hydrogen is incorporated in the deposit as compared to the polycrystalline substrate. Furthermore, due to the open dendritic structure hydrogen formed by decomposition of hydrides can leave the deposit more quickly leading to the contraction of the lattice and thus to tensile stress [124]. Therefore, the open foam structure shows a reduction and even a change of the sign of the internal stress that improves the mechanical stability of the dendritic deposit and its adhesion to the substrate.

Hydrogen evolution causes gas bubble stirring that changes the hydrodynamics and the mass transfer conditions in the near-electrode electrolyte layer [85]. This leads to the formation of a large amount of nuclei due to the numerous nucleation sites on the polycrystalline Cu substrate. These nuclei determine the following deposition process. The CoNi deposition is performed under conditions of slow diffusion of the cations from the solution to the cathode where a fast electroreduction occurs.

5.3.7 Enhanced catalytic ability of open, dendritic structure deposited on single-crystalline Cu (111) substrate

Further investigation of the influence of the microstructure and morphology on the catalytic activity has been conducted on polished, rough and open, dendritic deposits. The deposit obtained on PC (cross-sectional image in Fig. 5.3b) was polished to about 500 nm thickness to provide a smooth reference sample (Fig. 5.6a insert). Figure 5.6) shows cyclic voltammograms recorded on CoNi deposits of similar composition but significantly different morphology in 0.1 M KOH at pH=12, that have been used to compare the

Substrate, thickness of deposit	Relative phase content (wt.%)		Co average grain size (nm)	CoNi macrostresses	
	HCP	FCC		σ_{11} (GPa)	σ_{33} (GPa)
polycrystalline Cu, 30 μm	93	7	14	-1.85	-0.89
single-crystalline Cu, 45 μm	80	20	9	0.74	0.43

Table 5.1: $\text{Co}_{90}\text{Ni}_{10}$ electrodeposits on different substrates. Results of the XRD measurements: content of HCP and FCC nanograins in solid solution of CoNi; for the Co (HCP) nanograins grain size and the values of the internal stresses are given (compressive stresses are indicated by a negative sign, tensile stresses are positive).

catalytic activity (Fig. 5.6). The peaks in the anodic region at 380 mV vs. Ag/AgCl for both rough and dendritic deposits (Fig. 5.6b and c) that precede the oxygen evolution reaction are attributed mainly to oxidation of the Ni and Co oxide/hydroxide compounds. The cathodic reduction peaks at 180 mV vs. Ag/AgCl are attributed to reverse processes.

A comparison of the surface charge density obtained by integration of the oxidation peaks revealed the values of 3 C cm^{-2} for the open dendritic CoNi deposit and 2 C cm^{-2} for the rough CoNi deposit. No peak is visible in the case of the polished CoNi deposit. Redox processes are conducted at higher rate at the CoNi dendritic deposit obtained on the SC substrate. This can be attributed to a higher surface area of the open, porous structure. Therefore, the morphology of the porous layer structure has a decisive influence on kinetics of the surface redox reaction suitable for both, batteries and the catalytic activity for oxygen evolution in electrolyzers. The porous CoNi layer obtained on SC exhibits a superior electrochemical performance as compared to the rough deposits and especially to the polished deposits, where no peaks attributed to any electrochemical process can be noticed in spite of the similarity in structure of all three deposits. It is important to emphasize that the processes presented in Fig. 5.6b and c are reversible, and have a great potential to be used as positive material in alkaline batteries.

5.3.8 Conclusions

CoNi layers were electrodeposited on Cu substrates with different surface structures. It is shown that the morphology, microstructure, internal stress

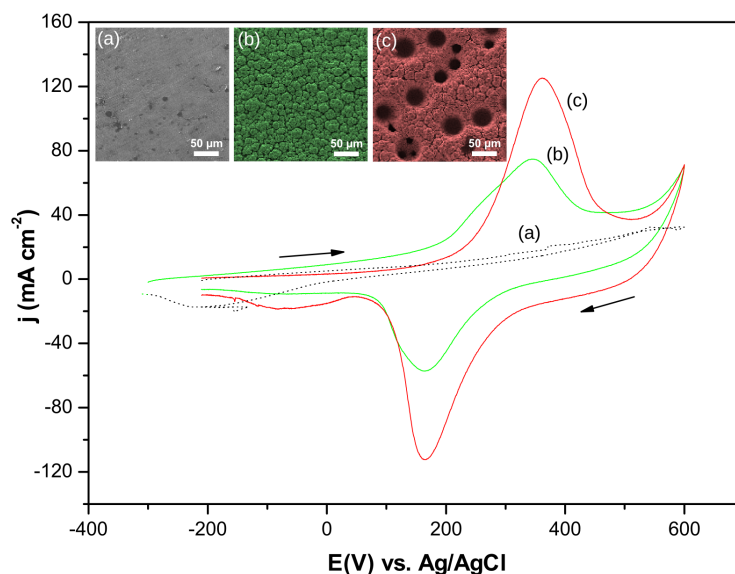


Figure 5.6: Cyclic voltammograms recorded in 0.1 M KOH with CoNi deposits obtained on (a) polished CoNi deposit, (b) rough deposit on PC and (c) open dendritic deposit on SC substrate (presented as inserts) showing enhanced peaks on SC substrate attributed to high surface area of open, dendritic structure. Scan rate 50 mV s^{-1} .

and catalytic ability of the layers are strongly influenced by the structure of the substrate.

By the use of a specially chosen single-crystalline (111) Cu substrate we achieved a uniform deposition of an open, dendritic foam structure at a low current density by providing uniformly distributed but distinct active sites for epitaxial growth and hydrogen bubble formation at the very beginning of deposition. The low wettability of the bare electropolished single crystalline Cu substrate with a minimum density of surface steps and a low surface energy assists the adhesion of large coalescing hydrogen bubbles on the substrate. The localized flow of metal ions due to hydrogen bubbles leads to localized growth of the CoNi deposit in the form of dendrites composed of fine platelets. The resulting nanostructured CoNi alloy foam with nanosized grains shows a low level of tensile stress.

In contrast, the electrodeposit on polycrystalline Cu at the same current density forms a dense nanocrystalline CoNi layer with a large compressive stress.

The presented approach allows depositing open structures at relatively

low current densities that are well attached to the surface and have a good mechanical stability. This makes the foam suitable for various applications. CoNi alloy foams with high surface area have promising applications in the fields of electrocatalysis, sensors, fuel cells, batteries and supercapacitors.

Chapter 6

A hierarchical nanodendritic NiCoFe alloy structures ¹

6.1 Introduction

The production of nanostructured iron-group alloys (Ni, Co, Fe) by electrodeposition has attracted considerable interest due to their outstanding magnetic and thermophysical properties, e.g. NiFe alloys can be used for magnetic memories [125]. NiCoFe ternary alloys have been reported to show improved properties for recording devices as compared to NiFe [18, 126]. Furthermore, their low thermal expansion allows commercial applications as high temperature alloys [127]. Considerable work has been done in the field of iron group thin films [94], but a systematic study on electrodeposition of NiCoFe alloy powders is still lacking despite the wide range of potential applications. The relatively new electrochemical technique, the hydrogen co-evolution process for electrodeposition of size dependent nickel nanoparticles [128], is an interesting addition to the currently used production techniques, which are based on mechanical processing, chemical reactions or liquid metal atomization, because electrolytic metal powder production usually yields product of high purity with controlled morphology under moderate physical conditions. Powder consolidation and sintering of NiCoFe powders electrodeposited from aqueous solutions could be scaled up and would thereby offer a promising route for their application [129]. Additionally, electrodeposition at high current density represents an excellent method for production of high

¹Based on a submitted article

surface area deposits. Different processing parameters can change the crystallite and particle size of deposits, type of crystalline phases and chemical composition, which can significantly alter the physical or chemical properties. Recently, attention has been paid to the production of nanoporous materials [84] with nanoramified dendritic walls suitable for application in electrochemical devices (e.g. catalysts, fuel cells, sensors or batteries) [100, 130].

The aim of this investigation is the synthesis and characterization of electrodeposited NiCoFe alloy powders and high surface area deposits, that are dendritic over several length scales (from 100 μm particles down to 10 nm branches). The possibility to use the electrodeposited alloys as catalysts is explored. A systematic study of the influence of the deposition process on the composition, phase, nanostructure, size and morphology of the electrochemically obtained particles is carried out using a combination of methods: scanning electron microscopy (SEM), transmission electron microscopy (TEM) and X-ray diffraction analysis (XRD) are used amongst other methods to characterize the structure on the micro and nanoscale.

6.2 Experimental Procedure

It was attempted to electrodeposit ternary alloy dendritic structures on polycrystalline Ti cathodes by constant current application through an ammonium sulfate-chloride solution at a current density from 0.1 to 1 A cm^{-2} , at room temperature without stirring, using a Jaissle potentiostat, IMP 83 PC-10. Both, powders and layers were obtained in an open glass electrochemical cell with a volume of 1.0 dm^3 . For the production of powders, a Ti plate placed roughly in the center of the cell with 1.0 cm^2 surface area and 0.2 cm thickness was used as the working electrode; flat electrolytic Ni electrodes with a 10 cm^2 surface area, placed at a distance of 2 cm from and aligned parallel to the Ti plate, were used as anodes. Dendritic layers were electrodeposited on a Ti rod with a surface area of 0.031 cm^2 and using a Ti / RuO_2 , TiO_2 anode. The electrolyte solutions were made from analytical grade chemicals (Sigma-Aldrich) and high purity water. The ternary NiCoFe powdery and dendritic structures were electrodeposited from solutions containing 0.09 M NiSO_4 + 0.03 M FeSO_4 + 0.053 M CoSO_4 + 0.4 M H_3BO_3 + 0.28 M NH_4Cl , at pH=2 adjusted with HCl [131]. The powder was removed after 180 and 1800 s using a brush and the solution was discarded and re-

placed with fresh electrolyte after 2 h of electrolysis to prevent significant change in composition. All samples were carefully treated to prevent oxidation due to the high surface area exposed to oxygen and moisture from the air [132]. It should be noted that oxidation of the deposit is most likely to occur during washing and drying steps, not during electrodeposition in acidic electrolytes [132]. However, acids can promote oxidation during drying. Therefore, initial washing consisted of repeated rinsing with large amount of high purity water. Secondly, stabilization was attempted with a colloidal substance (0.1 % benzoic acid solution), followed by washing and finally, drying in a tube furnace under vacuum at 100 °C for 1 hour.

The determination of the phase content and the crystallite size was conducted by X-ray diffraction on a X'Pert Powder diffractometer from PANalytical (CuK α 40 kV and 30 mA) in Bragg-Brentano geometry. The measurements were performed in step-scan mode over the range $\theta = 20 - 110^\circ$ with a step size of 0.05° and a counting time of 10 s/step. Evaluation of the phase volume and crystallite size was done by Rietveld refinement [88] using the TOPAS software.

The particle size distribution of the NiCoFe alloy powder was determined by a method which combines photometric gravitation and centrifugal sedimentation based on Stoke's law. The change in concentration of the suspension was detected by optical means at a fixed distance from the uppermost surface and the time measured from the commencement of the sedimentation. The photometric detection method determines the particle size by measuring the change of concentration of the sample in a suspension after a known elapsed time at a constant sedimentation distance (the distance from the liquid surface). The centrifugal sedimentation method uses the centrifugal force to accelerate the sedimentation rate allowing measurement of particles which have a slow speed of sedimentation or lift. Typically these are fine particles, or particles differing only slightly in specific gravity from the dispersant. The measurements of powder particle size were done using the particle size analyzer, Shimadzu, SA-CP4 in a glycerine based solution.

Zeta potential measurements were carried out at room temperature (298 K) in electrolytes used for preparation of ternary powders using an electroacoustic spectrometer DT-1200 (Dispersion Technology Inc.). The quoted zeta potential value are averages of 3 measurements.

The morphology was analyzed with a SEM equipped with a field emission

gun (XL 30 ESEM-FEG, FEI). The profile and roughness measurements, as well as 3D area analysis directly from the stereoscopic images of the specimen surface were carried out using MeX software from Alicona (A). For characterization on the nanoscale, TEM investigations were carried out using a Philips CM200 microscope operating at an acceleration voltage of 200 kV.

6.2.1 Electrochemical characterization of NiCoFe alloy deposits

A characteristic of the iron group metals (Ni, Co and Fe) and their alloys is that electrodeposition from aqueous electrolyte is typically accompanied by intensive hydrogen evolution, due to their negative standard electrode potentials relative to hydrogen [82, 99, 85]. However, dendritic deposition occurs via a mass-transfer controlled electrochemical process which is enhanced at high current densities and hydrogen gas production rate increases monotonically with current density. Also, cell resistance increases when gas partially blocks the electrodes. Therefore, for the electrochemical characterization, it is necessary to correct all polarization measurements for the IR drop in the electrolyte during the process [82, 99].

In order to obtain information on the electrochemical behaviour of the NiCoFe alloy, polarization curves were obtained for the single metals Ni, Co and Fe at the same concentration of the respective metal ions alone in the solution as compared to ternary alloy deposition. The polarization measurements were carried out by a computer controlled electrochemical system (PAR M 273A, software PAR M352/252, version 2.01) with a sweep rate of 1 mV s^{-1} . For the correction of the IR drop, a current interrupt technique was used with a time of current interruption of 0.5 s[82]. The polarization curves were measured in a three-electrode, three-compartment electrochemical cell at $(298 \pm 1) \text{ K}$. A Luggin capillary connecting the saturated calomel reference electrode (SCE) to the electrolyte was positioned at a distance of 0.2 cm from the working electrode. The working electrode was a Ti rod embedded in resin ($d = 4 \text{ mm}$). Electrochemical characterization of a NiCoFe electrode was done employing linear sweep voltammetry (LSV) at a scan rate of 10 mVs^{-1} . A Pt-mesh with high surface was used as a counter electrode. A blank LSV test was obtained in aqueous 0.1 M Na_2SO_4 solution at pH=3, adjusted by addition of HCl. To examine the electroreduction of

nitrate 0.01 M NaNO_3 was added to the solution.

6.3 Results and discussions

6.3.1 Polarization diagrams for the deposition of dendritic Ni, Co and Fe metals and NiCoFe alloys

The standard redox potentials of Ni^{2+} , Co^{2+} , Fe^{2+} and H^+ are -0.52, -0.53, -0.68 and -0.24 V vs. SCE, respectively. These values should be taken for rough comparison only, because the activities of the ions during electrolysis were not well defined. However, it may be safely assumed that hydrogen evolution would accompany metal deposition in all cases. Linear sweep voltammograms (Fig. 6.1) of electrolytes containing one type of metal ion (Fe, Ni or Co) exhibited some similarities. Specifically, below -0.6 V vs. SCE the potential showed a region (i) of rather linear dependence on the logarithm of the current density up to a limiting current density of about $10^{-3.5}$ to $10^{-2.5}$ A cm^{-2} . Then followed a region (ii) where the potential changed little with current density until a limiting current density of about $10^{-0.5}$ A cm^{-2} was reached. Thereafter, in region (iii) the potential increased greatly with current density. Region (i) is explained as mixed electron transfer and diffusion control of the metal reduction reaction coinciding with limited hydrogen evolution. Within this region Fe and Co showed at least one inflexion in the polarization diagram, which may be due to a surface phase formation with the Ti. Region (ii) is indicative of significant hydrogen evolution, up to a diffusion limit at around $10^{-0.5}$ A cm^{-2} . The expected Tafel slopes of -1/120 mV [25] are not observed due to the IR correction technique. However, the relative overpotentials for the hydrogen evolution reaction, after IR correction, at this pH, may be seen to increase from $\text{Co} < \text{Fe} < \text{Ni}$ at around 0.1 A cm^{-2} . In region (iii) both metal deposition and hydrogen evolution are under diffusion control. This is the region where electrodeposits were rough and powdery.

6.3.2 Nanofabrication of high surface area NiCoFe deposits

As can be seen from LSV of the electrolyte containing all three metal ions (Fig. 6.1), a current density of 0.1 A cm^{-2} represents the border between region (ii)/(iii) with mixed electron transfer and diffusion control of the metal

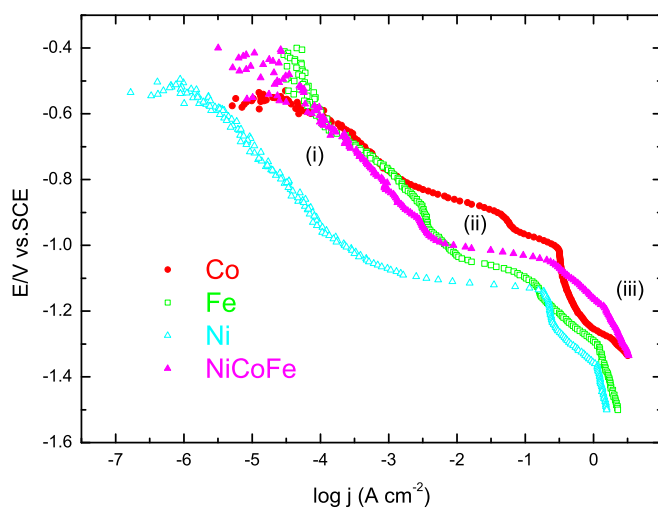


Figure 6.1: Linear sweep voltammograms for the electrodeposition of non-dendritic and dendritic nanostructures: Ni (\triangle), Co (\bullet) and Fe (\square) from the solution containing 0.09 M NiSO_4 for pure Ni ; 0.09 M FeSO_4 for pure Fe and 0.09 M CoSO_4 for pure Co; 0.09 M NiSO_4 + 0.053 M CoSO_4 + 0.03 M FeSO_4 for \blacktriangle -NiCoFe alloy. All solutions were mixed with 0.4 M H_3BO_3 + 0.28 M NH_4Cl . All curves were measured with an IR drop correction.

deposition. After 180 s at this current density a smooth deposit of non-dendritic NiCoFe alloy was formed. The surface of the deposit is shown in Fig. 6.2a. For comparison a further sample was prepared at 0.1 A cm^{-2} but with the same amount of charge passed as for the sample obtained at 1 A cm^{-2} for 180 s (i.e. 0.1 A cm^{-2} 1800 s deposition time). This sample (Fig. 6.2b) closely resembled the sample deposited at 0.1 A cm^{-2} for 180 s (Fig. 6.2a) on a microscopic level, although stresses within the deposit had caused the dense $10 \text{ }\mu\text{m}$ thick layers to partially split and delaminate from the titanium substrate.

In contrast at 1 A cm^{-2} (for 180 s) a 3D dendritic structure with open pores was obtained (Fig. 6.2c). The pores are a consequence of the vigorous hydrogen gas evolution and the microstructure from the diffusion-limited metal deposition. It was found that 180 s was an optimal deposition time, because longer deposition tended to give rise to fragile dendrites that were liable to become disconnected in the cell, due to the gas evolution.

In addition to the morphology, the composition depends also on the current density (i.e. the applied overpotential) in the region of intensive hydrogen evolution (i.e. region (ii) in Fig. 6.1). Namely, at a current density of 0.1 A cm^{-2} , the composition of the obtained deposit was 20 at.% Ni, 45 at.% Co and 35 at.% Fe; indicating an anomalous codeposition of the iron group elements [117] where the less noble metal is deposited preferentially to the more noble one. From thermodynamic considerations, Ni, the most noble metal of the three, would be expected to deposit preferentially to both Co and Fe during alloy deposition, if the kinetics of each metal deposition reaction were comparable. However, the deposition of Ni is inhibited by the deposition of Co and/or Fe. Figure 6.3 shows the XRD of a non-dendritic (0.1 A cm^{-2} , 180 s) and dendritic (1 A cm^{-2} , 180 s) deposit. The XRD reveals the formation of a (Ni,Co)Fe solid solution with BCC structure corresponding to that expected from the phase diagram for the given composition ($\text{Ni}_{20}\text{Co}_{45}\text{Fe}_{35}$) [133]. Reflections arising from the Ti substrate are strong due to very thin NiCoFe deposit of around $1 \text{ }\mu\text{m}$. On the other hand, the dendritic deposit (Fig. 6.3b) shows FCC structure in accordance with a significantly different composition obtained at the higher current density ($\text{Ni}_{50}\text{Co}_{30}\text{Fe}_{20}$). It is interesting to note that the crystallite size of the deposit was 6.5 nm. This can be correlated with the LSV (Fig. 6.1) where deposition at a current density of 0.1 A cm^{-2} belongs to the region (ii) with little dependence of overpo-

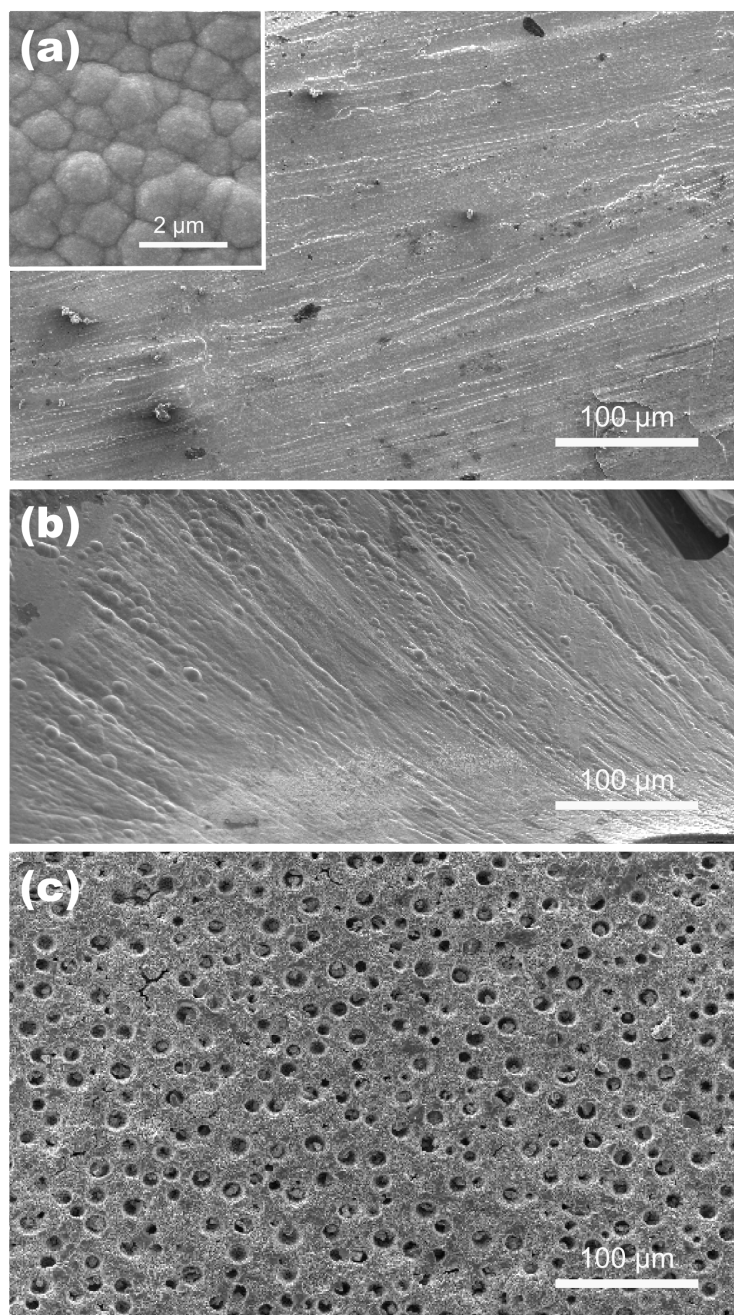


Figure 6.2: SEM images of NiCoFe alloys obtained at different current densities: (a) Non-dendritic deposit obtained at $j=0.1 \text{ A cm}^{-2}$ for 180 s characterized by a smooth cauliflower morphology consisting of fine particles as shown in the insert, (b) Non-dendritic deposit obtained at the same charge passed as in (a), i.e. $j= 0.1 \text{ A cm}^{-2}$ for 1800 s and (c) Dendritic deposit obtained at $j= 1 \text{ A cm}^{-2}$ showing a 3D dendritic morphology formed during an intensive hydrogen evolution reaction.

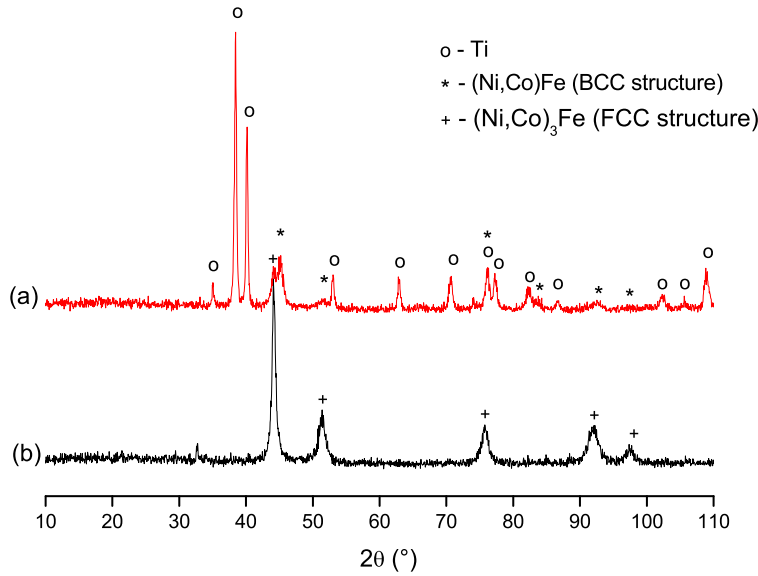


Figure 6.3: X-ray profile of the NiCoFe non-dendritic deposit obtained at a deposition time of 180 s on a Ti substrate at: (a) a current density of $j = 0.1 \text{ A cm}^{-2}$, showing broad peaks corresponding to the nanocrystalline BCC structure of the $\text{Ni}_{20}\text{Co}_{45}\text{Fe}_{35}$ deposit and sharp peaks corresponding to the Ti substrate and (b) NiCoFe dendritic deposit obtained at a current density of $j = 1 \text{ A cm}^{-2}$, showing broad peaks corresponding to the nanocrystalline FCC structure of the $\text{Ni}_{50}\text{Co}_{30}\text{Fe}_{20}$ deposit.

tential on current. Since from the nucleation theory, the crystallite size is mainly affected by the increase of overpotential [38], the crystallite size is not changed after reaching the plateau in the polarization diagram.

With a further increase of the current density, the increase of the overpotential is connected with an increasingly intensive hydrogen bubble evolution. Intensive hydrogen evolution causes gas stirring, changing the mass transfer conditions in the double layer and hence the local electrolyte composition at the electrode surface. Under pure diffusion control the composition of the deposit should be determined by the composition of the electrolyte. Dendritic deposits are formed under the diffusion control conditions, i.e. high current density. At potentials more negative than -1.2 V vs. SCE at a current density of $j \geq 1 \text{ A cm}^{-2}$, the deposition process is under complete diffusion control. Figure 6.4 shows a detailed 3D SEM reconstruction of the dendritic NiCoFe alloy surface obtained under such deposition conditions. Pronounced circular depressions ca. $20 \mu\text{m}$ diameter (a roughness profile is

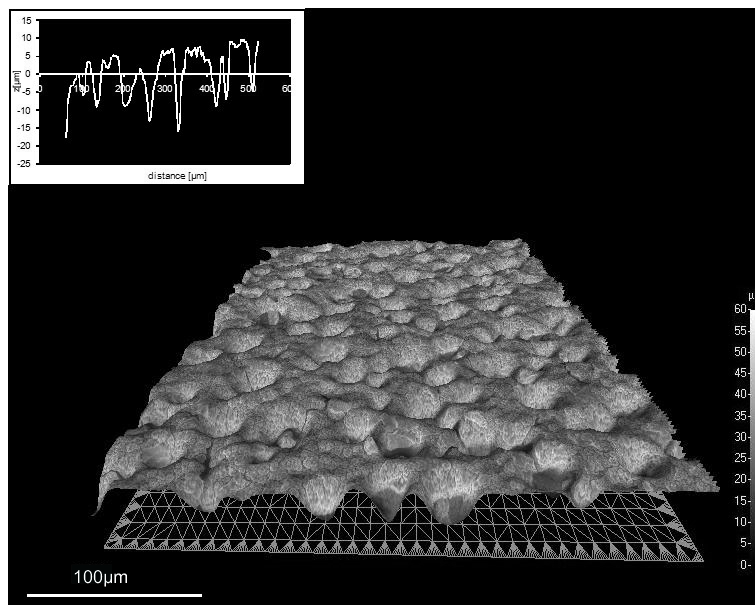


Figure 6.4: 3D SEM reconstruction of the NiCoFe surface showing the distribution of pores formed during hydrogen codeposition at a current density of $j = 1 \text{ A cm}^{-2}$; A roughness profile across the NiCoFe surface is shown as an insert.

shown as an insert in Fig. 6.4 in addition to smaller scale roughness were observed). Uniformly distributed pores are created by hydrogen bubbles during intensive hydrogen evolution reaction yielding deposit thickness of a 20 μm . Hierarchical structures with features ranging from nm to tens of μm were thus deposited in a single-pot, template-free, room temperature process.

6.3.3 Nanodendritic NiCoFe alloy as catalysts

A big challenge over recent years is to convert nitrate into harmless nitrogen [134] or ammonia e.g. $\text{NO}_3^- + 8\text{e}^- + 9\text{H}^+ \rightarrow 3\text{H}_2\text{O} + \text{NH}_3$ [130] with emphasis on the selection of an appropriate catalyst with a good performance for an effective electroreduction reaction in aqueous solution. Linear sweep voltammetry was employed for the investigation of the electroreduction of nitrate in $0.1 \text{ M Na}_2\text{SO}_4$ solution. A sulfate solution with and without addition of 0.01 M NaNO_3 was investigated for nanodendritic (1 A cm^{-2} , 180 s) and non-dendritic (0.1 A cm^{-2} , 180 and 1800 s) NiCoFe electrodes (Fig. 6.5). Typically catalytic activity of solid-phase catalysts increases with surface area. Clearly visible reduction peaks of NO_3^- at ca. -900 mV vs. SCE can be

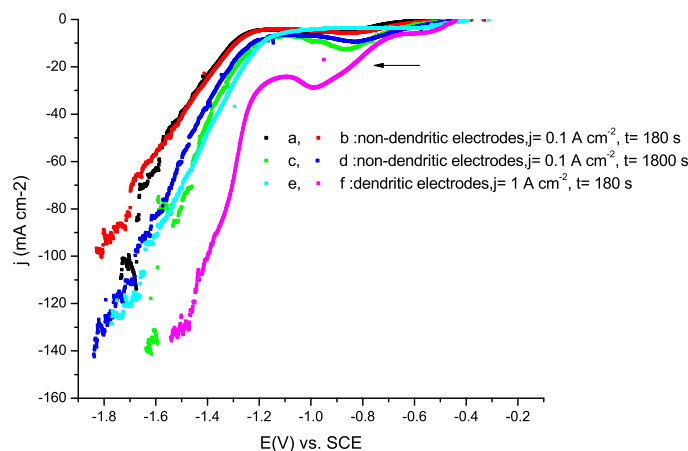


Figure 6.5: Linear sweep voltammograms on different NiCoFe deposits: (a), (c) non-dendritic and (e) nanodendritic electrodes recorded in blank 0.1 M Na_2SO_4 solution and on (b), (d) non-dendritic and (f) nanodendritic electrodes in aqueous solution containing 0.01 M NaNO_3 . Scan rate of 10 mVs^{-1} .

attributed to the high surface area of the nanodendritic NiCoFe electrode described in the previous section because the non-dendritic electrodes showed no significant features attributed to NO_3^- reduction. The nitrate reduction ability of the nanodendritic electrode is greatly enhanced over the dendritic deposit, which may reasonably be attributed to the high surface area of the modified electrode. The nanodendritic NiCoFe electrode, prepared under extreme hydrogen evolution providing conditions for nanodendritic growth and mechanical stability in a short electrolysis time, is a suitable candidate material for further study as a catalyst for the electroreduction of nitrate.

6.3.4 Deposition of micro and nanoscaled metal alloy NiCoFe powders

An electrosynthesized metal powder represents a dendritic or disperse deposit which can spontaneously fall off or can be removed from the electrode by tapping or in a similar way [38]. Here we show that under similar experimental conditions it is possible to electrodeposit ternary alloy powders and to tailor their particle size from the microscale down to the nanoscale.

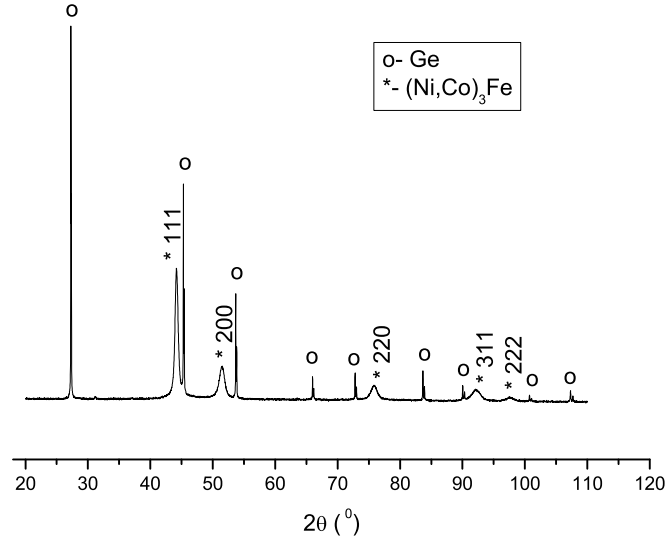


Figure 6.6: X-ray profile of the electrodeposited NiCoFe powder obtained at a current density of $j = 1 \text{ A cm}^{-2}$ and removed after 180 s showing broad peaks corresponding to the nanocrystalline NiCoFe powder and sharp peaks corresponding to the Ge standard, that was added to allow a precise determination of the lattice constant.

6.3.5 Structural characterization of the electrodeposited ternary NiCoFe alloy powders

The chemical composition of the ternary NiCoFe alloy powders obtained at a current density of $j = 1 \text{ A cm}^{-2}$ and removed after a time of 180 s was determined by Energy-dispersive X-ray spectroscopy showing that the powder composition was $\text{Ni}_{50}\text{Co}_{30}\text{Fe}_{20}$ significantly different to the composition at 0.1 A cm^{-2} and better reflecting the metal salt concentrations in the bulk electrolyte. According to the ternary NiCoFe phase diagram [133], this composition is in the range where a FCC crystal structure corresponding to a $(\text{Ni, Co})_3\text{Fe}$ solid solution is formed. The XRD measurements (Fig. 6.6) confirm the presence of a FCC phase only. No peaks related to the oxides are present. For the determination of a precise lattice constant, Ge powder was added as a standard to the powder sample, showing that the FCC $(\text{Ni, Co})_3\text{Fe}$ solid solution has a lattice constant of $a = 3.5543 \text{ \AA}$.

The presence of broad peaks corresponding to the $\text{Ni}_{50}\text{Co}_{30}\text{Fe}_{20}$ alloy

powder (Fig. 6.6) indicates that the ternary powder consists of nanosized crystallites. A detailed crystallite size determination was performed using a double-Voigt approach implemented in Topas software. For the calculation all peaks were included and the instrumental broadening was taken into account. The calculations show that the NiCoFe alloy powder has an area weighted mean crystallite size of 7.4 nm. The presence of FCC structure in the ternary alloy powder was determined in the powder obtained at a current density of $j = 1 \text{ A cm}^{-2}$. As for the composition, the crystallite size was shown not to be affected by the time of powder removal (from 180-1800 s).

6.3.6 Morphology and size of the powder particles

Two different techniques, SEM imaging and gravitation/sedimentation methods were employed to determine the particle size of the electrodeposited NiCoFe powders. Figure 6.7 shows SEM images of typical alloy powder particles. The particles exhibited a highly branched three-dimensional morphology that can be clearly seen in Fig. 6.7a, showing particles as large as $100 \mu\text{m}$. With increasing time of powder production, the particle size of the NiCoFe alloy powder increased (Fig. 6.7) showing the particles with dimensions larger than $100 \mu\text{m}$ after 1800 s at 1 A cm^{-2} . Increasing the deposition time led to further dendritic growth with more pronounced high order branches.

For a quantification of the particle size distribution, the sedimentation method was used to determine the size of the finer powder obtained after deposition for 180 s at a current density of 1 A cm^{-2} . The mean powder size was found to be ca. $10 \mu\text{m}$ (Fig. 6.8).

By this method it was also possible to determine the specific surface area of the NiCoFe powder sample resulting in values of 94 and $75 \text{ m}^2 \text{ g}^{-1}$ for the particles electrodeposited at 180 s and 1800 s, respectively. It should be pointed out that this value was calculated assuming dense particles, and therefore does not take into account the fine substructures of the particles. This means that in addition to the rather large specific surface area of the particles the dendritic morphology gives rise to an additional surface that is orders of magnitude larger, making the powder interesting for catalytic applications.

For both powder samples obtained after 180 s and 1800 s the measured

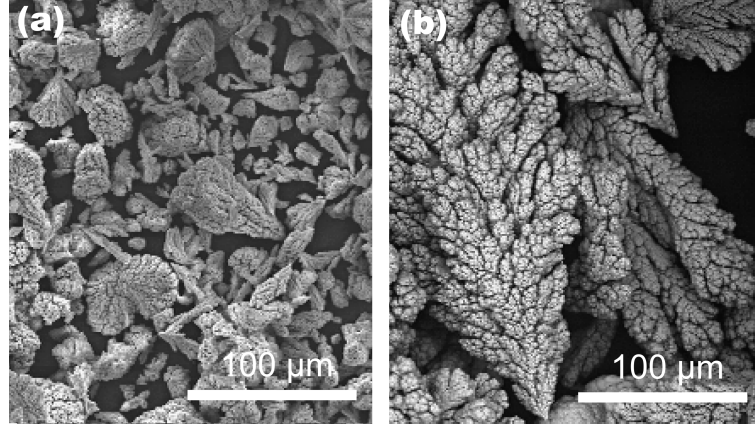


Figure 6.7: SEM images of NiCoFe powder deposited at $j= 1 \text{ A cm}^{-2}$ after (a) 180 s and (b) 1800 s deposition time. The images show that by increasing the deposition time the particle size increases. The particles show a 3D dendritic morphology.

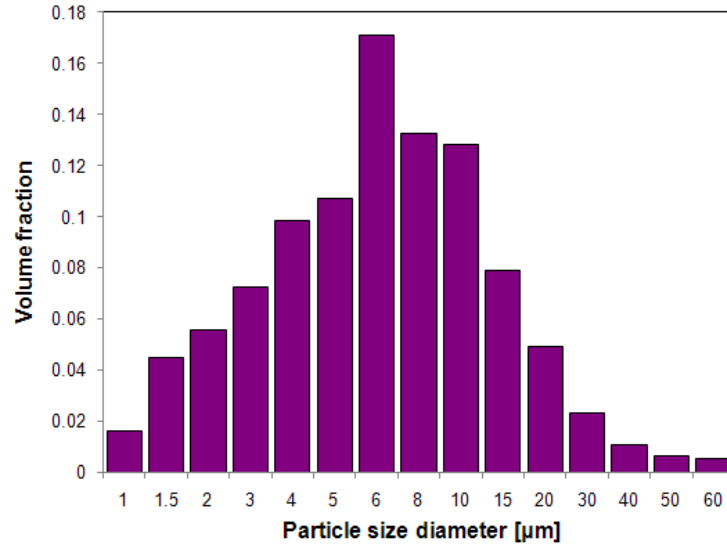


Figure 6.8: Particle size distribution of NiCoFe alloy powder ($j=1 \text{ A cm}^{-2}$, deposition time, $t=180 \text{ s}$) measured by the sedimentation method. The distribution shows a mean of $10 \mu\text{m}$.

zeta potentials were similar, specifically $\xi = +(20 \pm 2)$ mV at pH= 2 in the electrolyte used for preparation of dendritic structures. The magnitude of ξ gives an indication of the stability of a colloidal suspension [135]. The value found here is typical of metastable suspensions where the electrostatic repulsion between particles is barely sufficient to compensate for the Van der Waals attraction. That both samples have similar values of ξ reflects the similar surface chemistry.

6.3.7 Grain size of electrodeposited ternary NiCoFe alloy powders

Figure 6.9 shows TEM images of the NiCoFe powder deposited at a current density of 1 A cm^{-2} for 180 s. The TEM bright-field image (Fig. 6.9a) reveals that the particles are dendritic on a nanoscale. From the SEM studies (Fig. 6.7) particles as large as $100 \mu\text{m}$ containing fine branches of ca. $1 \mu\text{m}$ were visible. Using the higher magnification available with TEM it was revealed that the branches are structured on length scales down to < 50 nm. Figures 6.9a and c show a TEM bright-field and the corresponding dark-field image taken at a higher magnification. The very fine branches consist of a nanograined structure with grains even smaller than 10 nm in agreement with XRD measurement of the crystallite sizes (Fig. 6.6). The corresponding selected area electron diffraction pattern taken from an area of $1.13 \mu\text{m}^2$ is shown in the inset in Fig. 6.9a. An evaluation of the diffraction pattern using the PASAD software [136] reveals that the NiCoFe powder is FCC structured with a lattice parameter of $a = 3.55 \text{ \AA}$ which is also in good agreement with the results from XRD.

TEM dark field images were used to determine a grain size histogram. More than 500 grains were evaluated by digital imaging processing. The resulting histogram shown in Fig. 6.10 reveals the presence of very fine nanograins with a mean of 5.3 nm and an area weighted mean of 7.9 nm. This result is in good accordance with the results obtained by XRD giving a mean area weighted crystallite size of 7.4 nm. This suggests that the dendrites consist of very small nanograins that do not contain many defects or subgrain boundaries.

Dendritic structures typically form under diffusion limiting conditions away from the thermodynamic equilibrium [137]. A model known as a diffusion limited aggregation is adopted to interpret different systems controlled

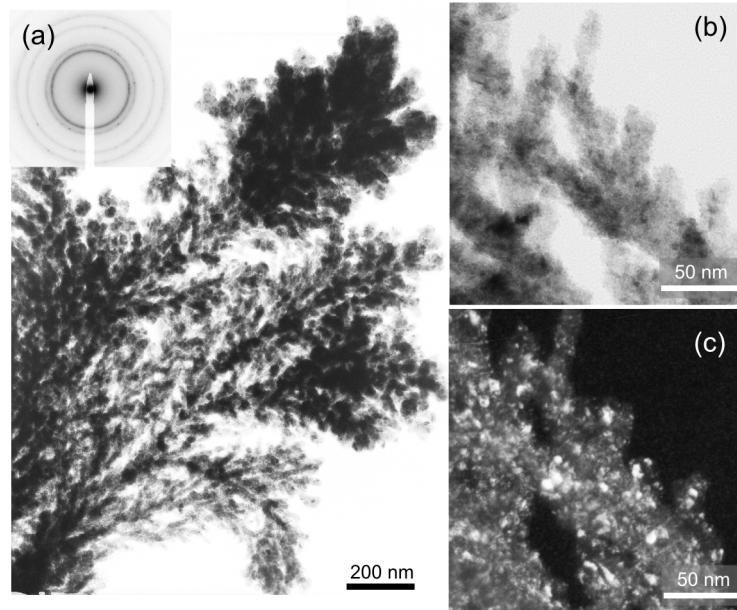


Figure 6.9: Transmission Electron Microscopy (TEM) study of the NiCoFe powder ($j=1 \text{ A cm}^{-2}$, deposition time, $t=180 \text{ s}$). (a) TEM bright-field image revealing a highly branched dendritic structure. The dendrites are very fine with branches down to less than 50 nm . The corresponding diffraction pattern shown as insert reveals a FCC structure in agreement with XRD. (b+c) The TEM bright and dark field images taken at a higher magnification show that the branches consist of a nanograined structure with grains smaller than 10 nm .

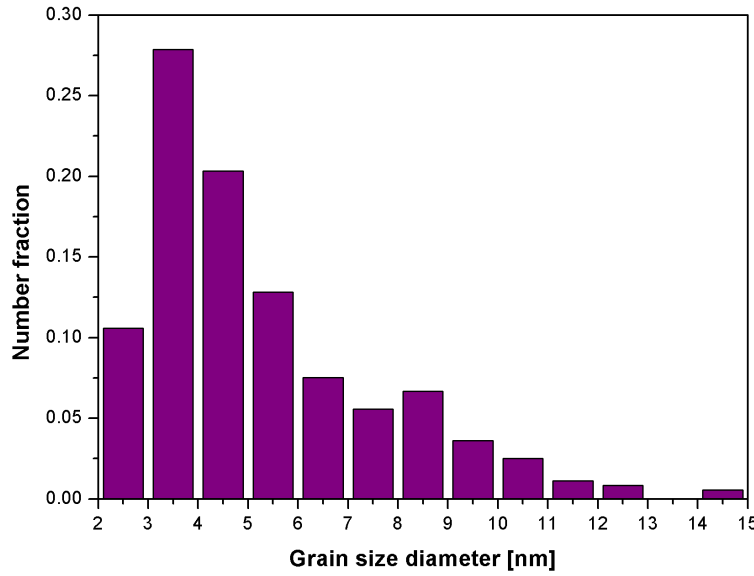


Figure 6.10: Grain size distribution of the NiCoFe powder ($j=1 \text{ A cm}^{-2}$, deposition time=180 s), determined by counting of grains from TEM dark field images. The distribution shows a mean of 5.3 nm and an area weighted mean of 7.9 nm.

by diffusion process [138]. The resulting surfaces may be characterized by the Hausdorff fractal dimensions, D_f , that may be determined by digitizing photographs and taking the best-fit slope of $\ln(N)$ vs. $\ln(r)$, where $N(r)$ is the number of pixels covering the fractal [44]. Therefore, a non-fractal planar boundary (e.g. circle) would have $D_f=1$, whereas a highly fractal boundary such as that of the Mandelbrot set has $D_f=2$ [139]. In practice Zn dendrites have been found to exhibit D_f up to 1.85 depending on the current density [44] and natural ferns ca. 1.826 [137]. A TEM image (Fig. 6.9a) of the dendritic NiCoFe structure was saved as black and white bitmap file for the program used for the calculation of the fractal dimension. Using the Fractalyse (ver. 2.4) fractal analysis software [140] the dendritic NiCoFe powder deposited at 1 A cm^{-2} was calculated to have a D_f of 1.77 similar to the one observed for natural fern [137].

Therefore, from TEM and SEM investigations it can be concluded that the electrochemically obtained ternary NiCoFe alloy powder shows a highly hierarchical structure suitable for practical application. The particles have a dendritic structure that is highly branched on several length scales and the branches themselves consists of nanograins smaller than 10 nm.

6.4 Conclusions

NiCoFe deposits obtained at a high current density of 1 A cm^{-2} under strong hydrogen evolution show a 3D dendritic morphology with a composition of 50 at.% Ni, 30 at.% Co and 20 at.% Fe and a FCC structure. The anomalous codepositon at lower current densities (0.1 A cm^{-2}), results in a significant change of the morphology and composition i.e. the formation of a non-dendritic NiCoFe deposit with an overall composition of 20 at.% Ni, 45 at.% Co and 35 at.% Fe and a BCC structure. The crystallite size of the obtained deposits is not affected by the current density applied due to the similar overpotential during electrodeposition at different current densities.

SEM and TEM methods show that the powder particles obtained at high current density of 1 A cm^{-2} have a highly branched dendritic structure extending from the micrometer scale down to the nanoscale with sub-branches smaller than 50 nm. Therefore, it is possible to deposit nanodendritic NiCoFe powders and deposits with a high surface area that are of interest for catalytic applications. The particle size of the NiCoFe alloy powder increases both with increasing current density and increasing time of powder production. TEM dark field images show that the mean area weighted grain size of the nanodendritic branches is 7.9 nm, which is in good agreement with the mean crystallite size derived from X-ray studies (7.4 nm). This suggests that the dendrites consist of very small nanograins that do not contain many defects or subgrain boundaries.

The electroreduction of NO_3^- on both, the nanodendritic and non-dendritic deposits were compared showing that the nanodendritic NiCoFe deposits are suitable to be used as catalysts due to their extremely developed surface area. Nanoarchitecture of dendritic NiCoFe alloy structure resembling natural fern leaves can play an important role as advanced material for practical application.

Summary

The formation of dendritic structures or powders requires special electrodeposition conditions and it is enhanced by decreasing the concentration of depositing ions, increasing the concentration of the supporting electrolyte, increasing the viscosity of the solution, decreasing the temperature, and decreasing the velocity of motion of the solution. In other words, it is enhanced by all factors that increase the diffusion control of the deposition process. Therefore, the influence of the deposition parameters, i.e. current density or overpotentials and bath composition were chosen to synthesize and characterize microstructure, composition and electrochemical properties of the obtained deposits of iron group metals.

The microstructure as well as the morphology of the Ni-Co alloy deposits electrochemically obtained from an ammonium sulfate-chloride solution depends on the deposition current density and the bath composition. The galvanostatic electrodeposition from five different $\text{Ni}^{2+}/\text{Co}^{2+}$ concentration ratios in the electrolyte was performed at a selected current density of 65 mA cm^{-2} to determine the influence of the bath composition on the development of the dendritic structure on polycrystalline Cu substrates. The chemical composition of the deposited alloys has shown a dependence on the electrolyte composition, especially in the case of the alloy obtained at the lowest concentration ratio of ions in the electrolyte, i.e. $\text{Ni}^{2+}/\text{Co}^{2+} = 0.25$. The increased content of Co of 95% in comparison to the one theoretically expected from the electrolyte (80%) is an indication for an increase of the reaction rate of Co at a relatively low current density for the production of dendritic structures, i.e. 65 mA cm^{-2} in accordance with the term “anomalous codeposition” which refers to the preferential deposition of the less noble metal, i.e. Co. The X-ray diffraction analysis has shown the formation of the solid solutions of Ni and Co with progressive change depending on the chem-

ical composition of the electrolyte. As expected, the highest content of Co in the alloy deposit obtained from the electrolyte with $\text{Ni}^{2+}/\text{Co}^{2+} = 0.25$ leads to a single phase deposit with a HCP phase. On the other hand, the highest Ni content in the alloy deposit obtained from the electrolyte with the highest concentration ratio of Ni^{2+} to Co^{2+} used in this study, i.e. $\text{Ni}^{2+}/\text{Co}^{2+} = 4$, revealed the formation of a single phase FCC structure in the deposit. In the range of 30 - 40 at. % of Ni in the deposit, the mixture of cubic FCC and hexagonal HCP phase was formed in accordance to the phase diagram. The morphology of the Ni-Co deposits was significantly influenced by the composition of the electrolyte, from the typical cauliflower morphology observed for deposits with high Ni content to a platelet morphology for the deposit with higher Co content in the deposit. The increase of the HCP phase content in the nanocrystalline deposits appears as a result of both an increase in the Co^{2+} ions concentration in the bath and a decrease of the deposition current density. The average grain size in the deposits consisting of single FCC phase was around 13 nm in comparison with 20 nm grain size obtained in the single HCP phase deposit. The formation of the solid solution in the deposit led to further grain refinement of the deposit. The increase of the current density and the decrease of the Co^{2+} ions concentration in the bath resulted in finer grain deposits. The hardness progressively changed from the highest one (4 GPa) for the deposit with highest Co content in the alloy (i.e. the electrolyte with the concentration ratio $\text{Ni}^{2+}/\text{Co}^{2+} = 0.25$) to the value of about 1 GPa for the deposit with highest Ni content in the alloy (i.e. the electrolyte with the concentration ratio $\text{Ni}^{2+}/\text{Co}^{2+} = 4$). On the other hand, the change of the current density had no remarkable influence on the obtained hardness values. The hardness was mainly influenced by the formation of disperse and dendritic structures at higher current densities. The surface morphology and the mean roughness of the deposits depended on the concentration ratio in the electrolyte; in the case of equal ions concentration of $\text{Ni}^{2+}/\text{Co}^{2+}$ in the electrolyte, the mean roughness of the deposit was highest. Therefore, it was possible to achieve a variety of microstructural properties by choosing the current density or the electrolyte composition appropriately.

Further investigations were carried out to elucidate the influence of the parent metals, i.e. Ni and Co, as well as that of Ni-Co deposit (from electrolyte with $\text{Ni}^{2+}/\text{Co}^{2+} = 1$) conducted at different current densities (up to 400 mA cm^{-2}) on the process of the formation of the dendritic struc-

ture. It was shown that the structure of the deposits was governed by the nature of the depositing ions and the quantity of the evolved hydrogen. In the Co bath, the polarization measurements have shown a lower hydrogen overpotential and consequently a lower current efficiency. Generally, the evolution of hydrogen provided some additional stirring effect and enhanced the formation of a disperse deposit with more developed structures. At current densities $j \geq 400 \text{ mA cm}^{-2}$, the deposition became dependent on the hydrogen evolution, since it is the predominant reaction in the overall cathodic process. The SEM images have shown a gradual evolution of the dendritic formation with increasing current density. The dendrites obtained at the higher current density of 400 mA cm^{-2} have shown typical dendrite structures that have more pronounced secondary branches and high order branches. The comparison with the parent metals, i.e. Ni and Co, revealed that the dendritic growth occurred only in the particular case of Co deposition where the HCP lattice served as a growth site because the development of protrusions along some axis in the direction of increasing concentration was more favorable. The formation of dendritic Ni-Co alloy deposits was enhanced by increasing the current density but led to a decrease of the mean roughness. The surface roughness determined by 3D SEM reconstruction of the specimen surface gave the highest mean surface roughness, i.e. $\sigma = 4$ for Ni deposits. This was ascribed to the influence of H_2 bubbles attached during the codeposition with Ni causing the growth of the deposit before the bubbles are released. The composition of the alloy deposit is determined by the hydrodynamic conditions in the near electrode layer; with increasing current density, the evolution of the hydrogen is predominant, leading to a more uniform distribution of Ni and Co ions in the double layer, and, therefore, the composition of the deposits reaches the real value of the corresponding ions in the solution. The whole process determines the density of nucleation sites and the final morphology of the deposit. The grain size of the Ni-Co deposits is determined by the applied overpotential where the nucleation rate increases with the overpotential squared, resulting in a more rapid nucleation at a higher current density and in the formation of smaller crystals with average grain sizes of around 10 nm for alloy deposits obtained at the current density of a 400 mA cm^{-2} . At lower current density, i.e. 65 mA cm^{-2} the Co deposit has shown a larger grain size of about 45 nm in comparison to Ni deposit where the grain size was about 20 nm. Generally,

increasing current density results in finer grain deposits. The structure of the Ni-Co deposits is characterized by the formation of a solid solution; increasing current density results in an increase in the volume fraction of the cubic phase in nanocrystalline deposits. Amorphous phase content found by XRD evaluation is ascribed to the small grain size of the obtained nanocrystalline deposits and especially, to the formation of the disperse or in some case very dendritic deposits. The presence of an amorphous content is only possible by additional TEM investigation.

In addition, it was found that CoNi layers electrodeposited on different Cu substrates have shown different surface structures. The morphology, microstructure, internal stress and the catalytic ability of the layers were strongly influenced by the structure of the substrate.

By the use of a specially chosen single-crystalline (111) Cu substrate a uniform deposition of an open, dendritic foam structure at a low current density of 0.1 A cm^{-2} for deposition of disperse deposits was achieved. Uniform distribution but distinct active sites for epitaxial growth and hydrogen bubble formation at the very beginning of deposition provided conditions for the formation of open, porous foam structure on single crystalline Cu (111) substrate. The low wettability of the bare electropolished single crystalline Cu (111) substrate with a minimum density of surface steps assisted the adhesion of large coalescing hydrogen bubbles on the substrate. The localized flow of metal ions due to hydrogen bubbles led to localized growth of the CoNi deposit in the form of dendrites composed of fine platelets. The resulting nanostructured CoNi alloy foam with nanosized grains of about 9 nm shows a low level of tensile stress.

In contrast, the electrodeposit on polycrystalline Cu at the same current density formed a dense nanocrystalline CoNi layer with a large compressive stress, higher content of hexagonal HCP phase and average grain size of about 14 nm.

The presented approach allowed depositing open structures at relatively low current densities that were well attached to the surface and had a good mechanical stability. Tailoring of the morphology of the foam layers were possible to achieve using single crystalline Cu(111) substrate in ambient conditions. This made the foam suitable for various applications and enhanced catalytic ability of the foam was checked by comparison of relatively smooth CoNi layer, rough CoNi layer formed on polycrystalline Cu substrates and

foam like layer formed on single crystalline Cu (111) substrate. Redox processes with higher rate can be attributed to the high surface area of deposited foam on single crystalline Cu (111) substrate. The reversibility of the reaction conducted in KOH on high surface area foam gives great potential to be used as positive materials in alkaline batteries or catalysts for oxygen evolution in electrolyzers.

One additional aim of this work was electrodeposition of ternary NiCoFe powders that can be periodically removed from the substrate or stay on the substrate in form of highly developed surface area deposits. A single-pot, room-temperature electrosynthesis route to hierarchical nanodendritic layers and powders of NiCoFe ternary alloy was performed. For that purpose, electrodeposition at constant very high current density of 1 A cm^{-2} was conducted on Ti polycrystalline substrates for a different deposition time. NiCoFe deposits obtained at high current density of 1 A cm^{-2} under strong hydrogen evolution show a 3D open, dendritic morphology with a composition of 50 at.% Ni, 30 at.% Co and 20 at.% Fe and a FCC structure. It was found that 180 s was an optimal deposition time because longer deposition gave rise to fragile dendrites that were liable to be disconnected in the cell due to hydrogen evolution. The pores in dendritic morphology achieved on polycrystalline Ti substrate were consequence of the vigorous hydrogen gas evolution and the microstructure formed depended on diffusion-limited metal deposition. At the same time, for comparison electrodeposition was conducted at significantly lower current density (0.1 A cm^{-2}) to examine the microstructure, morphology and electrochemical characteristics of obtained deposits. The anomalous codeposition at a lower current densities (0.1 A cm^{-2}), results in a significant change of the morphology and composition i.e. the formation of a non-dendritic NiCoFe deposit with an overall composition of 20 at.% Ni, 45 at.% Co and 35 at.% Fe and a BCC structure. The crystallite size of the obtained deposits however, was not affected by the current density applied due to the similar overpotential during electrodeposition at different current densities.

SEM and TEM methods showed that the powder particles obtained at high current density of 1 A cm^{-2} have a highly branched dendritic structure. The powder particles were roughly $100 \text{ }\mu\text{m}$ in diameter but contained dendrites down to 50 nm width, comprising nanodendritic branches with grains of about 7.9 nm . The particle size of the NiCoFe alloy powder increased

both with increasing current density and increasing time of powder production. TEM dark field images showed that the mean area weighted grain size of the nanodendritic branches is 7.9 nm, which is in good agreement with the mean crystallite size derived from X-ray studies (7.4 nm). This suggests that the dendrites consist of very small nanograins that do not contain many defects or subgrain boundaries. The hierarchical nature of the NiCoFe dendrites is reflected in the high Hausdorff fractal dimensions of 1.77, which is close to that of natural ferns. Self-assembly of metallic nanoparticles led to a dendritic structure suitable for practical applications. Layer deposits additionally possessed circular depressions of ca. 20 μm diameter due to the intensive gas evolution that accompanied the alloy deposition. The alloy was also demonstrated to be an effective catalyst for nitrate reduction.

Therefore, it was possible to deposit nanodendritic NiCoFe powders and deposits with a high surface area that are of interest for catalytic applications. The electroreduction of NO_3^- on both, the nanodendritic and non-dendritic deposits were compared showing that the nanodendritic NiCoFe deposits are suitable to be used as catalysts due to their extremely developed surface area. Nanoarchitecture of dendritic NiCoFe alloy structure resembling natural fern leaves can play an important role as advanced material for practical application.

Bibliography

- [1] H. Gleiter. Nanocrystalline materials. *Advanced Structural and Functional Materials*, pages 1–37, 1991.
- [2] M.A. Meyers, A. Mishra, and D.J. Benson. Mechanical properties of nanocrystalline materials. *Progress in Materials Science*, 51(4):427–556, 2006.
- [3] L.P. Bicelli, B. Bozzini, C. Mele, and L. D’Urzo. A review of nanostructural aspects of metal electrodeposition. *Int. J. Electrochem. Sci*, 3:356–408, 2008.
- [4] K.I. Popov and M.G. Pavlovic. Metal powder production by electrolysis. *Electrochemistry Encyclopedia*.
- [5] U. Erb. Electrodeposited nanocrystals: synthesis, properties and industrial applications. *Nanostructured Materials*, 6(5-8):533–538, 1995.
- [6] U. Erb, A.M. El-Sherik, G. Palumbo, and K.T. Aust. Synthesis, structure and properties of electroplated nanocrystalline materials. *Nanostructured materials*, 2(4):383–390, 1993.
- [7] I. Bakonyi, E. Toth-Kadar, T. Tarnoczi, LK Varga, A. Cziraki, I. Geröcs, and B. Fogarassy. Structure and properties of fine-grained electrodeposited nickel. *Nanostructured Materials*, 3(1-6):155–161, 1993.
- [8] R. Würschum, S. Gruss, B. Gissibl, and H. Natter. Free volumes and thermal stability of electro-deposited nanocrystalline Pd. *Nanostructured*, 9(1-8):615–618, 1997.

- [9] O. Karaagac, H. Kockar, and M. Alper. Composition Dependence of Structural and Magnetic Properties of Electrodeposited Co-Cu Films. *IEEE Transactions on Magnetics*, 46(12):3973–3977, 2010.
- [10] T. Morikawa, T. Nakade, M. Yokoi, Y. Fukumoto, and C. Iwakura. Electrodeposition of Ni-P alloys from Ni-citrate bath. *Electrochimica acta*, 42(1):115–118, 1997.
- [11] R. Rofagha, U. Erb, D. Ostrander, G. Palumbo, and K.T. Aust. The effects of grain size and phosphorus on the corrosion of nanocrystalline Ni-P alloys. *Nanostructured materials*, 2(1):1–10, 1993.
- [12] C. Cheung, F. Djuanda, U. Erb, and G. Palumbo. Electrodeposition of nanocrystalline Ni-Fe alloys. *Nanostructured materials*, 5(5):513–523, 1995.
- [13] D.L. Grimmett, M. Schwartz, and K. Nobe. Pulsed Electrodeposition of Iron-Nickel Alloys. *Journal of the Electrochemical Society*, 137:3414, 1990.
- [14] C. Karwas and T. Hepel. Influence of Boric Acid on Electrodeposition and Stripping of Ni-Zn Alloys. *Journal of the Electrochemical Society*, 135(4):839–844, 1988.
- [15] C. Karwas and T. Hepel. Morphology and Composition of Electrodeposited Cobalt-Zinc Alloys and the Influence of Boric Acid. *Journal of The Electrochemical Society*, 136(6):1672–1678, 1989.
- [16] K.J. Bryden and J.Y. Ying. Electrodeposition synthesis and hydrogen absorption properties of nanostructured palladium-iron alloys. *Nanos-structured Materials*, 9(1-8):485–488, 1997.
- [17] N.V. Myung, D.Y. Park, M. Schwartz, K. Nobe, H. Yang, C.K. Yang, and J.W. Judy. Electrodeposited hard magnetic thin films for MEMS applications. In *Sixth International Symposium on Magnetic Materials, Processes and Devices, Proc. Electrochem. Soc*, 2000.
- [18] T. Osaka, M. Takai, K. Hayashi, K. Ohashi, M. Saito, and K. Yamada. A soft magnetic CoNiFe film with high saturation magnetic flux density and low coercivity. *Nature*, 392(6678):796–798, 1998.

- [19] A.R. Despić and V.D. Jović. Electrochemical Formation of Laminar Deposits of Controlled Structure and Composition. *Journal of the Electrochemical Society*, 134(12):3004–3011, 1987.
- [20] D.S. Lashmore and M.P. Dariel. Electrodeposited Cu-Ni Textured Superlattices. *Journal of the Electrochemical Society*, 135(5):1218–1221, 1988.
- [21] U. Cohen, F.B. Koch, and R. Sard. Electroplating of cyclic multilayered alloy (CMA) coatings. *Journal of the Electrochemical Society*, 130(10):1987–1995, 1983.
- [22] J. Crousier, Z. Hanane, and J.P. Crousier. Electrodeposition of NiP amorphous alloys. A multilayer structure. *Thin solid films*, 248(1):51–56, 1994.
- [23] M. Shirkhanzadeh. Electrochemical fabrication of alkoxy-derived nanocrystalline zirconia coatings at room temperature. *Materials Letters*, 16(4):189–193, 1993.
- [24] J. Switzer. Electrochemical architecture of ceramic nanocomposites. *Nanostruct. Mater.*, 1(1):43–46, 1992.
- [25] D. Pletcher. *First course in electrode processes*. Springer Verlag, 2009.
- [26] J.O.M. Bockris and G.A. Razumney. *Fundamental aspects of electrocrystallization*. Plenum press New York, 1967.
- [27] J.W. Diggle, A.R. Despic, and J.O.M. Bockris. The mechanism of the dendritic electrocrystallization of zinc. *Journal of The Electrochemical Society*, 116(11):1503–1514, 1969.
- [28] W. Plieth. *Electrochemistry for material science*. Elsevier, 2008.
- [29] D.R. Gabe. The role of hydrogen in metal electrodeposition processes. *Journal of applied Electrochemistry*, 27(8):908–915, 1997.
- [30] R.T.C. Choo, J.M. Toguri, A.M. El-Sherik, and U. Erb. Mass transfer and electrocrystallization analyses of nanocrystalline nickel production by pulse plating. *Journal of applied electrochemistry*, 25(4):384–403, 1995.

- [31] E. Budevski, G. Staikov, W.J. Lorenz, and K.E. Keusler. Electrochemical phase formation and growth. *Angewandte Chemie-German Edition*, 109(12), 1997.
- [32] A. Milchev. Electrochemical alloy formation - theory of progressive and instantaneous nucleation without overlap. *Electrochimica acta*, 42(10):1533–1536, 1997.
- [33] V.M. Weber. Keimbildung in übersättigten Gebilden. *Z. physik. Chem*, 119:277–301, 1926.
- [34] S.A. Chambers. Epitaxial growth and properties of thin film oxides. *Surface science reports*, 39(5-6):105–180, 2000.
- [35] N. Eliaz and M. Eliyahu. Electrochemical processes of nucleation and growth of hydroxyapatite on titanium supported by real-time electrochemical atomic force microscopy. *Journal of Biomedical Materials Research Part A*, 80(3):621–634, 2007.
- [36] L.G. Benning, G.A. Waychunas, SL Brantley, and JD Kubicki. Nucleation, growth, and aggregation of mineral phases: Mechanisms and kinetic controls. *Kinetics of Water-Rock Interaction*, pages 259–333, 2008.
- [37] J.W. Dini. *Electrodeposition: the materials science of coatings and substrates*. William Andrew Publishing, 1993.
- [38] K.I. Popov, S.S. Djokić, and B.N. Grgur. *Fundamental aspects of electrometallurgy*. Plenum Pub Corp, 2002.
- [39] A. Damjanovic. On the mechanism of metal electrocrystallization. *Plating*, 52:1017–1026, 1966.
- [40] K.I. Popov, M.J. Pavlovic, M.I. Cekerevac, and G.Z. Removic. Electrode surface coarsening in pulsating overpotential copper electrodeposition. *Surface and Coatings Technology*, 34(3):355–363, 1988.
- [41] C.L. Rinne, J.J. Hren, and P.S. Fedkiw. Electrodeposition of tin needle-like structures. *Journal of the Electrochemical Society*, 149:C150, 2002.

- [42] K.I. Popov and N.V. Krstajić. The mechanism of spongy electrodeposits formation on inert substrate at low over potentials. *Journal of applied electrochemistry*, 13(6):775–782, 1983.
- [43] J. Karczmarczuk. Dendrites in nature and in computers. 2006.
- [44] C.P. Chen and J. Jorné. Fractal analysis of zinc electrodeposition. *Journal of the Electrochemical Society*, 137(7):2047–2051, 1990.
- [45] D.L. Feldheim and C.A. Foss. *Metal nanoparticles: synthesis, characterization, and applications*. CRC, 2002.
- [46] G.K. Boschloo, A. Goossens, and J. Schoonman. Investigation of the potential distribution in porous nanocrystalline TiO₂ electrodes by electrolyte electroreflection. *Journal of electroanalytical chemistry*, 428(1-2):25–32, 1997.
- [47] K. Lin, R. Weil, and K. Desai. Effects of current density, pulse plating, and additives on the initial stage of gold deposition. *Journal of The Electrochemical Society*, 133:690, 1986.
- [48] A.M. El-Sherik, J. Shirokoff, and U. Erb. Stress measurements in nanocrystalline Ni electrodeposits. *Journal of Alloys and Compounds*, 389(1-2):140–143, 2005.
- [49] J.J. Vlassak. Thin Film Mechanics. *Harvard University, Boston, MA*, 2004.
- [50] K. Cholevas, N. Liosatos, A.E. Romanov, M. Zaiser, and E.C. Aifantis. Misfit dislocation patterning in thin films. *Physica status solidi (b)*, 209(2):295–304, 1998.
- [51] B.W. Sheldon, A. Rajamani, A. Bhandari, E. Chason, SK Hong, and R. Beresford. Competition between tensile and compressive stress mechanisms during Volmer-Weber growth of aluminum nitride films. *Journal of applied physics*, 98:043509, 2005.
- [52] R.V. Kukta and L.B. Freund. Minimum energy configuration of epitaxial material clusters on a lattice-mismatched substrate. *Journal of the Mechanics and Physics of Solids*, 45(11-12):1835–1860, 1997.

- [53] R. Hoffman. Stresses in thin films: The relevance of grain boundaries and impurities. *Thin Solid Films*, 34:185–190, 1976.
- [54] E. Chason, B.W. Sheldon, L.B. Freund, J.A. Floro, and S.J. Hearne. Origin of compressive residual stress in polycrystalline thin films. *Physical review letters*, 88(15):156103, 2002.
- [55] S.J. Hearne and J.A. Floro. Mechanisms inducing compressive stress during electrodeposition of Ni. *Journal of Applied Physics*, 97:14901, 2005.
- [56] E.G. Shafrin. Constitutive relations in the wetting of low energy surfaces and the theory of the retraction method of preparing. *The Journal of Physical Chemistry*, 64(5):519–524, 1960.
- [57] W. Barthlott and C. Neinhuis. Purity of the sacred lotus, or escape from contamination in biological surfaces. *Planta*, 202(1):1–8, 1997.
- [58] M.F. Doerner and W.D. Nix. Stresses and deformation processes in thin films on substrates. *Critical Reviews in Solid State and Materials Sciences*, 14(3):225–268, 1988.
- [59] A.S. Arico, P. Bruce, B. Scrosati, J.M. Tarascon, and W. Van Schalkwijk. Nanostructured materials for advanced energy conversion and storage devices. *Nature materials*, 4(5):366–377, 2005.
- [60] I. Gurrappa and L. Binder. Electrodeposition of nanostructured coatings and their characterization - a review. *Science and Technology of Advanced Materials*, 9:043001, 2008.
- [61] S. Gorer and R.M. Penner. Multipulse Electrochemical/Chemical Synthesis of CdS/S Core/Shell Nanocrystals Exhibiting Ultranarrow Photoluminescence Emission Lines. *The Journal of Physical Chemistry B*, 103(28):5750–5753, 1999.
- [62] H. Liu and R.M. Penner. Size-selective electrodeposition of mesoscale metal particles in the uncoupled limit. *The Journal of Physical Chemistry B*, 104(39):9131–9139, 2000.
- [63] M.P. Zach and R.M. Penner. Nanocrystalline nickel nanoparticles. *Advanced Materials*, 12(12):878–883, 2000.

- [64] R.E. Dinnebier and K. Friese. *Modern XRD Methods in Mineralogy*, chapter 3. Eolss Publishers, 2003.
- [65] D. Landolt. Electrodeposition science and technology in the last quarter of the twentieth century. *Journal of the Electrochemical Society*, 149(3):S9–S20, 2002.
- [66] R. Orinakova, A. Turonova, D. Kladekova, M. Galova, and R.M. Smith. Recent developments in the electrodeposition of nickel and some nickel-based alloys. *Journal of Applied Electrochemistry*, 36(9):957–972, 2006.
- [67] H. Li and F. Ebrahimi. Synthesis and characterization of electrodeposited nanocrystalline. *Materials Science and Engineering A*, 347(1-2):93–101, 2003.
- [68] N.V. Myung and K. Nobe. Electrodeposited iron group thin-film alloys structure-property relationships. *Journal of the Electrochemical Society*, 148(3):C136–C144, 2001.
- [69] D.Y. Park, K.S. Park, J.M. Ko, D.-H. Cho, S.H. Lim, W.Y. Kim, B.Y. Yoo, and N.V. Myung. Electrodeposited Ni_{1-x}Co_x nanocrystalline thin films. *Journal of the Electrochemical Society*, 153(12):C814–C821, 2006.
- [70] N.V. Myung, D.Y. Park, B.Y. Yoo, and P.T.A. Sumodjo. Development of electroplated magnetic materials for MEMS. *Journal of Magnetism and Magnetic Materials*, 265(2):189–198, 2003.
- [71] K.I. Popov and M.G. Pavlovic. Electrodeposition of metal powders with controlled particle grain size and morphology. *Modern Aspects of Electrochemistry*, 24:299–391, 1993.
- [72] K.I. Popov, N.V. Krstajic, and M.I. Cekerevac. The mechanism of formation of coarse and disperse electrodeposits. *Modern Aspects of Electrochemistry*, 30:261–311, 1996.
- [73] A. Calusaru. Electrodeposition of Powders from Solutions. *Electrodeposition of Powders from Solutions*, 1979.
- [74] A. Maricic, M. Spasojevic, L. Rafailovic, V. Milovanovic, and L. Ribic-Zelenovic. Hydrogen absorption and desorption kinetics in nickel and cobalt alloy powder. *Materials Science Forum*, 453-454:411–416, 2004.

- [75] L. Ribic-Zelenovic, L. Rafailovic, M. Spasojevic, and A. Maricic. The influence of structural changes on electrical and magnetic characteristics of amorphous powder of the Ni_xMo_y alloy. *Science of Sintering*, 38(2):145–153, 2006.
- [76] L. Ribic-Zelenovic, L. Rafailovic, M. Spasojevic, and A. Maricic. Correlation between electron state density change and the electrical resistivity and magnetic permeability changes in the nanostructured powder of the NiMo alloy. *Physica B: Condensed Matter*, 403(12):2148–2154, 2008.
- [77] E. Gomez, S. Pane, X. Alcobe, and E. Valles. Influence of a cationic surfactant in the properties of cobalt-nickel electrodeposits. *Electrochimica Acta*, 51(26):5703–5709, 2006.
- [78] S. Hassani, K. Raeissi, and M.A. Golozar. Effects of saccharin on the electrodeposition of Ni-Co nanocrystalline coatings. *Journal of Applied Electrochemistry*, 38(5):689–694, 2008.
- [79] A. Bai and C.-C. Hu. Effects of electroplating variables on the composition and morphology of nickel-cobalt deposits plated through means of cyclic voltammetry. *Electrochimica Acta*, 47(21):3447–3456, 2002.
- [80] C. Lupi and D. Pilone. Electrodeposition of nickel-cobalt alloys: The effect of process parameters on energy consumption. *Minerals Engineering*, 14(11):1403–1410, 2001.
- [81] A. Bianco, G. Gusmano, R. Montanari, G. Montesperelli, and E. Traversa. Microstructural characterisation of Ni, Co and NiCo fine powders for physical sensors. *Thermochimica Acta*, 269-270(C):117–132, 1995.
- [82] V.D. Jovic, B.M. Jovic, and M.G. Pavlovic. Electrodeposition of Ni, Co and Ni-Co alloy powders. *Electrochimica Acta*, 51(25):5468–5477, 2006.
- [83] V.D. Jovic, B.M. Jovic, V. Maksimovic, and M.G. Pavlovic. Electrodeposition and morphology of Ni, Co and Ni-Co alloy powders. Part II. Ammonium chloride supporting electrolyte. *Electrochimica Acta*, 52(12):4254–4263, 2007.

- [84] H.C. Shin and J. Dong. Nanoporous structures prepared by an electrochemical deposition process. *Advanced Materials*, 15(19):1610–1614, 2003.
- [85] N.D. Nikolic, L.J. Pavlovic, M.G. Pavlovic, and K.I. Popov. Formation of dish-like holes and a channel structure in electrodeposition of copper under hydrogen co-deposition. *Electrochimica Acta*, 52(28):8096–8104, 2007.
- [86] J. Ebothe and S. Vilain. Surface roughness and morphology of Co-(Fe and Ni) binary alloy electrodeposits studied by atomic force microscopy. *Journal of Physics D: Applied Physics*, 32(18):2342–2353, 1999.
- [87] A. Brenner. Electrodeposition of Alloys. *Electrodeposition of Alloys*, 1-2, 1963.
- [88] H.M. Rietveld. A profile refinement method for nuclear and magnetic structures. *Journal of Applied Crystallography*, 2:65–71, 1969.
- [89] A X S Bruker. TOPAS V2.1: General Profile and Structure Analysis Software for Powder Diffraction Data. *TOPAS V2.1: General Profile and Structure Analysis Software for Powder Diffraction Data*, 2005.
- [90] T.B. Massalski. Binary Alloy Phase Diagrams. *Binary Alloy Phase Diagrams*, 1990.
- [91] L. Wang, Y. Gao, Q. Xue, and H. Liu. Microstructure and tribological properties of electrodeposited Ni-Co alloy deposits. *Applied Surface Science*, 242(3-4):326–332, 2005.
- [92] S. Tao and D.Y. Li. Tribological, mechanical and electrochemical properties of nanocrystalline copper deposits produced by pulse electrodeposition. *Nanotechnology*, 17(1):65–78, 2006.
- [93] M.K. Roy, V.S. Subrahmanyam, and H.C. Verma. Defect studies in Fe-Cu alloys prepared by electrodeposition. *Physics Letters, Section A: General, Atomic and Solid State Physics*, 328(4-5):375–379, 2004.
- [94] Daheum Kim, D.Y. Park, B.Y. Yoo, P.T.A. Sumodjo, and N.V. Myung. Magnetic properties of nanocrystalline iron group thin film

- alloys electrodeposited from sulfate and chloride baths. *Electrochimica acta*, 48(7):819–830, 2003.
- [95] V. Radmilovic, K.I. Popov, M.G. Pavlovic, A. Dimitrov, and S. Hadzi Jordanov. The mechanism of silver granular electrodeposits formation. *Journal of Solid State Electrochemistry*, 2(3):162–169, 1998.
- [96] H. Vogt. Improved current efficiency equation for the electrodeposition of copper. *Journal of Applied Electrochemistry*, 25(8):764–769, 1995.
- [97] H. Vogt and R.J. Balzer. The bubble coverage of gas-evolving electrodes in stagnant electrolytes. *Electrochimica Acta*, 50(10):2073–2079, 2005.
- [98] M.P. Marceta Kaninski, V.M. Nikolic, G.S. Tasic, and Z.Lj. Rakocevic. Electrocatalytic activation of Ni electrode for hydrogen production by electrodeposition of Co and V species. *International Journal of Hydrogen Energy*, 34(2):703–709, 2009.
- [99] L.D. Rafailović, D.M. Minić, H.P. Karnthaler, J. Wosik, T. Trišović, and G.E. Nauer. Study of the Dendritic Growth of Ni-Co Alloys Electrodeposited on Cu Substrates. *Journal of the Electrochemical Society*, 157:D295–D301, 2010.
- [100] H.C. Shin, J. Dong, and M. Liu. Nanoporous Structures Prepared by an Electrochemical Deposition Process. *Chem. Phys*, 203:1556, 2002.
- [101] Y. Song, Y. Yang, C.J. Medforth, E. Pereira, A.K. Singh, H. Xu, Y. Jiang, C.J. Brinker, F. van Swol, and J.A. Shelnutt. Controlled synthesis of 2-D and 3-D dendritic platinum nanostructures. *J. Am. Chem. Soc*, 126(2):635–645, 2004.
- [102] J. Huang, S. Vongehr, S. Tang, H. Lu, J. Shen, and X. Meng. Ag Dendrite-Based Au/Ag Bimetallic Nanostructures with Strongly Enhanced Catalytic Activity. *Langmuir*, 25(19):11890–11896, 2009.
- [103] R. Qiu, X.L. Zhang, R. Qiao, Y. Li, Y.I. Kim, and Y.S. Kang. CuNi Dendritic Material: Synthesis, Mechanism Discussion, and Application as Glucose Sensor. *Chem. Mater*, 19(17):4174–4180, 2007.

- [104] F. Jia, C. Yu, K. Deng, and L. Zhang. Nanoporous metal (Cu, Ag, Au) films with high surface area: General fabrication and preliminary electrochemical performance. *J. Phys. Chem. C*, 111(24):8424–8431, 2007.
- [105] M. Liu and L. Jiang. Switchable adhesion on liquid/solid interfaces. *Advanced Functional Materials*, 20:3753–3764, 2010.
- [106] Y. Lai, Z. Lin, Z. Chen, J. Huang, and C. Lin. Fabrication of patterned CdS/TiO₂ heterojunction by wettability template-assisted electrodeposition. *Materials Letters*, 64(11):1309–1312, 2010.
- [107] X.Z. Fu, Q.C. Xu, R.Z. Hu, B.X. Pan, J.D. Lin, and D.W. Liao. [beta]-CoOOH coated spherical [beta]-NiOOH as the positive electrode material for alkaline Zn-NiOOH battery. *Journal of power sources*, 164(2):916–920, 2007.
- [108] T.M. Benedetti, V.R. Gonçalves, D.F.S. Petri, S.I. Torresi, and R.M. Torresi. Macroporous MnO₂ electrodes obtained by template assisted electrodeposition for electrochemical capacitors. *Journal of the Brazilian Chemical Society*, 21(9):1704–1709.
- [109] H.P. Karnthaler, F. Prinz, and G. Haslinger. Electron Microscopy of the Dislocation Structure in Plastically deformed Cu-5at.%Al Single Crystals. *Acta Metall*, 23(2):155–163, 1975.
- [110] A.D. Krawitz. *Introduction to diffraction in materials science and engineering*. Wiley, 2001.
- [111] P. Angerer, W. Artner, E. Neubauer, L.G. Yu, and K.A. Khor. Residual stress in spark-plasma-sintered and hot-pressed tantalum samples determined by X-ray diffraction methods. *International Journal of Refractory Metals and Hard Materials*, 26(4):312–317, 2008.
- [112] I.C. Noyan. *Residual Stress—Measurement by Diffraction and Interpretation*. Springer-Verlag, 1987.
- [113] U. Welzel, J. Ligot, P. Lamparter, A.C. Vermeulen, and E.J. Mittemeijer. Stress analysis of polycrystalline thin films and surface regions by X-ray diffraction. *Journal of Applied Crystallography*, 38(1):1–29, 2005.

- [114] D. Quéré. Wetting and roughness. *Annu. Rev. Mater. Res.*, 38:71–99, 2008.
- [115] A.T. Hasouna, K. Nogi, and K. Ogino. Effects of Surface Finish, Heat Treatment and Cold Working on the Wettability of Solid Copper by Liquid Tin. *Transactions of the Japan Institute of Metals*, 29(10):812–819, 1988.
- [116] L.D. Rafailović, H.P. Karnthaler, T. Trisović, and D.M. Minić. Microstructure and mechanical properties of disperse Ni-Co alloys electrodeposited on Cu substrates. *Materials Chemistry and Physics*, 120(2-3):409–416, 2010.
- [117] N. Zech, E.J. Podlaha, and D. Landolt. Anomalous Codeposition of Iron Group Metals: I. Experimental Results. *Journal of the Electrochemical Society*, 146(8):2886–2891, 1999.
- [118] J.P. McHale and S.V. Garimella. Bubble nucleation characteristics in pool boiling of a wetting liquid on smooth and rough surfaces. *International Journal of Multiphase Flow*, 36(4):249–260, 2010.
- [119] A. Reuss. Berechnung der Fließgrenze von Mischkristallen auf Grund der Plastizitätsbedingung für Einkristalle. *ZAMM-Journal of Applied Mathematics and Mechanics*, 9(1):49–58, 1929.
- [120] W. Voigt. *Lehrbuch der kristallphysik*. BG Teubner, 1910.
- [121] W. Martienssen and H. Warlimont. *Springer handbook of condensed matter and materials data*. Springer Verlag, 2005.
- [122] K.S. Kumar, S. Suresh, M.F. Chisholm, J. Horton, and P. Wang. Deformation of electrodeposited nanocrystalline nickel. *Acta Materialia*, 51(2):387–405, 2003.
- [123] D.Y. Park, R.Y. Song, J.M. Ko, B.Y. Yoo, and N.V. Myung. Stress changes of nanocrystalline CoNi thin films electrodeposited from chloride baths. *Electrochemical and Solid-State Letters*, 8:C23, 2005.
- [124] F. Czerwinski. Grain Size-Internal Stress Relationship in Iron-Nickel Alloy Electrodeposits. *Journal of the Electrochemical Society*, 143:3327, 1996.

- [125] H.V. Venkatesetty. Electrodeposition of thin magnetic permalloy films. *Journal of the Electrochemical Society*, 117:403–407, 1970.
- [126] T. Osaka. Electrodeposition of highly functional thin films for magnetic recording devices of the next century. *Electrochimica Acta*, 45(20):3311–3321, 2000.
- [127] N.H. Phan, M. Schwartz, and K. Nobe. Electrodeposition of Fe- Ni-Co alloys part I: Direct current deposition. *Journal of Applied Electrochemistry*, 21(8):672–677, 1991.
- [128] M.P. Zach and R.M. Penner. Nanocrystalline nickel nanoparticles. *Advanced Materials*, 12(12):878–883, 2000.
- [129] C. Suryanarayana and C.C. Koch. Nanocrystalline materials - Current research and future directions. *Hyperfine Interactions*, 130(1):5–44, 2000.
- [130] R. Qiu, H.G. Cha, H.B. Noh, Y.B. Shim, X.L. Zhang, R. Qiao, D. Zhang, Y.I. Kim, U. Pal, and Y.S. Kang. Preparation of Dendritic Copper Nanostructures and Their Characterization for Electroreduction. *The Journal of Physical Chemistry C*, 113(36):15891–15896, 2009.
- [131] Y. Sverdlov, Y. Rosenberg, Y.I. Rozenberg, R. Zmood, R. Erlich, S. Natan, and Y. Shacham-Diamand. The electrodeposition of cobalt-nickel-iron high aspect ratio thick film structures for magnetic MEMS applications. *Microelectronic engineering*, 76(1-4):258–265, 2004.
- [132] M.G. Pavlovic, L.J. Pavlovic, I.D. Doroslovaki, and N.D. Nikolic. The effect of benzoic acid on the corrosion and stabilisation of electrodeposited copper powder. *Hydrometallurgy*, 73(1-2):155–162, 2004.
- [133] Y.K. Yoo, Q. Xue, Y.S. Chu, S. Xu, U. Hangen, H.C. Lee, W. Stein, and X.D. Xiang. Identification of amorphous phases in the Fe-Ni-Co ternary alloy system using continuous phase diagram material chips. *Intermetallics*, 14(3):241–247, 2006.
- [134] M. Li, C. Feng, Z. Zhang, and N. Sugiura. Efficient electrochemical reduction of nitrate to nitrogen using Ti/IrO₂-Pt anode and different cathodes. *Electrochimica Acta*, 54(20):4600–4606, 2009.

- [135] T. Cosgrove. *Colloid science: principles, methods and applications*. Wiley-Blackwell, 2010.
- [136] C. Gammer, C. Mangler, C. Rentenberger, and H.P. Karnthaler. Quantitative local profile analysis of nanomaterials by electron diffraction. *Scripta Materialia*, 63(3):312–315, 2010.
- [137] Z. Ji, H. Li, Y. Liu, and W. Hu. The replacement reaction controlling the fractal assembly of copper nanoparticles. *Nanotechnology*, 19:135602, 2008.
- [138] R.M. Brady and R.C. Ball. Fractal growth of copper electrodeposits. *Nature*, 309:225–229, 1984.
- [139] M. Shishikura. The Hausdorff dimension of the boundary of the Mandelbrot set and Julia sets. *The Annals of Mathematics*, 147(2):225–267, 1998.
- [140] Fractalyse Software: <http://www.fractalyse.org/>.

Acknowledgements

I would like to express my sincere gratitude to Prof. Dr. Hans-Peter Karnthaler for giving me the opportunity to discover the nano-world with deeper insight and for very helpful discussions.

I am very grateful to Prof. Dr. Christian Rentenberger for very valuable discussions and for his positive attitude. To Prof. Tomas Waitz I am grateful for support and for creating good working atmosphere together with other members at the Faculty of Nanostructured Materials.

I am grateful for support by the I.K. “Experimental Materials Science - Nanostructured Materials”, a college for PhD students at the University of Vienna, Austrian Science Fund (FWF): [S10403, P22440] and COMET program by the Austrian Research Promotion Agency (Österreichische Forschungsförderungsgesellschaft, FFG) and the government of Lower Austria.

I am thankful to all members of the TEM group, to Dr. Clemens Mangler, Dr. David Geist and especially to Mag. Christoph Gammer for constant interest and discussions throughout this work.

To Prof. Dr. Tomislav Trišović I am very thankful for support in all respects, at the beginning in Serbia, but also for consultancy during the work on this thesis together with Prof. Dragica Minić.

I am very grateful for all kind of support from Center of Electrochemical Surface Technology in Wr. Neustadt to Prof. Dr. Christoph Kleber and to Dr. Adam Whitehead for bringing this text into the final form and for very helpful suggestions.

For all administrative support in Vienna I am thankful to Regina Pinter and in Wr. Neustadt to Anita Heiner and Brigitte Polly.

For all their time, love and support during my stay in Vienna I am very grateful to family Vukajlović.

CURRICULUM VITAE

Lidija Rafailović

Center of Electrochemical Surface Technology,

CEST, Wr. Neustadt

Viktor- Kaplan Strasse 2

A-2700 Wr. Neustadt

Phone: +43-(0)2622-222 66-26

E-mail: lidija.rafailovic@cest.at

Fax: +43-(0)2622-222 66-50

Website: www.cest.at

Personal information

Date and place of birth 24. May 1971, Ehingen, Germany

Citizenship Serbian

Education

2007-present PhD studies
Faculty of Physics, University of Vienna
supervisor: Prof. Dr. Hans- Peter Karnthaler

October 2006 Mag. in Chemistry
Faculty of Natural Sciences and Mathematics, University of Kragujevac. thesis: *Influence of electrolysis parameters on properties of obtained nickel and cobalt powders*
supervisors: Prof. Dr. Miloš Djuran and Prof. Dr. Miroslav Spasojević

March 1998 B.Sc. in Physical Chemistry
Faculty of Physical Chemistry, University of Belgrade
thesis: *Physical Chemistry of Induction Processes of Delayed Fluorescence in Chlorophyll*
supervisors: Prof. Dr. Čedomir Radenović and Prof. Dr. Mihailo Jeremić

Work experience

2010-present	Researcher Center of Electrochemical Surface Technology, CEST, Wr. Neustadt, Austria www.cest.at
2007-2010	Research Assistant Physics of Nanostructured Materials, Faculty of Physics, University of Vienna http://physnano.univie.ac.at/
2005-2007	Researcher on project in collaboration with the Joint Laboratory for Advanced Materials of Serbian Academy of Science and Arts, Belgrade, Section for Amorphous Systems, at the Technical Faculty in Čačak, University of Kragujevac www.tfc.kg.ac.rs
2000-2007	Teaching Assistant Physical Chemistry and Analytical Chemistry, Food Technology Department, Čačak, University of Kragujevac www.afc.kg.ac.rs
1998-2000	Research Assistant Food Technology Department, Čačak, University of Kragujevac www.afc.kg.ac.rs

Awards

- | | |
|------|--|
| 2007 | Diploma of the Russian Ministry of Education and Science at the International Exhibition of inventors GENIUS, for Advanced multipurpose electrochemical cell |
| 2006 | Award from foundation "Mladen Selak" for young inventors organized by Serbian Chamber of commerce and Association of inventors. |
| 2005 | Award from town of Čačak |
| 2001 | Scholarship from the Ministry of Science Republic of Serbia |

Publications

Articles in refereed journals:

A.Gavrilovic, L.D.Rafailovic, W.Artner, J.Wosik, A.H. Whitehead, *The corrosion behavior of amorphous and nanocrystalline Fe_{73.5}Cu₁Nb₃Si_{15.5}B₇ alloy*, Corrosion Science, 53 (2011) 2400-2405.

A.Gavrilovic, D.Minic, L.D.Rafailovic, J.Wosik, P.Angerer, D.M.Minic, *Influence of thermal treatment on structure development and mechanical properties of amorphous Fe_{73.5}Cu₁Nb₃Si_{15.5}B₇ ribbon*, J. Alloy. Compd., accepted (2010).

L.D.Rafailovic, D.M.Minic, H.P.Karnthaler, T.Trisovic, J.Wosik, G.E.Nauer, *Study of the dendritic growth of Ni-Co alloys electrodeposited on Cu substrates*, J. Electrochem. Soc., 157 (2010) 295-301.

L.D.Rafailovic, H.P.Karnthaler, T.Trisovic, D.M.Minic, *Microstructure and mechanical properties of disperse Ni-Co alloys electrodeposited on Cu substrates*, Mater. Chem. Phys, 120 (2010) 409-416.

L.D.Rafailovic, W.Artner, G.E.Nauer, D.M.Minic, *Structure, morphology and thermal stability of electrochemically obtained Ni-Co deposits*, Thermochem. Acta, 496 (1-2) (2009) 110-116.

L.Ribic-Zelenovic, L.Rafailovic, M.Spasojevic, A.Maricic, *Correlation between electron state density change and the electrical resistivity and magnetic permeability change in the nanostructured powder of the NiMo alloy*, Physica B, 403 (2008) 2148-2154.

A.Maricic, M.Spasojevic, L.Rafailovic, V.Milovanovic, L.Ribic-Zelenovic, *Hydrogen absorption and desorption kinetics in nickel and cobalt alloy powder*, Material Science Forum, 453-454 (2004) 411-416.

Posters&Talks:

L.Rafailovic, *Electrochemical synthesis of nanopowders and metal disperse deposits of iron group metals with a highly developed surface area*, Kolloquium über aktuelle Fragen der Materialphysik WS 2010/2011, October 2010, Westfälische Wilhelms Universität, Münster, Germany.

L.D.Rafailovic, C.Gammer, D.Minic, A.Gavrilovic, P.Angerer, E.Schäfer, H.P.Karntaler, N.Krendelsberger, G.E.Nauer, *Characterization of electrochemically deposited ternary NiCoFe alloy powders*, 61st International Meeting of the Electrochemical Society, ISE, September 2010, Nice, France.

L.Rafailovic, C.Gammer, P.Angerer, A.Gavrilovic, G.Nauer, H.P.Karntaler, *Thermal treatment of the CoNi electrodeposits*, 17th International Symposium on Metastable, Amorphous and nanostructured materials, ISMANAM 2010, July 2010, Zurich, Switzerland.

L.Rafailovic, T.Trisovic, B.Grgur, G.Nauer, *The new multipurpose electrochemical cell*, 217th Electrochemical Society Meeting, ECS May 2010, Vancouver, Canada.

L.Rafailovic, D.Minic, H.P.Karnthaler, J.Wosik, G.Nauer, *Study of the Dendritic Growth of NiCo Alloy Powders Electrodeposited on Cu Substrates*, 216th Electrochemical Society Meeting, ECS October 2009, Vienna, Austria.

L.Rafailovic, P.F.Rogl, D.M.Minic, H.P.Karnthaler, *Quantitative SEM study of NiCo alloy powders electrodeposited on Cu substrates*, MC 2009, Microscopy Conference, September 2009, Graz, Austria.

L.D.Rafailovic, H.P.Karnthaler, *Phase transformation in nanograined Co₉₅Ni₀₅ obtained by electrodeposition*, International Conference from Nanoparticles and Nanomaterials to Nanodevices and Nanosystems (IC4N), July 2009, Rhodes, Greece.

L.Rafailovic, H.P.Karnthaler, T.Trisovic, P.F.Rogl, *Iron group nanopowders electrodeposition*, 10th Materials Research Society Conference "YUCOMAT 2008", September 2008, Herceg Novi, Montenegro.

L.Rafailovic, H.P.Karnthaler, P.F.Rogl, T.Trisovic, *Electrodeposition of nanostructured ferromagnetic powders*, 1st Regional Symposium on Electrochemistry of South-East Europe, May 2008, Rovinj, Croatia.

A.M.Maricic, A.Kalezic-Glisovic, N.S.Mitrovic, L.Rafailovic, M.M.Ristic, *The effect of structural changes on functional properties of the Fe_{73.5}Cu₁Nb₃Si_{15.5}B₇ metastable alloy*, 7th Scientific Meeting, Physics and Technology of Materials, FITEM, Annual Meeting, July 2007, Čačak, Serbia.